Design and Development of a Novel DC/DC Bidirectional Converter with Dual Solar/PV-Based Snow Removal and EV Charging Functionality

by

Sandra M. Aragon Aviles

A thesis submitted to the

School of Graduate and Postdoctoral Studies in partial

fulfillment of the requirements for the degree of

Master of Applied Science in Electrical and Computer Engineering

Department of Electrical, Computer, and Software Engineering

Faculty of Engineering and Applied Sciences

University of Ontario Institute of Technology (Ontario Tech University)

Oshawa, Ontario, Canada

February 2022

THESIS EXAMINATION INFORMATION

Submitted by: **Sandra Aragon Aviles**

Master of Applied Science in **Electrical and Computer Engineering**

Thesis title: Design and Development of a Novel DC/DC Bidirectional Converter with Dual Solar/PV-Based Snow Removal and EV Charging Functionality

An oral defence of this thesis took place on February 14, 2022 in front of the following examining committee:

Examining Committee:

Chair of Examining Committee	Dr. Khalid Elgazzar
Research Supervisor	Dr. Sheldon S. Williamson
Research Co-supervisor	Dr. Tarlochan Sidhu
Examining Committee Member	Dr. Vijay Sood
Thesis Examiner	Dr. Martin Agelin-Chaab, UOIT

The above committee determined that the thesis is acceptable in form and content and that a satisfactory knowledge of the field covered by the thesis was demonstrated by the candidate during an oral examination. A signed copy of the Certificate of Approval is available from the School of Graduate and Postdoctoral Studies.

ABSTRACT

Different factors affect solar photovoltaic (PV) systems by decreasing input energy and reducing the conversion efficiency of the system. One of these factors is the effect of snow cover on PV panels, a subject lacking sufficient academic research. This thesis reviews current research for snow removal in solar PV modules and power electronic circuit topologies used. Additionally, it presents the design, analysis and modelling of a smart heating system for solar PV electric vehicle (EV) charging applications. The system is based on a bidirectional buck-boost DC/DC converter that redirects the grid/battery power into heating of the PV modules thus removing snow cover, as well as providing the function of MPPT when required to charge the EV battery. A performance evaluation by simulating and testing the system under various climatic conditions is presented validating the usefulness of the proposed converter to be used in solar PV systems under extreme winter conditions.

Keywords: solar PV systems; bidirectional DC-DC converter; bidirectional synchronous buck converter; snow removal; EV charging.

AUTHOR'S DECLARATION

I hereby declare that this thesis consists of original work of which I have authored. This is a true copy of the thesis, including any required final revisions, as accepted by my examiners.

I authorize the University of Ontario Institute of Technology (Ontario Tech University) to lend this thesis to other institutions or individuals for the purpose of scholarly research. I further authorize University of Ontario Institute of Technology (Ontario Tech University) to reproduce this thesis by photocopying or by other means, in total or in part, at the request of other institutions or individuals for the purpose of scholarly research. I understand that my thesis will be made electronically available to the public.

<div style="text-align: right">

_____   SANDRA ARAGON AVILES

</div>

STATEMENT OF CONTRIBUTIONS

Part of the work described in Chapter 1 and Chapter 2 has been published as:

Part of the work described in Chapter 1 and Chapter 3 has been submitted for publication as:

The work described in Chapter 4 was performed at one of the climatic chambers at the ACE facility in Ontario Tech University, operated by Luke Durst, Kyle Cannon and other ACE staff members. The inverter control was put into operation by Mr. Sherif Abdelsamad, member of the "Upstartz Energy Ltd." company, who participated as a sponsor of this study. I was responsible for installing and testing the solar PV panels under extreme winter conditions, and taking the respective measurements.

I acknowledge the support provided by my co-authors on all papers. However, all the work contained within these publications is my own, and my co-authors provided advisory and direction in the development of the final product. Any published (or unpublished) ideas and/or techniques from the work of others are fully acknowledged in accordance with the standard referencing practices.

I performed the majority of the analysis, designing and modelling of the proposed converter, testing of the solar PV panels under extreme winter conditions, and writing of the manuscript.

ACKNOWLEDGEMENTS

I would like to thank my friends in Colombia and elsewhere for their moral support to keep me on the right track.

Last but not least, I would like to thank my family for always being there, even when you are so far away from me. Thank you for always believing in me and bringing me all your support and love in good times and in bad. This is for you.

Los amo pa, ma, pala y paydi.

TABLE OF CONTENTS

LIST OF TABLES

LIST OF FIGURES

LIST OF ABBREVIATIONS

In order of appearance:

PV   Photovoltaic

EV   Electric vehicles

MPPT   Maximum power point tracking

CWT   Climatic Wind Tunnel

DC/DC   Direct current/direct current

GHG   Greenhouse gas emissions

IEA   International Energy Agency

CO2   Carbon dioxide

Gt   Gigatonnes

PHEV   Plug-in hybrid electric vehicles

IRENA   International Renewable Energy Agency

GW   Gigawatts

HEV   Hybrid electric vehicles

BEV   Battery electric vehicles

EREV   Extended range-electric vehicles

ICE   Internal combustion engine

SAE   Society of Automotive Engineers

IEC   International Electrotechnical Commission

SAC   Standardization Administration of China

AC	Alternating current
VAC	Alternating current voltage
VDC	Direct current voltage
V	Voltage
A	Amperes
kW	Kilowatts
V2G	Vehicle-to-grid
BMS	Battery management system
kWh	Kilowatt hour
Li-ion	Lithium-ion
Li-Po	Lithium-ion polymer
CCS	Combined charging system
CV	Constant voltage
CC	Constant current
CC-CV	Constant current – constant voltage
MPP	Maximum power point
IGBT	Insulated-gate bipolar transistor
P&O	Perturb and observe
INC	Incremental conductance
FOCV	Fractional open circuit voltage
FSCC	Fractional short circuit current
SCM	Slide control mode
SEPIC	Single-ended primary inductor converter

ZVS	Zero-voltage-switching
HB	Half-bridge
ZVT	Zero-voltage-transition
ZCS	Zero-current-switching
CCM	Continuous conduction mode
ESR	Equivalent series resistance
ELS	Effective series inductance
THD	Total harmonic distortion
DAB	Dual active bridge
FB	Full-bridge
PWM	Pulse-width modulation
MOSFET	Metal-oxide semiconductor field-effect transistor
QR	Quasi-resonance
LVS	Low-voltage switching
SiC	Silicon carbide
ZSI	Z-source inverter
W/m^2	Watts per square meter
°C	Celsius degree
m^2	Square meters
Wp	Watt-peak
m	Meter
W	Watts
kW/m^2	Kilowatt per square meter

Ω	Ohm
BHBC	Bidirectional half-bridge converter
SBC	Synchronous buck converter
EMF	Electromotive force
kHz	Kilohertz
µH	Microhenry
µF	Microfarads
ms	Millisecond
PCS	Power conversion system
HORIZ	Horizontal
VERT	Vertical
ORIEN	Orientation
Hrs	Hours

LIST OF SYMBOLS

Chapter 2

I	Current
V	Voltage
P	Power
I_{SC}	Short-circuit current
V_{OC}	Open-circuit voltage
I_{MPP}	Current at MPP
V_{MPP}	Voltage at MPP
I_{ph}	Photo-current
R_s	Series resistance
R_{sh}	Shunt resistance
I_{pv}	Output current of the PV panel or PV array
I_d	Diode current
V_d	Diode voltage
I_0	PV cell saturation current
k	Boltzmann constant $(1.38 \cdot 10^{-23} \, J/°K)$
T	Temperature of PV cell in $°K$ units
q	Electron charge $(1.6 \cdot 10^{-19} \, C)$
A	P-N junction ideality factor of the diode
K_1	PV cell temperature coefficient of short-circuit current
T_{cell}	PV cell operating temperature

T_{ref}	PV cell reference temperature
λ	Solar irradiance in W/m^2

Chapter 3

A	Reverse saturation current of the PV panel
B	Inverse of the thermal voltage of the PV panel
V_{pv}	Output voltage of the PV panel or PV array
R_{pv}	Resistance of the Norton model
D	Diode
L	Inductance
C	Capacitor
P_{MAX}	Peak power
η_m	Module efficiency
P_{PV}	Solar PV array power
S_1, S_2	Controllable MOSFET switch 1 and 2
D_{S1}, D_{S2}	Internal diode of MOSFET's S1 and S2
C_1	Input capacitor
C_2	Output capacitor
t	Time
T	Period
D	Duty cycle
T_{dead}	Dead time
T_{on}	ON time

T_{off}	OFF time
V_{GS1}, V_{GS2}	Gate control signal of MOSFET's S1 and S2
i_L	Current of the inductor
v_L	Voltage of the inductor
i_{S1}, i_{S2}	Current of switches S1 and S2
V_{DS1}, V_{DS2}	Voltage of the internal diodes of the switches S1 and S2
i_C	Current of the capacitor
v_1	Input voltage or voltage at PV side
v_2	Output voltage or voltage at the load
ΔV_1	Input ripple voltage
ΔV_2	Output ripple voltage
Δi_L	Estimated inductor ripple current
$V_{1(min)}$	Minimum input voltage
η	Estimated efficiency of the converter
V_2	Desired output voltage
$I_{1(Max)}$	Maximum input current necessary in the application
$I_{2(Max)}$	Maximum output current necessary in the application
V_1	Typical input voltage
f_s	Minimum switching frequency of the converter
V_{bus}	Bus voltage or output voltage of the converter
v_{C1}	Input capacitor voltage
R_{C1}	Internal resistance of input capacitor C1

R_L	Internal resistance of inductor L
α, β, γ	Variables
$G_{id}(s)$	Transfer function of the inductor current in relation to the duty cycle
$G_{vd}(s)$	Transfer function of the input capacitor voltage in relation to the duty cycle
I_{LRef}	Inductor reference current
C_{iL}	Inductor current controller
X	State vector
U	Input or control vector
A_m, B_m, C_m, D_m	State-space representation matrices
V_{pvRef}	Solar PV array reference voltage
C_{vpv}	Solar PV array voltage controller
K_p	Coefficient of proportional term
T_i	Integration time

Chapter 4

S	Solar irradiance

Note: When modelling the proposed converter, the capital letters indicates the DC values (steady-state), and the superscript symbol ($\sim$) denotes the small AC perturbations of the variables.

Chapter 1. Introduction

In this chapter, the background to the problem is described, the motivation for the work is presented, and the objectives and contributions of the thesis are outlined.

1.1 Background

There is a growing concern in the world about climate change and global warming. Since one of the main causes of global warming is greenhouse gas (GHG) emissions, its reduction is an indisputable and urgent need. According to a report presented by the International Energy Agency (IEA), transportation and electricity/heat generation sectors represent more than 60% of the CO_2 emissions as shown in Figure 1.1 [1], [2]. Although the total energy spent in the transportation sector is used primarily by road, railway, ship and aviation transport, road transport represents three quarters of the total [3]. The report also shows that during 2017 in the world, CO_2 emissions from fossil fuel combustion, such as coal and oil approached to 14.5 gigatonnes (Gt) and 11.37 Gt, respectively [2]. In more recent studies, it has been analyzed that even global consumption fossil fuel will be lower with high penetration of EV in transportation but the efficacy in long term GHG reduction will be only when EV policy incorporates maximum uses of renewable energy with carbon pricing [4].
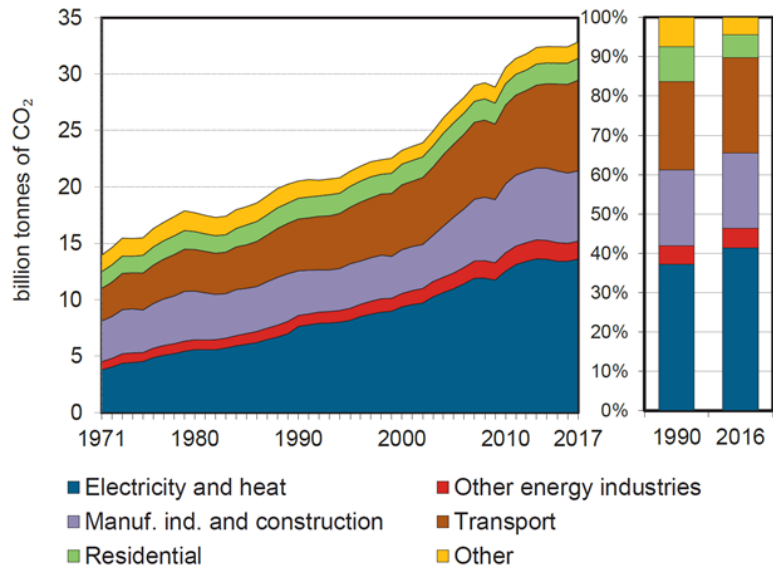
Figure 1.1. Global CO2 emissions by sector from 1971 to 2017 according to the IEA [2]. Source: IEA (2019) CO2 Emissions from Fuel Combustion - Highlights. All rights reserved.

1

Both conventional electric power and conventional vehicles rely on the combustion of fossil fuels, which contributes to the emission of CO_2 [5], [6]. Therefore, the use of standalone and grid-connected renewable energy sources, and the use of electric vehicles (EVs) and plug-in hybrid electric vehicles (PHEVs) are a realistic solution that will reduce CO_2 emissions and dependence on fossil-based sources, promising to be the future of energy and mobility [5], [7]. This is where the smart grid plays an important role in the game, making processes more efficient, ensuring optimal system energy management, reducing costs, increasing reliability, and facilitating the integration of renewable energy sources such as photovoltaic solar energy, and electric transport [8]–[10]. Over the last 5-10 years, there has been lots of advancement in technology in various fields, especially the ones that contribute to a smart grid infrastructure and real-time communication/pricing: smart meters, advanced information/communication technology [11].

The current trend of renewable energy sources dominating an ever-increasing share of the world's power grid mix has been increasing steadily over the past year. According to a report presented by International Renewable Energy Agency (IRENA) [12], by the end of 2019, renewable capacity had increased by 176 gigawatts (GW), compared to the previous year, to a capacity of 2537 GW. In the same report, it was also stated that in the last 10 years, the global solar photovoltaic capacity has increased from 40.2 GW to 580.1 GW. There are several influences that have resulted in the continuous integration of solar PV into EV charging system: rapid growth in global demand for EVs, concerns over the effects of GHG and a decrease in the price of solar PV modules [13].

Despite the increase in capacity in recent years, there are some challenges in developing solar systems that have made their implementation slow since their inception. Some of the limitations of solar PV systems include price (the relation between lifetime generation cost versus electricity prices), energy storage, efficiency, among others.

According to Ueda et al. [14] the efficiency of solar PV systems can be affected by meteorological parameters that decrease the input energy such as shading, soiling, snow covering, mismatch, etc.; or parameters that reduce the conversion efficiency such as module temperature, losses, equipment efficiency, among others [14].

Most of these factors have been researched in-depth, such as the effects of shading and mismatch or the efficiency of the converters used, resulting in an improvement in system efficiency [15]–[21]. The current converters developed has an efficiency of around 90 % or higher; however, more research is still required to improve the input energy efficiency of solar PV cells [22]–[25].

Various authors in the literature [26], [27] specifically described the factors that influence snowfall losses in solar PV systems. These factors are classified in two categories, environmental factors and system design factors. The environmental factors include snow characteristics, snowfall recurrence patterns, ambient and solar module temperature patterns, irradiation, wind speed and direction, and humidity. On the other hand, the factors related to the system design include tilt angle of the modules, orientation (fixed or tracking), tracker rotation parameters, installation type (open rack or building integrated), and distance of the modules to the ground.

A positive aspect in areas with a high tendency to snowfall is that soiling losses are reduced in the summer season due to regular precipitations throughout the year [26]. However, the most important negative aspect is that even a partial snow cover on the PV module can significantly reduce the energy produced by the entire panel; this problem is critical as one of the main purposes of the electricity used in these areas is to heat buildings [28], [29].

Many studies have been developed on the effects of snowfall on solar PV systems since this is one of the main factors affecting the performance of PV systems in cold areas [21], [26]–[28], [30]–[44].

DNV GL (formerly BEW Engineering) developed an analytical model to estimate snow loss in PV systems [26], [45]. This model estimated an annual yield loss ranging between 2% to 5%. On the other hand, Andrews et al. [30] proposed a different approach to the model by analyzing the snow shedding patterns. This research concluded that the annual energy losses ranged from 1 to 3.5%. Many more studies have been proposed in the literature to estimate energy losses in PV systems due to snowfall [26], [27], [29], [31], [33], [35], [37]–[39], [46] , each using different prediction models, including stochastic

3

and curve fitting models, as well as different input parameters, such as the PV system parameters, weather factors and the snow properties. However, all studies have shown different monthly energy loss results ranging from 1 to 90%, largely due to the different conditions evaluated in each model.

Several active and passive heating systems for snow removal of PV modules have been proposed in the literature. In Canada, the company Soltek Solar Energy Ltd., developed flush mount panels to reduce the snow covering issue on solar modules, however, there are still problems of icing on the modules [47]. Also, the use of different self-cleaning surfaces for the solar modules has been commercially developed, such as hydrophilic and superhydrophobic surfaces, which are made to repel water, forming beads of water that roll across the surface. There have also been attempts to create icephobic surface coatings, which repel ice or inhibit ice formation [32], [39], [42], [44], [47]. However, there are no conclusive and effective results related to these materials.

Ross and Usher [47], [48] proposed a heating system that melts snow using reflected radiation from the ground to heat the back surface of the PV module by using a black absorbent coating placed on the back of the module mounted alongside with a glass enclosure, although the results found were negligible. This model is shown in Figure 1.2.
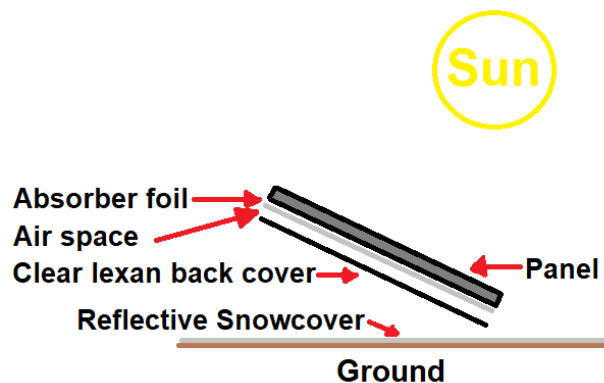
Figure 1.2. Ross and Usher's snow removal solution [47], [48].

Various patents were developed in Germany, Japan, Norway and Sweden [49]–[52] all of them using the same active method, but using different type of sensors for the control system. The proposed system consisted of applying a reverse current to the solar panel using an external power source in order to heat the solar cells, thus melting the snow. Other

4

methods included the use of resistive electrical cables to heat the frame of the photovoltaic modules that would produce an avalanche effect to remove snow. Several studies using these methods were found in the literature [51], [53]–[58]. However, although some of the proposed prototypes have had good results in reducing losses in the system caused by snow cover, most of these systems have used many sensors, such as photodetectors, temperature sensors and pyranometers, as well as they have used external voltage sources to produce the reverse current flow in the PV cells. Additionally, they lack relevant historical data to draw decisive conclusions.

1.2 Motivation

It is known that the main challenge of solar PV systems used in electric vehicle charging applications is to deliver efficient, reliable and fast power to the EV battery pack. As mentioned earlier in Section 1.1, one of the factors that affects solar PV systems is the snow cover; during winter, when the hours of solar radiation are reduced and snowfall is very abundant, solar panels can remain covered by snow or ice for weeks or even months, reducing its productivity to zero [55]. However, unlike other factors, there are not many effective solutions reported within the academic literature. In fact, only 5 articles were found in which active solutions were reported to counteract the effect of snow on solar panels [51], [54], [55], [57], [58].

In [55] Husu et al. proposed a method that involved heating the solar panel using a set of electrical resistors that are powered by an external voltage source. In addition, it used two irradiation sensors and a temperature sensor to control the heating of the electrical resistance. However, this method could be too expensive as it requires many sensors and an additional voltage source, which would not be cost effective in a system with multiple solar panels.

On the other hand, a different method was described in the other 4 manuscripts [51], [54], [57], [58]. In them the use of reverse electric current through the solar PV panel was used to heat the PV cells. The method used was based on the heating phenomenon of a forward biased diode that occurs when it begins to conduct current. In this case, when reverse current flow through the photodiodes of the PV panels, they generate dissipated

heat that was enough to start melting the snow/ice adhering to their surface, or allow the snow cover to slide off. However, although the reports showed good results in terms of effectiveness, important information was lacking in relation to design, control, among others.

For the reasons mentioned above, a power electronics circuit topology was proposed that would solve the aforementioned challenges. Therefore, this thesis will focus on the design, modeling, simulation and testing of an efficient bidirectional DC-DC power converter to be used in solar PV connected electric vehicle charging applications, including a snow removal function for solar systems located in places with winter climates.

1.3 Research Objectives

This thesis study mainly focuses on the integration of an EV battery charger system connected to solar PV with integrated snow removal functionality.

In this regard, the specific objectives of this thesis are the following:

- To develop an electrical model and design a bidirectional DC/DC conversion system for PV EV charging applications;

- To design the power management controller to achieve maximum power (including MPPT) of the PV system and at the same time manage the heat to melt snow/ice from the solar PV array using reverse current flow from the PV cell diode when needed;

- To verify the performance of a solar PV system with integrated snow removal functionality.

1.4 Contributions

The contributions of this work are:

- A comprehensive study of EV charger classification and standards, PV systems characteristics and modeling, and snow removal solutions for solar PV panels.

- Introduction of a solar PV system with integrated snow removal functionality that prevents the disruption or reduction of electricity production during the winter season in off-grid or on-grid EV charging systems.

- An overview of the available power electronics circuit topologies and the selection of a suitable topology for dual solar/PV-based snow removal and EV charging functionality based on the required criteria.

- Introduction of a permanent and simple solution that can be implemented even in previously installed systems, without requiring the installation of external components, only the proposed bidirectional dc-dc converter and its control system.

- Introduction of a system that offers total snow removal on the surface of solar panels at ambient temperatures above -15 °C, for solar PV panels placed in different orientations and tilt angles.

- Reduction of the number of stages used in a solar PV EV charging system, going from three stages to only two stages.

1.5 Outline of the thesis

This thesis presents in detail the design, modeling, simulation and testing of a bidirectional DC-DC buck-boost converter to interconnect a solar PV array and an EV charging system; The presented proposed system provides the maximum power to charge the EV battery pack and provides a reverse current flow to heat the PV cells to melt the snow on the surface of the solar panels when needed. The thesis is organized as follows. Section 2 presents a comprehensive overview regarding EV charging standards, PV system modelling and the several isolated and non-isolated topologies used to interface PV systems to the grid or to a storage system. Followed by Section 3, where a detailed design and modelling of the proposed bidirectional dc-dc converter is described, including the design of the controller and its simulation results. Additionally, in Section 4, the experimental results of the snow removal function applied to a commercially available inverter are described. Finally, Section 5 presents a summary of the main conclusions and possible

future work that can be developed to improve the efficiency of solar photovoltaic systems for electric vehicle charging applications in extreme snow conditions.

Chapter 2. Solar PV Systems for EV Charging Applications

PV-EV charging stations are widely implemented around the world since the boom of the EV is increasing year by year. More charging stations equals more electric range for the vehicle. However, in adverse winter climates the charging stations only rely on the grid or on the energy storage, since the solar panels are cover by snow and can't produce energy most of the time. This chapter presents a detailed review of EV charger classification and standards. It also describes different power architectures for integration of PV to the grid or to an energy storage. Additionally, this chapter dives into details about PV systems characteristics and modelling, and snow removal solutions for solar PV panels.

2.1 EV Charging Systems

2.1.1 *Electric Vehicles*

According to the definition of Bhatti et al. [13], a vehicle that is powered by electrical means whilst using one or more motors for motion is called an EV. The classification of EVs encompass: hybrid electric vehicles (HEV), battery electric vehicles (BEV), PHEV and extended range-electric vehicles (EREV) [5], [59], [60]. BEVs are equipped with a fully electric drivetrain which is powered by rechargeable batteries. On the other hand, PHEVs have a hybrid vehicle drivetrain, which uses a combination of an internal combustion engine (ICE) and electrical power, similar to a HEV, although its rechargeable battery can be charged by plugging it into an external power supply unlike HEVs [5], [61].

EV chargers can be classified as: on-board or off-board, and conductive or inductive. Based on the place where the battery charger is installed can be classified as on-board or off-board. In this way, an on-board battery charger is installed inside the EV, while off-board chargers are placed outside the EV [62], [63]. On the other hand, battery chargers can be classified as conductive or inductive, depending on the mode of power transfer from the power source to EV [62]. In this way, power flow between the PV/grid and the EV battery is delivered using plugs and sockets when utilizing conductive chargers [62], [63]. On the other hand, the transfer of power using resonance via a wireless medium is allowed

by the inductive chargers [63]. However, this thesis focuses mainly on the conductive off-board EV chargers.

2.1.2 *Standards for EV/PHEV Charging*

There are different standards available that regulate charging operations for EVs/PHEVs with many classifications and rules regarding infrastructure, communication, interface and safety [64], [65]. The standards issued by the Society of Automotive Engineers (SAE), the International Electrotechnical Commission (IEC), and the Standardization Administration of China (SAC) are the most used in US, Europe and China, respectively.

Table 2.1. Summary of EV charging standards [64]–[67]

Type	Standards	Description
Interface	SAE J1772 SAE J1773 GB/T 20234 Part 1 to 2 GB/T 33594 IEC 62196 Part 1 to 3 IEC 62893 Part 1 to 4 IEC 61851 Part 1 GB/T 18487 Part 1	They describe the requirements for plugs, sockets outlets, vehicle inlets and couplers as well as charging cables for conductive and inductive electric vehicle charging. Also, the different charging power levels for AC and DC charging are described here.
Communication	SAE J2293 Part 2 SAE J2836 Part 1 to 6 SAE J2847 Part 2 SAE J1850 SAE J2931 Part 1, 4 and 7 SAE J2953 Part 1 and 2 IEC 61850 Part 90-8 IEC 61980 Part 1 to 3 IEC 61851 Part 24 GB/T 27930 ISO 15118-8	These standards describe the requirements for the communication network interface, its protocols, network architecture, interoperability, and security, all between the charger and the EV. It is important to note that the communication protocol for the SAE standard is PLC (Power line carrier) and that used by GB/T and CHAdeMO is based on the CAN (Controller Area Network) protocol.
Infrastructure	SAE J2894 Part 1 and 2 SAE J2293 Part 1 IEC 61439 Part 5 and 7 IEC 61851 Part 1, 21, 23 and 25 GB/T 18487 Part 1 GB/T 29781 NFPA 70 Art. 625	These standards include the requirements for the system architectures and topologies, electromagnetic compatibility (EMC), power quality tests, system architecture of the energy transfer system (ETS), requirements for the DC EV supply equipment and the requirements for the assembly of power distribution in public networks
Safety	SAE J1766 SAE J2894-2 IEC 60364-7-722 IEC 62840 Part 2 GB/T 18384 Part 1 and 3 GB/T 37295 ISO 6469-3 ISO 17409	These standards describe test methods, safety and protection system requirements for electric vehicle chargers and battery swap systems. It also includes the necessary requirements for special installations. Additionally, SAE J1766 focuses on test methods for battery systems during crash tests.

Power levels.

The Society of Automotive Engineers' (SAE): SAE J1772 standard, is one of the most accepted standards for EV/PHEV charging power converters [62], [64]. As stated in the latest revised SAE J1772 standard, two AC charging power levels are designed for on-board chargers, whereas two DC charging power levels are dedicated for off-board chargers [66], as shown in Table 2.2.

The AC Level 1 charging is defined for slow charging operations and the AC charging level 2 refers to semi-fast charging. AC Level 1 is intended to be used for single-phase AC sources in common household circuits or charging stations with power levels that peak at 1.92 kW [61], [64]. However, this study is only focused on DC charging systems.

Table 2.2. SAE J1772 US Standard for EV/PHEV charging power levels [66].

Type	Level	Supplied Voltage Range (V)	Maximum Current (A)	Output Power Level (kW)
AC Charging (On-board chargers)	Level 1	120 VAC (1-phase)	up to 12 up to 16	up to 1.44 up to 1.92
	Level 2	208 – 240 VAC (1-phase or 3-phase)	up to 80	up to 19.2
DC Charging (Off-board chargers)	Level 1	50 - 600 VDC	up to 80	up to 48
	Level 2	50 - 1000 VDC	up to 400	up to 400

The DC charging systems are installed at fixed locations and are built with dedicated wiring [61]. In addition, this charging systems are known as fast charging systems since they can handle higher power levels, charging the electric vehicles in less time compared with the level 1 AC chargers. Although each EV battery pack require an specific power level supply, modern DC charging stations have implemented a system that identify the voltage level of the battery pack and adjust to that [61].

Depending on the flow of the power allowed by the charger, two types of charging systems can be found: unidirectional or bidirectional [68]. Then, when the power only flows in one direction from the grid/PV into the battery, is called unidirectional. On the other hand, when the power also flows from the battery to the grid, is it called bidirectional, under the concept of vehicle-to-grid (V2G) as mentioned in [68], [69].

11

2.1.3 *EV Battery Pack*

In terms of the EV battery, first, it is important to differentiate all the terms when talking about batteries, such as battery cell, module and a pack. In general, EV batteries are made up of each of these terms mentioned. Thus, a pack is made up of cluster of modules and all these modules have a group of hundreds of battery cells inside it connected in series and parallel to achieve the desired voltage and capacity [70]. Additionally, the final battery pack must include a battery management system (BMS) that will control/protect the battery from overheating, overcharging, or any other damage. It is good to mention that the EV battery pack is designed to meet the requirements of the motors and other equipment that the vehicle uses, however, all vehicles have different types of battery packs as they differ from their manufacturer, requirements of vehicle voltage and capacity, chemistry of the battery cells, among others [71].

Table 2.3 shows some of the characteristics for various EV models, however for the purpose of this thesis, we are going to focus on the nominal battery voltages. The values on the table below suggest that a range between 320V to 400V represents a reasonable assumption for the voltage of the battery to be used for the design of the proposed converter.

Table 2.3. EV Models battery and charger specifications [5], [72], [73].

EV 2021 Models	Battery capacity (kWh)	Battery Chemistry	Battery Supplier	Number of cells	Nominal Voltage (V)	DC Charging Interface
Audi e-tron	95	Lithium-ion (Li-ion)	LG Chem	432 cells in 36 modules	396	Type 2*
BMW i3	42.2	Lithium-ion (Li-ion)	Samsung SDI	-	353	Type 2*
Chevrolet Bolt	66	Lithium-ion (Li-ion)	LG Chem	288 cells of 3.75 volts	350	Type 1*
Chevrolet Spark EV (2016)	18.4	Lithium-ion (Li-ion)	LG Chem	192 cells	400	Type 1*
Fiat 500 electric	42	Lithium-ion (Li-ion)	Samsung/ Bosch	192 cells	364	Type 2*
Hyundai IONIQ EV	38.3	Lithium-ion polymer (Li-Po)	LG Chem	-	319.4	Type 2*
Hyundai KONA EV	39.2 and 64	Lithium-ion polymer (Li-Po)	LG Chem	294 cells in 5 modules	319 and 356	Type 2*

Jaguar I-Pace S	90	Lithium-ion (Li-ion)	LG Chem	432 cells in 36 modules	388	Type 1 and Type 2*
Kia Soul EV (2020)	39.2 and 64	Lithium-ion polymer (Li-Po)	SK Innovation	-	327 and 356	Type 1 and Type 2*
Mercedes-Benz EQC	80	Lithium-ion (Li-ion)	LG Chem and Deutsche ACCUMOTIVE	384 cells in 6 modules 230 Ah	405	Type 2*
Nissan Leaf SV	40	Lithium-ion (Li-ion)	AESC	192 cells in 24 modules	360	Type 4*
Tesla 3 Standard	54	Lithium-ion (Li-ion)	Panasonic / Tesla	2976 cells in 4 modules	360	Tesla charging inlet
Tesla S Long Range	100	Lithium-ion (Li-ion)	Panasonic / Tesla	7104 cells in 16 modules	350	Tesla charging inlet
Tesla X Long Range	100	Lithium-ion (Li-ion)	Panasonic / Tesla	8256 cells in 16 modules	350	Tesla charging inlet
Tesla Y	75	Lithium-ion (Li-ion)	LG Chem	4416 cells	350	Tesla charging inlet
Volkswagen e-Golf SE (2020)	35.8	Lithium-ion (Li-ion)	Samsung SDI	264 cells in 27 modules	323	Type 1 and Type 2*

* Type 1: IEC 62196-3 CC (CCS1); Type 2: IEC 62196-3 FF (CCS2); Type 4: IEC 62196-3 AA (CHAdeMO)

Additionally, another factor to consider when using batteries is their charging method. There are 3 different battery charging methods, including constant voltage CV, constant current CC and the combination of both CC-CV. In all cases, the BMS is in charge of this process, protecting the battery from overload or full discharge and maintaining its life cycle [65].

2.2 PV Systems

2.2.1 *Solar PV Panel*

When studying how to integrate PV systems into the grid or to a standalone system, first, it is very important to understand how a solar PV panel works. A solar PV panel is composed of an array of many photovoltaic (PV) cells connected in series and parallel. These photovoltaic cells are generally made up of layers of p and n silicon, however there are many other different materials that are being investigated in order to provide higher

efficiencies. The inner field between the positive and negative layers produces a potential difference when the sun rays ionize the atoms of the silicon. A stronger irradiance can produce a higher interaction between the atoms, producing a higher potential difference [74].

Figure 2.1 shows the current-voltage (I-V) and power-voltage (P-V) curve characteristics of a PV module. There are two important parameters of a PV module, named: short-circuit current (I_{SC}), which is the current that flows through the solar cells when its voltage is zero; and open-circuit voltage (V_{OC}), which is the maximum voltage a solar cell can provide when the current is zero. The power drawn from a solar module is a product of the PV module voltage and current setpoints. As can be seen in Figure 2.1, the power-voltage (P-V) characteristic curve of a PV module has a single point of maximum power (MPP) corresponding to a specific current (I_{MPP}) and voltage (V_{MPP}) under a level of constant irradiance [75]. Then, one of the main purposes of a DC-DC converter used on a PV system is to achieve the MPP of the PV array.
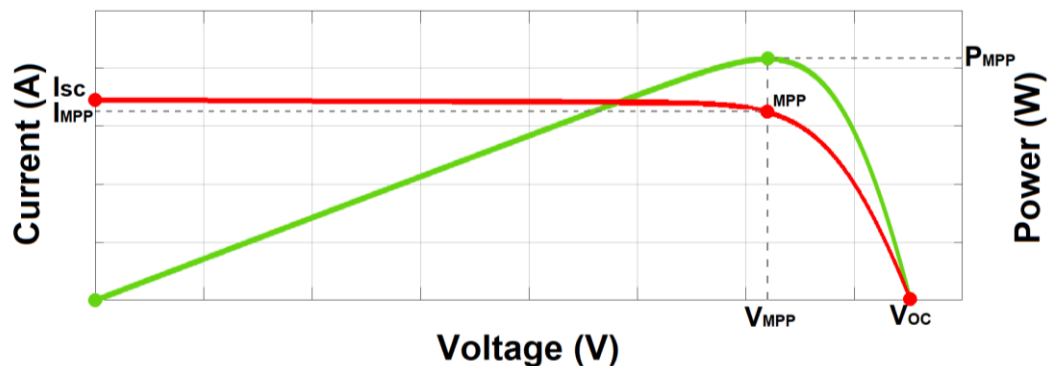
Figure 2.1. I–V and P–V curve characteristics of a PV module [22].

There are several models reported in the literature, which present the electrical characteristics of a solar PV panel [76], [77]. These models generally obtain the characteristic curves of the solar PV panel like the example shown above, through a modeling based on an equivalent electrical circuit or a set of mathematical equations.

The most common models of a solar PV module found in the literature are the single diode model and the two-diode model, however, the latter is more precise and presents an I-V characteristic curve that is closer to the real behavior of a PV panel [76]. The drawback

14

of this model is that it is much more complex and requires a greater computational effort than the single diode model. The single diode model is shown in Figure 2.2. The electrical energy produced by the PV panel is represented by a photo-current I_{ph}, which is proportional to the solar irradiance [76], [77]. The series resistance R_s included in the model represents the internal resistance of the PV panel, while the shunt resistance R_{sh} represents the leakage current.
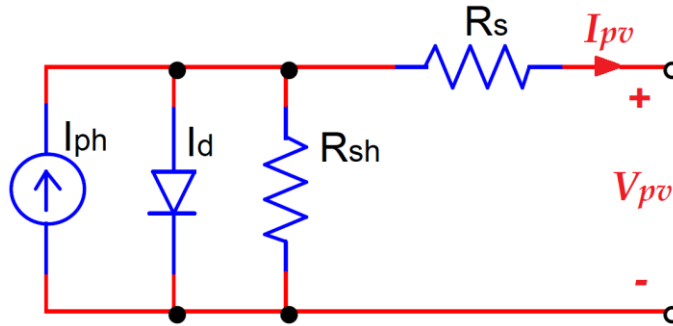
Figure 2.2. Single diode model of solar PV module [76], [77].

The output current of the PV module can be represented by the following equation:

$$I_{pv} = I_{ph} - I_d - \frac{V_d}{R_{sh}} \tag{2.1}$$

Where the diode current I_d is:

$$I_d = I_0\left(e^{\frac{V_d}{\frac{kT}{q}A}} - 1\right) \tag{2.2}$$

And photo-current I_{ph} is equal to:

$$I_{ph} = \left(I_{sc} + K_1(T_{cell} - T_{ref})\right)\lambda \tag{2.3}$$

The terms in the above equations are defined as follows:

V_d: diode voltage;

I_0: PV cell saturation current;

kT/q: thermal voltage of the PV cell; where k is the Boltzmann constant ($1.38 \cdot 10^{-23}\ J/°K$), T is the temperature of PV cell in $°K$ units, and q is the electron charge ($1.6 \cdot 10^{-19}\ C$);

A: p-n junction ideality factor of the diode;

I_{sc}: short-circuit current of the PV cell at standard test condition (STC) i.e. $1000\ W/m^2\ and\ 25\ °C$;

K_1: PV cell temperature coefficient of short-circuit current;

$T_{cell}\ and\ T_{ref}$: PV cell operating and reference temperature;

λ: solar irradiance in W/m^2.

According to [77], [78], the non-linear model shown in Figure 2.2 can be simplified by neglecting the effects of both resistances R_{sh} and R_s. Additionally, by neglecting the ground-leakage and small diode currents under zero-terminal voltage, and since $I_{ph} \gg I_0$, it is concluded that $I_{sc} \cong I_{ph}$. Hence, the equivalent circuit of a single diode model can be simplified as shown in Figure 2.3, where, the diode current I_d is represented by Ae^{B*Vpv}. In this expression, A is the reverse saturation current of the PV panel, B is the inverse of the thermal voltage of the PV panel, and V_{pv} is the output voltage of the PV panel.
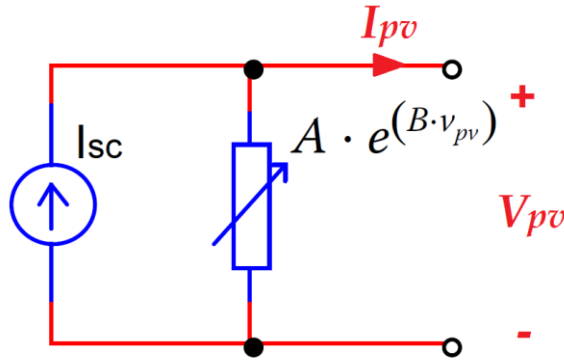
Figure 2.3. Simplified equivalent circuit of a single diode solar PV model [77], [78].

Then the equation of the simplified non-linear model can be expressed as:

$$I_{pv} = I_{sc} - Ae^{B*Vpv} \tag{2.4}$$

This model is very useful for electrical simulation purposes and can be applied for a solar PV array too; however, its complexity is high when it is used for control system analysis and design. For this reason, a linear modeling approach will be used for the analysis and design of control systems.

There are several linear models reported in the literature that represent the behaviour of the PV panel near to the MPP [74], [77], [79], [80]. One of these is the Norton equivalent model which has a response close to that of the non-linear model for voltages below V_{MPP}. Figure 2.4 depicts the Norton model.
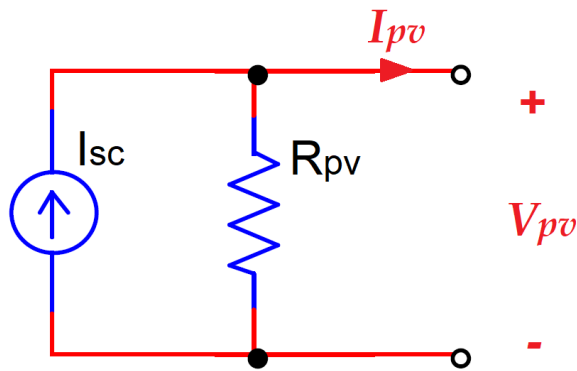
Figure 2.4. Norton equivalent model of PV panel [74].

As it can be seen from the above figure, this model includes the short-circuit current I_{sc}, which is proportional to the irradiance. This allows the PV system to be analyzed under different irradiance disturbances [74].

The equivalent resistance of the Norton model R_{pv} can be expressed as follows:

$$R_{pv} = \frac{V_{MPP}}{I_{sc} - I_{MPP}} \tag{2.5}$$

Figure 2.5 shows the PV panel model comparison of the I-V and P-V characteristic curves for the single diode simplified model and the Norton equivalent model.
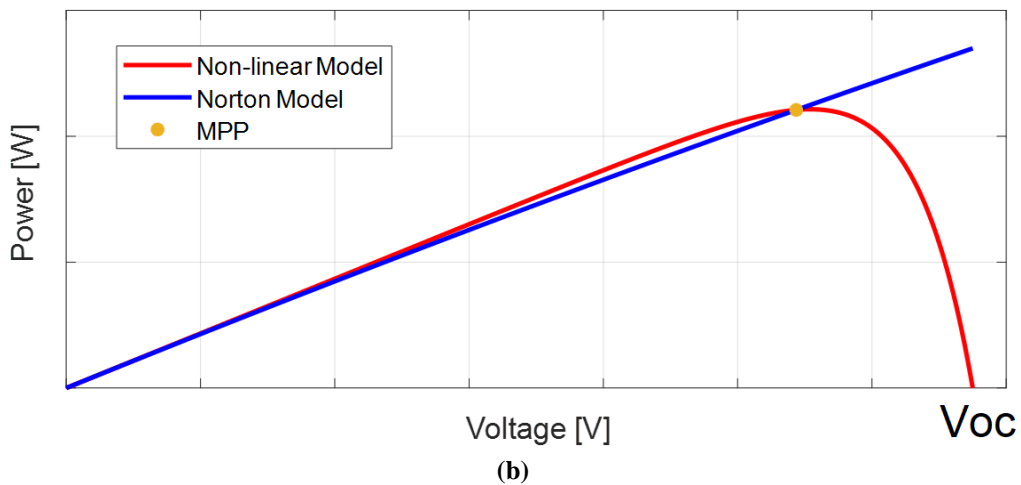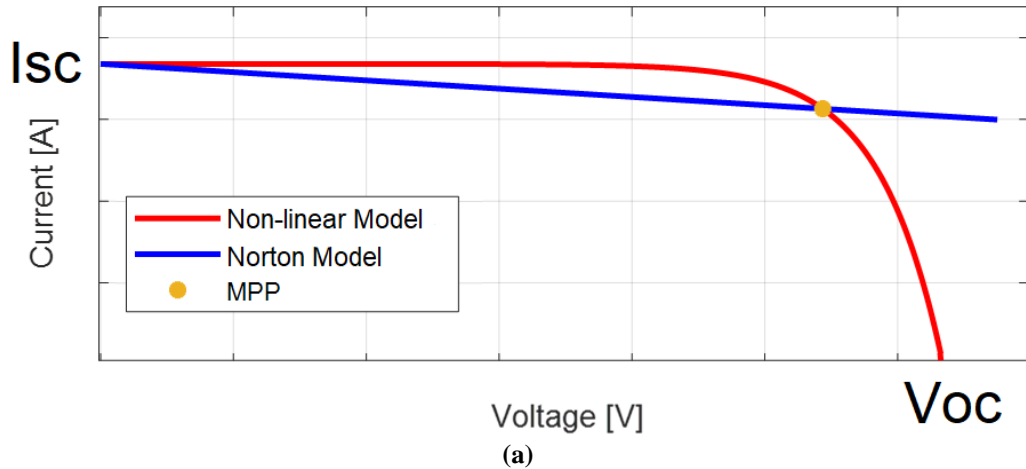
Figure 2.5. PV panel model comparison of the I-V and P-V characteristic curves. (a) I-V characteristic curve; (b) P-V characteristic curve [74].

2.2.2   *PV Systems Architectures*

It is also important to understand the different categories of structures generally used to connect the PV source to the load. These types of structures are known as centralized, string structure and module architectures.

The centralized structure aims at connecting all the PV modules of a PV array to a single converter, which depending on the system needs, can be a DC-DC converter or a DC-AC inverter, as shown in Figure 2.6(a). The main advantages of using this structure are the low-cost installations and the simplicity of control as discussed in the literature [81]. However, the main drawback of this structure is the high variation of the output power due to the mismatch conditions of the series-connected PV modules. Mismatch conditions are generally caused by partial shading or dust accumulation in the PV modules, or in other

18

cases due to silicon impurities or aging of the solar panels. Therefore, when these mismatch conditions arise, a decrease in system efficiency is expected since the system cannot extract the maximum power from the PV array [75]. Some of the most used inverter topologies when using this type of structure are low-frequency transformers and 3-phase full bridge using IGBTs [82].

On the other hand, string and module structures for PV systems were designed and developed to extract the maximum energy from the system [75], [83]. Figure 2.6(b) shows the string system architecture. As it can be seen from the figure, PV modules are series-connected and grouped in different strings. Unlike the centralized structure, each PV string has its own DC-DC converter or AC-DC inverter that uses a maximum power point tracking (MPPT) controller to extract the MPP of each string. This type of structure aims to increase the efficiency of the system when mismatch conditions appear compared to the centralized structure, although the power losses remain significant within the same strings [75]. To further improve the MPP tracking efficiency of the solar PV system under mismatched conditions, the use of integrated module inverter structures has been proposed in the literature. In this structure, each PV module has its own power converter with an MPPT controller, as shown in Figure 2.6(c). The main benefit of using this structure is the improvement on the MPP tracking efficiency for each PV module. Thus, decreasing the power losses produced by mismatch conditions. However, the use of this type of structure increases costs since a power converter is required for each photovoltaic module used [83], [84].
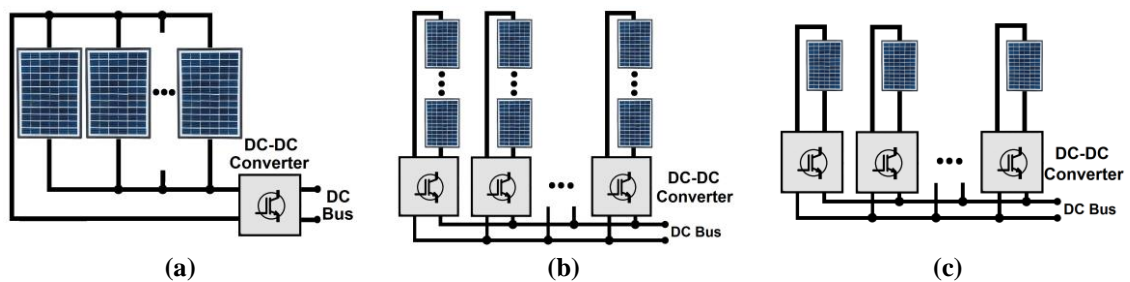
Figure 2.6. Conventional PV structures. (a) Centralized structure; (b) String structure; (c) Module structure [83].

As described in the literature, in order to achieve high DC bus voltages in PV-grid tied systems, a PV module series-connection is usually used, allowing to supply power to both;

the AC grid and battery storage devices at a high efficiency, in this case to the EV battery charger [75], [85]. However, as discussed above, one of the main challenges to solve on the PV stage is the mismatch conditions that affect the power provided by the PV array.

2.2.3 *MPPT Algorithms*

A very important consideration when designing solar energy systems is its efficiency. Since the power efficiency of solar energy systems depends on environmental factors such as irradiance, temperature or partial shading conditions, it is vital to implement a maximum power point tracker (MPPT) [86].

MPPT search algorithms are widely studied in the literature. Its main objective is to maximize the energy delivered by a solar PV panel or array. The search for maximum power point tracking (MPPT) is achieved by changing the duty cycle value of the power converter, which will depend on the disturbance in the input variables sensed such as PV voltage/current, PV panel temperature, and solar irradiance. As a result, there will be a change in the voltage or current of the solar PV panel/array, and as a consequence, a change in the power output [87]. The controller of the PV system is the one that most influences the overall performance of the system [88]. This controller not only makes the system work at the maximum power point (MPP) but also permanently tracks it when unpredictable changes appear in the environmental variables (irradiance and temperature), which are the main variables that produce some of the previously mentioned challenges. For this reason, the use of tracking algorithms or optimization methods to obtain the MPPT is very important in PV systems, and has been widely studied and compared in the literature [81], [86], [88]–[96].

The problem considered by MPPT techniques is to automatically find the voltage V_{MPP} or current I_{MPP} at which a PV array should operate to obtain the maximum output power P_{MPP} under a given temperature and irradiance. Most techniques respond to changes in both irradiance and temperature, but some are specifically more useful if temperature is approximately constant.

The numerous existing MPPT methods are classified as parametric-based or heuristic-based methods [88]. The parametric-based methods use a parametric model and measure

the parameters of the PV module directly or indirectly, while the heuristic-based methods measure the electric variables to determine whether the system is at the MPP [88]. A list of the major characteristics of the most known and used MPPT algorithms can be found in [86].

On the mentioned list can be found the conventional methods such as the Perturb and observe (P&O), incremental conductance (INC), fractional open circuit voltage (FOCV), fractional short circuit current (FSCC) and slide control mode (SCM). These methods are characterized by its simplicity and relatively easy implementation [86].

With so many MPPT techniques available for use in PV systems, it may not be obvious how to choose which one best suit your application needs. Based on the characteristics of the MPPT techniques, the main aspects to consider selecting the best control technique to use are the complexity of the implementation, the sensors that are required for the implementation, the multiple local maxima and the cost of the implementation of the controller. Based on those aspects, the MPPT technique selected for this study was the P&O technique, which according to [86], [92], it is a method that do not require very complexity on its implementation, only requires the voltage and the current measurements on the PV array as input parameters for the algorithm, and it can be implemented digitally.

Recently, many MPPT techniques have been developed and improved continuously, Perturb and Observe method is widely applied in the MPPT controllers due to its simplicity and easy implementation. The P&O MPPT algorithm is based on the disturbance of the output voltage V(k) of the PV panel and the corresponding output power P(k), which is compared with the previous perturbing cycle P(k-1). If the power increases, keep the next voltage change in the same direction as the previous change. Otherwise, change the voltage in the opposite direction as the previous one, when the stable condition is reached the algorithm oscillates around the peak power point. Figure 2.7 shows the flowchart of the P&O MPPT method.
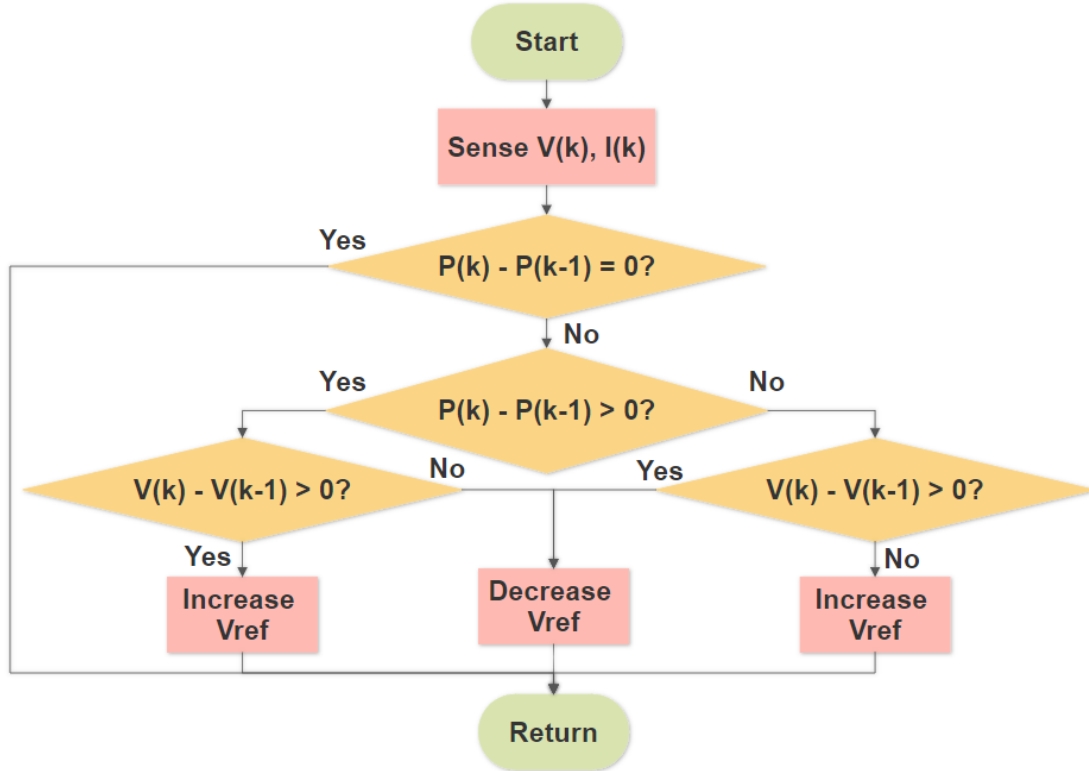
Figure 2.7. Flowchart of the P&O MPPT method [86], [92].

In the P&O method, the voltage is being increased or decreased with a fixed step size in the direction of reaching the MPP. The process is repeated periodically until the MPP is reached. At steady state, the operating point oscillates around the MPP. An optimized P&O algorithm was proposed by [87], by reducing the perturbation size of the duty cycle to reduce the oscillations of the array operating point around the MPP; additionally they proposed an optimized solution based on the tuning of the P&O algorithm according to the converter's dynamics.

2.3 Power Electronics Circuit Topologies

In this section are presented several topologies of isolated/non-isolated DC-DC converters and AC-DC inverters to interface the PV, the grid and the EVs/PHEVs, all of them classified depending on the stage where they can be used: PV stage, AC grid stage or charger stage for the EV. Several DC-DC and AC-DC converter topologies and their applications are discussed in [13], [22], [61], [64], [71], [85], [97]–[115].

2.3.1 *Solar PV-EV Charging System*

In this section it is presented the typical structure for a solar PV/grid-tied EV charging system, however this can also be applied for an off-grid system just by changing the type of converter used. The most important features and characteristics that the power electronic converters must provide are addressed. Additionally, the operation modes of the system are explained.

A typical block diagram for an off-board PV/grid-tied charging system for EV/PHEV is shown in Figure 2.8. The structure is interfaced through three power converters; in the PV stage, there is a DC-DC converter with MPPT, which is used to step up the voltage supplied by the PV array and at the same time provide the maximum power to the common DC bus; a bidirectional AC-DC inverter, which is part of the AC grid stage, aims to control the power factor and the current injected into the grid, and regulate the DC voltage to adapt to that required by the common DC bus [97]; and a bidirectional DC-DC converter, which belongs to the charger stage, serves as an interface for the EV/PHEV, controlling the DC charging current. All of these components are connected to the common DC bus, which has a voltage range from 200 to 600 VDC, according to the SAE J1772 standard reviewed on Section 2.1 [13]. There is also required in the system a central controller to establish the power flow and activation of the power converters based on different constraints e.g. minimum charging cost, maximum profit, among others [13], [116]–[118].
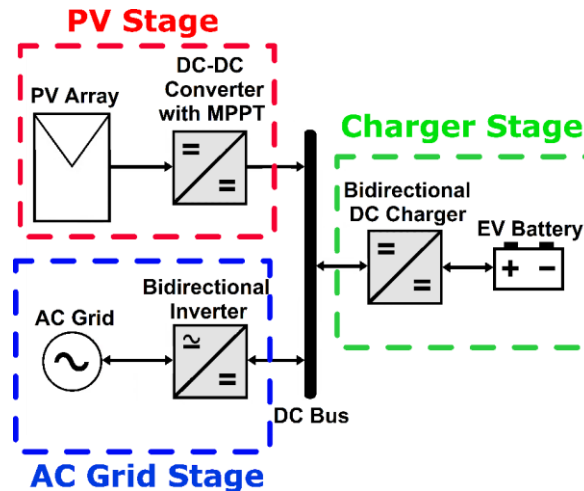
Figure 2.8. Overall PV/grid-tied off-board EV charging system structure [13], [83].

23

The use of a bidirectional inverter in the AC grid stage, as shown in Figure 2.8, will allow the transfer of excess power from the PV array to the AC grid throughout the sunny hours of the day. Additional, in the system showed, the flow of power from the EV battery to the grid (V2G) can be allowed. During low solar irradiation the battery can draw energy from the grid. In order to facilitate the inverter and rectification modes of operation in the PV/grid-tied charging system, a bidirectional inverter is used [98], [119]–[121].

To interconnect all the stages, the power converters must guarantee some characteristics to suit the system; For example, according to the grid needs, the power converters must provide a high power factor, with zero distortion and galvanic isolation to protect both, the grid and the EV [104]. As stated in the literature, this galvanic isolation can be implemented on the front-end of the AC-DC inverter through a low-frequency transformer. Another option to implement the isolation can be using an isolated DC-DC power converter at the charger stage by using a high frequency transformer [97], [104].

Furthermore, at the charging stage, a power converter is required to control the charging power of the EV battery, so that the battery life can be maximized. It is also worth noting that the converters selected for this application must have high efficiency since high power is transferred to and from the common DC bus. [104].

2.3.2 *Unidirectional DC-DC Converters*

On the PV stage, it is required a unidirectional DC-DC converter capable of extracting the maximum power from each solar module in a PV array and at the same time maintaining the voltage at the output of the converter, which is connected to the DC bus of the system. However, this thesis seeks to implement a system that extracts the maximum power from the solar panel and at the same time seeks to melt the snow on the solar panels in the winter season to increase the efficiency of the system; therefore, it is necessary to use a bidirectional DC-DC converter in this case.

During high temperatures and low levels of irradiation, the PV endures its main issues with performance, significantly reducing the power provided by the PV array [85]. When using non-isolated or transformerless converters, the use of series-connected PV modules is necessary to achieve the required voltage of the DC bus. However, as discussed in

24

Section 2.2.2, these mismatch conditions become more problematic when series-connected PV modules are used. Many solutions are reported in the literature with the aim of addressing this problem.

As reported by Esram and Chapman [81], several maximum power point tracking (MPPT) techniques have been developed and implemented. The methods most used are perturb and observe, incremental conductance, fuzzy logic control and hill climbing; however, this last-mentioned technique is the most preferred, since it reduces oscillation in steady state, providing better tracking efficiency. On the other hand, methods such as artificial neural network or fuzzy logic control are more flexible when handling module mismatch or partial shading conditions according to [13], [89].

The most used power converters for the PV stage are the standard non-isolated, boost and buck–boost topologies. Although, there is also reported the use of Cuk and Single-Ended Primary Inductor Converter (SEPIC) in the literature [13], [22], [99].

To acquire a higher output voltage, the input voltage magnitude must be stepped up accordingly as shown in Figure 2.9(a) by the DC-DC boost converter [22]. On the other hand, the magnitude of the input voltage can either be lower or higher than the output voltage magnitude when speak of the buck-boost topology, as indicated in Figure 2.9(b). This converter is developed using a boost and buck basic topologies cascade connected. The Cuk converter is shown in Figure 2.9(c); its work mimics the buck-boost converter. The common terminal of the input voltage is employed with reverse polarity so that the Cuk converter can step up or down input voltage. The SEPIC shown in Figure 2.9(d), also has the same features of a buck-boost converter: possesses a non-inverting output polarity and step up & down the input voltage [22].
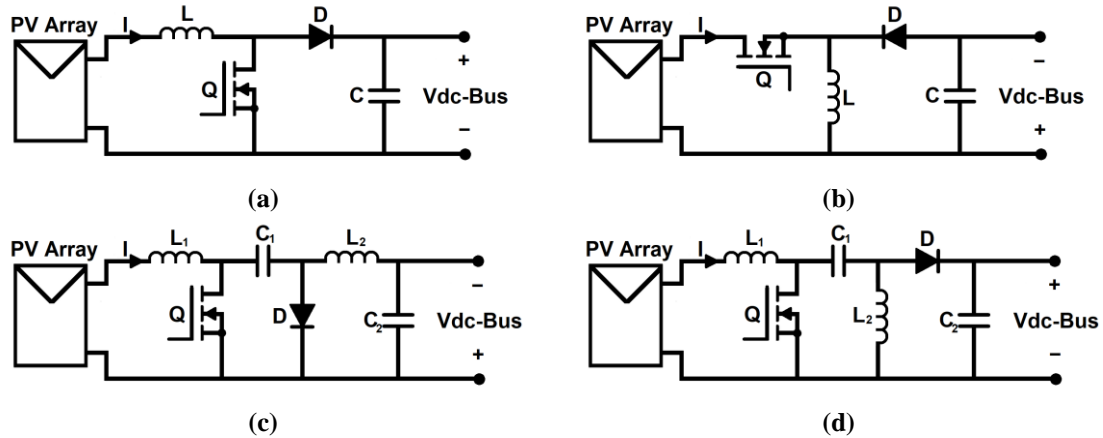
Figure 2.9. Schematic diagram of non-isolated DC-DC converters. (a) Boost converter; (b) Buck-Boost converter; (c) Cuk Converter; (d) Single-ended primary-inductor converter (SEPIC) [22], [122].

Table 2.4 describes the main advantages, disadvantages and applications of the aforementioned converters used in the PV stage.

Table 2.4. Comparison of non-isolated DC-DC converters for the PV stage.

Ref.	DC-DC Topology	Advantages	Disadvantages	Applications
[22], [99], [115]	Boost Converter	• The reverse current is blocked by the free-wheeling diode • It is remarkably the most effective topology at any price • Less ripple on output side • Cheaper filter components • It has output non-inverted polarity	• MPP cannot be tracked under low irradiation conditions • It has a non-operational region • It cannot achieve values near the modules' V_{OC}	• Not suitable for high variability environmental conditions • Low input voltage • High output voltage required
[22], [99]	Buck-Boost Converter	• This converter can operate in any operating region of the PV module (from I_{SC} to V_{OC}) • It is the only topology capable of tracking load resistance • It is able to track the modules' MPP at varying conditions of irradiance, temperature and load	• There are many harmonic components in the input current • It has a high input voltage ripple • It has substantial noise issues • It is more complex and expensive • It has a high current and voltage stress on the switch • Cost is inversely proportional to efficiency • Lower efficiency than the boost converter • The switch drive is floated • It has output inverted polarity	• Used for charging systems
[22], [99]	Cuk Converter	• This converter can operate in any operating region of the PV module (from I_{SC} to V_{OC}) • Prevent large harmonics at the input	• High number of passive components • It has high electrical stresses on the devices • The switch drive is floated	• Low voltage DC supply for electric vehicles

		• It is more reliable and less noisy than other topologies due to the inductors at the input and output	• It has output inverted polarity	
[22], [99]	SEPIC Converter	• It has output non-inverted polarity • The switch drive is grounded, simplifying the gate-drive circuitry • Less ripple on input side due to the continuous input current • This converter can operate in any operating region of the PV module (from I_{SC} to V_{OC})	• More ripple on output side • Medium efficiency • Most expensive than the other topologies • High number of passive components	• Low power charger systems

2.3.3 *Bidirectional DC-DC Converters*

The main purpose of a DC-DC converter is to regulate the output voltage and current on the common DC bus to suit the current required to charge the battery [13]. Several topologies are discussed on the literature [13], [61], [97], [98]. These topologies are classified into isolated and non-isolated DC-DC converters. However, isolated converters are more preferred than non-isolated types because of the high gain and galvanic isolation [13].

A) Non-Isolated Charger Topologies

The following are the non-isolated bidirectional converter topologies that will be analyzed:

- Bidirectional buck - boost converter with coupled inductors (Figure 2.10(a))
- Zero-Voltage-Switching (ZVS) interleaved half-bridge (HB) converter (Figure 2.10(b))
- HB converter with resonant circuit (Figure 2.10(c))
- Zero-Voltage-Transition (ZVT) interleaved converter with resonant circuit (Figure 2.10(d))
- ZVS HB converter with coupled inductors (Figure 2.10(e))
- 3-Phase interleaved buck converter (Figure 2.10(f))
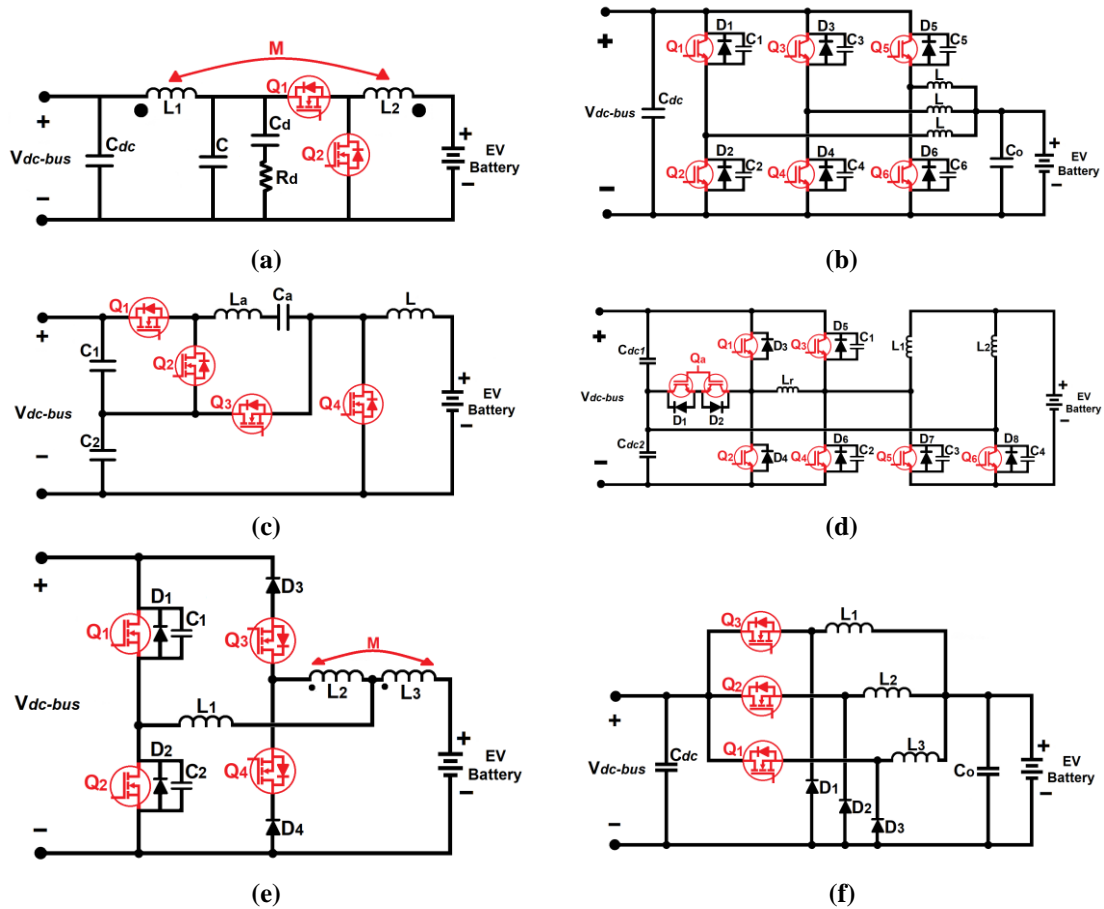
Figure 2.10. Schematic diagram of non-isolated bidirectional DC-DC converters. (a) Bidirectional buck - boost converter with coupled inductors; (b) ZVS interleaved HB converter; (c) HB converter with resonant circuit; (d) ZVT interleaved converter with resonant circuit; (e) ZVS HB converter with coupled inductors; (f) 3-phase interleaved buck converter [13], [97], [106], [107], [123]–[128].

Table 2.5 presents a comparison of the main characteristics of the aforementioned non-isolated bidirectional DC-DC converters used in the EV charger stage.

Table 2.5. Comparison of non-isolated bidirectional DC-DC converter topologies.

Ref.	Charger Topologies	Advantages	Disadvantages	Applications
[13], [98], [106], [123], [124]	Bidirectional Converter with Coupled Inductors	• Step down/up functions • It does not require an extra filter circuit since the coupled inductor acts as a filter • A smoother control is offered by the coupled inductor • It has an efficiency of 95% when operating at rated power despite not having ZVS and Zero Current Switching (ZCS) • Least expensive than other topologies	• Faces the right half plane zero effect within the output voltage to duty cycle in continuous conduction mode (CCM) • The dynamic performance of the converter is limited • Require a floating drive since the switch is not near ground	• Low power solar PV charger • Solar PV power supply

28

[98], [104], [107]	ZVS Interleaved HB Converter	• The use of the snubber capacitor allows to achieve the soft switching turn off at negative voltage instead of zero • Turn on soft switching is achieved using a complementary gate signal control • The input ripple current is reduced • The inductor size is reduced due to the use of the interleaved technique	• It is the most expensive among the other topologies discussed	• High power low ripple power supply • Portable programable power supply
[13], [98], [125]	HB Converter with Resonant Circuit	• High voltage gain • Can handle high power in charge and discharge mode • Using the auxiliary resonant circuit, the ZVS and ZCS are implemented • Reduced voltage stress on the switches	• It has a reduced output voltage due to the equivalent series resistance (ESR) drop of the active and passive devices • The operation of couple inductors produce a considerable input current ripple	• Low cost battery continuous duty charging application • Uninterruptable power supply • Not suitable for high power applications
[13], [98], [126]	ZVT Interleaved Converter with Resonant Circuit	• The input ripple current is reduced by using the interleaving technique • High voltage gain • Low switch current and voltage stresses • The reverse recovery effects can be minimized since the rectifier diodes realize ZCS condition	• There are not drawbacks mentioned on the literature of the proposed topology	• Low ripple programable power supply • Robust closed loop control
[13], [98], [127]	ZVS HB Converter with Coupled Inductors	• For heavy loads, by selecting a ZVS mode, it is obtained a high efficiency • For light loads, by selecting a hard-switching mode, it is also obtained a high efficiency	• At light conditions the efficiency decrease • When the load decrease, the recycled energy increases	• Medium power constant load DC power supply
[97], [128], [129]	3-Phase Interleaved Buck Converter	• Efficiency is improved by using separate inductors • The current is shared between the multi-phase modules	• The number of phases is inversely proportional to the inductor size • In phase current, it has a high total harmonic distortion (THD)	• High power DC drive • Fast DC charger • Applications with isolated front low-frequency transformers

B) Isolated Charger Topologies

The following are the isolated bidirectional DC-DC converter topologies that will be discussed:

- ZVS Dual Active Bridge (DAB) Converter (Figure 2.11 (a))
- Phase-Shift Full-bridge (FB) Converter (Figure 2.11 (b))
- FB LLC Resonant Converter (Figure 2.11 (c))
- ZVS FB Converter with Capacitive Output Filter (Figure 2.11 (d))
- Interleaved Flyback Converters (Figure 2.11 (e))

(a)

(b)

(c)

(d)

(e)
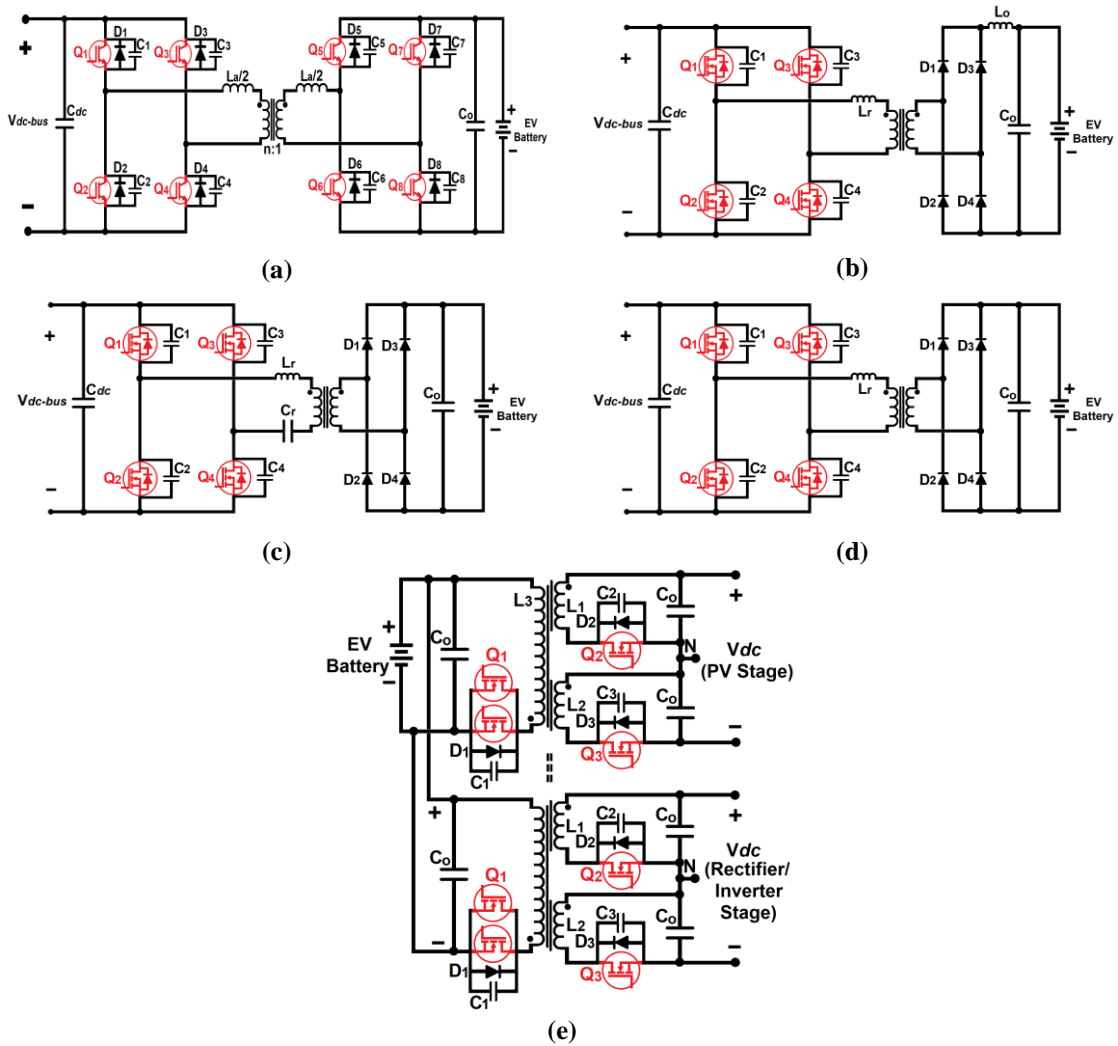
Figure 2.11. Schematic diagram of isolated bidirectional DC-DC topologies. (a) ZVS DAB Converter; (b) Phase-Shift FB Converter; (c) FB LLC Resonant Converter; (d) ZVS FB Converter with Capacitive Output Filter; (e) 4 Interleaved Flyback Convert [13], [98], [104], [108], [130]–[132].

Table 2.6 describes a comparison of the main characteristics of the above mentioned isolated bidirectional DC-DC converters common used in the EV charger stage.

Table 2.6. Comparison of isolated bidirectional DC-DC converter topologies.

Ref.	Charger Topologies	Advantages	Disadvantages	Applications
[13], [98], [130]	ZVS DAB Converter	• By using snubbers capacitors, ZVS mode can only be achieved for specific conditions • It has low switching losses	• Higher switching frequencies cause high turn-off losses • ZCS mode is not enabled	• High voltage applications • High level of reliability required
[97], [104], [133], [134]	Phase-Shift FB Converter	• Primary switches require soft-switching • Simple control • The freewheeling interval possess high current flow • Achieve higher efficiency that conventional FB topologies • The PWM control reduce switching losses and current stress on devices	• High voltage stress on the rectifier bridge • Hard switching losses and the loss of guarantee with ZVT operation are consequences of PHEV current requirements dropping below minimum critical output current value	• High power and high frequency applications
[61], [97], [131], [135]–[137]	FB LLC Resonant Converter	• It can achieve high efficiency in a full range of ZVS for primary switches, in high voltage operations and at the resonant frequency • No reverse recovery current in addition to an absent oscillation voltage across the rectifier diodes • The output voltage is able to be regulated during the hold-up time	• The transformer and filter designs are complex • When the battery voltage is low, its operation is less efficient	• Energy conversion systems • Power supply • PV applications
[61], [132]	ZVS FB Converter with Capacitive Output Filter	• The diode rectifier ringing is minimized inherently on the current fed topologies with capacitive output filter • At ZVS mode can achieve high efficiency (approx. 95.7%)	• Has reverse recovery losses in the secondary rectifier diodes • Has high voltage ringing	• High power applications
[108]	4 Interleaved Flyback Converter	• For bidirectional operation, the antiparallel diodes and MOSFETs are used on both sides of the transformer • As a result of the two MOSFETs connected in parallel on the secondary side, there was a reduction in conduction losses • Provides isolation as required by the EV charging standards • Use less switches than the DAB and resonant converter topologies • In both charging and V2G operation a quasi-resonance (QR) mode is operated • Cause a reduction in turn-on losses resulting from low-voltage switching (LVS) or ZVS • Turn-off losses approach zero, because resonant capacitors absorb turn-off energy	• It is more expensive than other topologies due to the transformer used • The topology is more robust	• Suitable for low power applications, however the research made by [108] concluded that when using SiC devices in a QR mode, high efficiency at high powers can be achieved

Single-Stage Conversion (Z-Source Inverter)

Single-phase Z-source inverter has been discussed in the literature [71], [110], [112]. The schematic of the Z-Source inverter is shown in Figure 2.12. One of the main advantages of the Z-converter is the double modulation capability, in addition to that while regulating the charge of the EV battery, it can simultaneously shape the grid current [71].
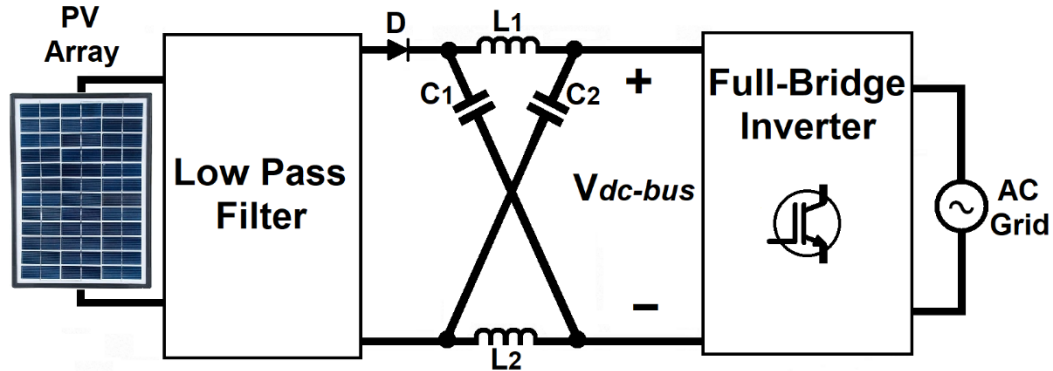
Figure 2.12. Schematic diagram of a Z-source Inverter (ZSI) for PV/grid-tied system [112].

A single-phase modified Z-source inverter (ZSI) topology was proposed by Singh [112]. According to Singh in his proposed topology, the capacitor voltages vary between twice the minimum battery voltage up to twice the fully charged battery voltage when battery voltages vary between 200 – 500 V. The converter operates between D_{0min} to D_{max} for v_{pvmax} to v_{pvmin} respectively. The proposed cascaded configuration system has the following advantages [112]:

- Single point of fault is avoided.

- ZSI has a packed structure due to the decreased number of stages.

- Galvanic isolation is feasible between the charger side and the PV and Grid.

- Presents an opening to step up the charging power levels by adding such converters.

- Any battery voltage levels can be charged by changing the charger side of the converter between voltage sharing or current sharing.

2.4 Snow Removal Functionality for Solar PV Panels

As it was mentioned before in Section 1.1, many studies have been developed on the effects of snowfall on solar PV systems since this is one of the main factors affecting the performance of PV systems in cold areas [21], [26]–[28], [30]–[44].

Powers et al. [26] developed a research that consisted in the installation of three pairs of PV modules with tilt angles of 0°, 24°, and 39°, fixed south-facing, installed in Truckee, California. To identify the energy loss in the system, one of each pair of PV modules was kept clear of snow manually. The analyzed data showed an average monthly snow depth of 5 m, however, a high variability per month and per year of up to 300% was observed. The study concluded that the energy loss during the months of November to May (2009-2010) was 42%, 33% and 25% for the tilt angles of 0°, 24° and 39°, respectively. Besides, annual energy losses of around 18%, 15% and 12% were estimated for the three cases mentioned above.

Pawluk et al. [39] presented a summary of different studies developed in various cities around the world. The monitored facilities had PV modules oriented at different tilt angles ranging from 0° to 90°. From the results it can be concluded that the annual energy loss depends on many factors, such as the annual depth of snowfall, the tilt angle of the PV module, the snow slide obstructions around the module and, in general, climatic factors, like wind and temperature of the location. For example, a study carried out in Calumet, Michigan and in Boulder, Colorado with installations of PV modules oriented to the same tilt angle (15°) presented completely different results. While at Calumet the annual snow depth was 5.3 m, at Boulder it was only 0.89 m. In this way, the annual energy losses presented in both places were 34% and 6%, respectively.

Regarding the methods used for snow removal in solar PV systems, various active and passive solutions were found in the literature [42], [47], [51], [53], [56]–[58], [138], [139]. They included:

- Hydrophilic and superhydrophobic surfaces

- Black absorbent coatings on the solar PV panel

- Mechanical removing methods

- Mobile robots

- Resistive electrical cables placed behind the solar PV panel

- Reverse current using external power sources

Weiss and Weiss [51] proposed two different circuit models for a current-controlled heating solution. One of the proposed circuits included a boost converter transformed into a synchronous buck converter to allow reverse current flow in the direction of the solar PV panel, with an additional external switch to control an electrical resistance that will heat the aluminum frame of the solar PV panel. The second proposed circuit included the boost converter that will allow to extract the MPPT of the solar PV panel and will feed a battery and again the external switch that controls a foil resistor for heating the aluminium frame of the PV panel. Both circuits are connected to a battery which will provide the current required for the system to heat the solar PV panel. However, a final prototype of these proposed circuits was not provided, nor was it discussed in detail.

Chapter 3. Bidirectional Buck-Boost DC-DC Converter with Snow Removal Functionality

This chapter proposes a bidirectional DC-DC converter capable of extracting the maximum power point (MPPT) of a solar PV array to charge a battery pack. The proposed system, in addition to allowing a current flow direct to the battery, is also designed to provide a reverse current flow to heat the solar cells of the solar PV array. This function will allow snow melt in severe winter conditions, thus improving the annual efficiency of any off-grid or grid connected PV-EV charger system.

3.1 Proposed System

The most common structure of a solar PV system for electric vehicle charging applications is depicted in Figure 3.1. However, for our purpose the unidirectional DC-DC converter connected between the solar PV array and the DC bus was replaced by a bidirectional DC-DC converter. Figure 3.1(a) show a grid-connected system; the system is integrated by a solar PV array and an EV battery pack connected through a bidirectional DC-DC converter to the DC bus, which feeds a bidirectional DC-AC converter for grid-connected operation. On the other hand, an off-grid system is shown in Figure 3.1(b). The solar PV array feeds a battery energy storage through another bidirectional DC-DC converter instead of the bidirectional DC-AC converter shown in Figure 3.1(a).
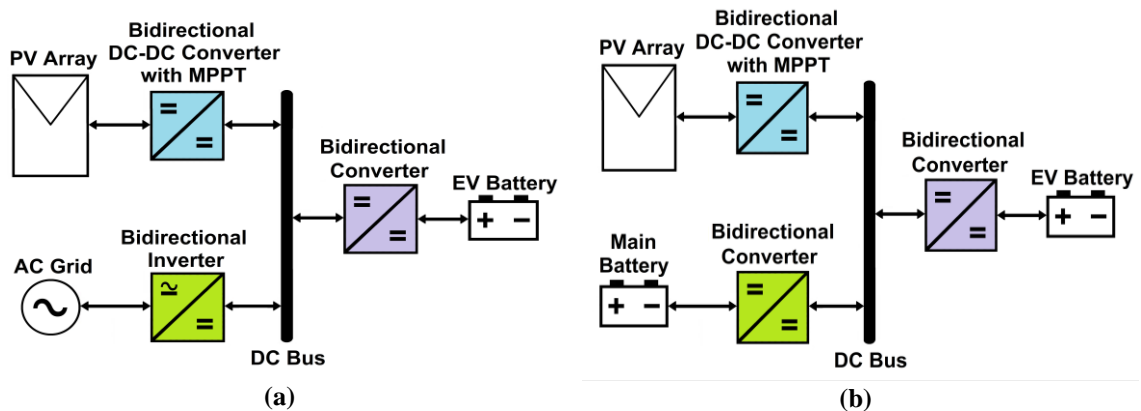
Figure 3.1. Solar PV system architecture for EV charging with snow removal functionality. (a) grid-connected system; (b) off-grid system.

The main focus of this thesis is the modeling, analysis and design of the bidirectional DC-DC converter with MPPT (highlighted in blue in Figure 3.1 (a) and (b)), which will allow the power transfer to charge the EV battery pack and a reverse flow of current to produce heat on the solar cells that will melt the snow over the solar panels in winter time.

3.2 System Design Considerations

There are several design considerations that must be assumed in the design process. The following are the most important factors to consider:

1. **Maximum power capacity of the system:** It is very important to determine the nominal power of the solar PV array according to the need of the system and the space available to place the solar PV array. In addition to the size of the solar PV array, it is also important to define the conversion efficiency of the solar panels to be used. At the same time, the nominal power of the battery pack to be charged and discharged must be considered.

2. **Maximum capacity of the battery**: There are some other parameters to consider such as the maximum open circuit voltage of the battery pack under a full charge condition and the maximum capacity of the battery pack which is determined by the maximum safe current level in which the battery is charged and discharged at. The maximum C-rating of the battery is directly proportional with its capacity.

3. **Power conversion system topology**: This factor is really important as it determines the capabilities of the system. For the proposed application, a topology is required that allows power flow in both directions, along with other conditions that will be described in the following sections.

4. **Safety requirement and other conditions**: Last but not least is the protection capability of the system and safety requirements. One of the limitations when connecting solar PV panels is that the maximum voltage cannot reach 600 VDC, according to the manufacturer's specifications. Also, since batteries are being used in the system, it is important to use the proper protection gears to avoid any damage or explosion of the energy storage devices. They must be protected against over currents or short circuits and over

voltages or under voltage. Likewise, it is important to protect all devices from overheating, such as solar panels, which lose efficiency due to high temperatures or in the case of the energy storage devices [71], [140].

3.2.1 *Photovoltaic Design Considerations*

Determining the design considerations for the solar PV array is very important, since it will allow us to know what is the nominal power that would be available for the EV charging station. It is imperative to consider the following factors, when defining the solar array characteristics:

- The area available;

- The size and efficiency of the solar panels.

To define the first factor, the laws/standards that regulate the maximum space of a parking space will be considered to calculate the available area of a solar powered charging station. According to the Zoning By-law 569-2013 of the City of Toronto, that includes the Parking Space regulations, the minimum dimensions of a parking space are 5.6 m (length) by 2.6 m (width) and the maximum dimensions for a parking space are 6.0 m (length) by 3.2 m (width) in Ontario [141]. For this study, the maximum dimensions of the parking space will be considered to calculate how many solar PV panels will be used, nevertheless, to obtain a greater capacity it is recommended to use a much larger area.

However, before continuing to calculate that, it is necessary to consider the second factor, the size and efficiency of the solar panels. In this study, there will be used Trina solar panels, model TSM-245-PA05 (245 W). These solar panels were provided by the company "*Upstartz* Energy Ltd.", who participated as a sponsor in this study. The characteristics of the solar PV panel are shown in Table 3.1.

Although there are solar panels on the market with up to 22.6% efficiency [142] that could increase the capacity of the installation, these solar panels will be used to proof the concept.

Table 3.1. Solar panel characteristics [143].

Solar PV Panel Model	Trina Solar TSM-245-PA05
Solar Cells Type	Multicrystalline
Peak Power (P_{MAX})	245 Wp
Power Output Tolerance	+/- 3%
Open Circuit Voltage (V_{OC})	37.5 V
Short Circuit Current (I_{SC})	8.68 A
Maximum Power Voltage (V_{MPP})	30.2 V
Maximum Power Current (I_{MPP})	8.13 A
Temperature Coefficient of P_{MAX}	-0.43 %/°C
Temperature Coefficient of V_{OC}	-0.32 %/°C
Temperature Coefficient of I_{SC}	0.047 %/°C
Solar PV Panel Efficiency (η_m)	15%
Solar PV Panel dimensions	$1650 \times 992 \times 35$mm

* Values at Standard Test Conditions STC (Air Mass AM1.5, irradiance 1000W/m², Cell Temperature 25°C).

In fact, if the Maxeon Gen III monocrystalline solar cells which have an efficiency of 22.6% are considered, using a solar irradiance level of 1000 W/m^2, the maximum available power that the solar array will provide will be about:

$$P_{PV} = 1000 \, W/m^2 * 19 \, m^2 * 22.6\% = 4.29 \, kW$$

It is important to mention that the maximum power shown in the above table will be provided by the solar PV panels only under good weather conditions and during a limited time of the day.

Now, using the maximum dimensions for a parking space (6.0 m by 3.2 m), which is an approximate area of 19 m^2, the maximum number of solar PV panels to use can be calculated (in the case this is the only area available). There were made two analysis for placing the solar PV panels on the charging station. The solar PV panels can be tilted 40˚ with a south orientation, to allow greater efficiency. On the first case, when placing the solar PV panels in a vertical position (the smaller side is placed on the bottom), it will allow the use of 6 solar PV panels as shown in Figure 3.2 (a). On the other hand, when placing the solar PV panels in a horizontal position (the longer side is placed on the bottom), the use of 9 solar PV panels would be allowed as shown in Figure 3.2 (b).

| | (a) | (b) |
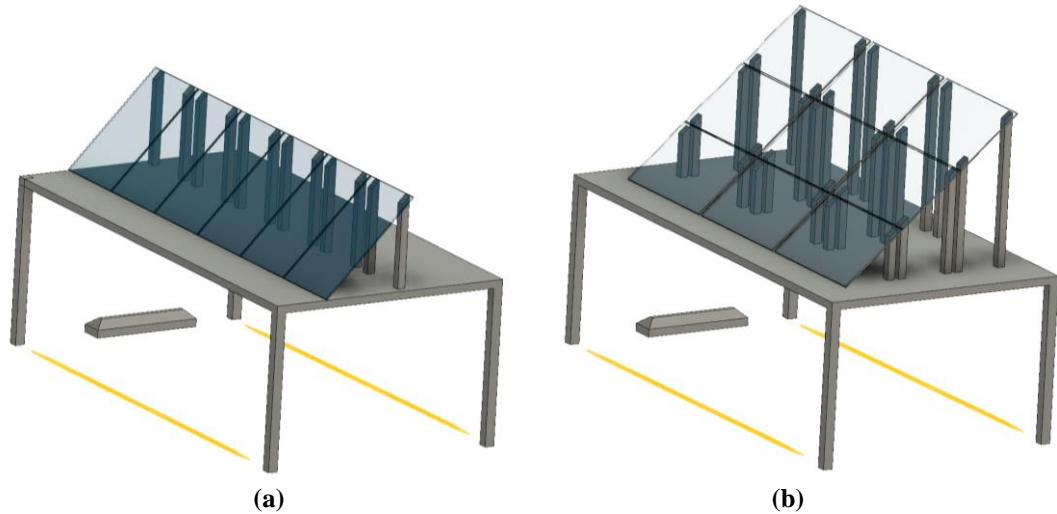
Figure 3.2. Solar array design. (a) 6 solar panels in vertical position; (b) 9 solar panels in horizontal position.

The following table shows the characteristics of the two solar array options. For both cases, a single string of solar panels connected in series was considered.

Table 3.2. Characteristics of the two solar array options.

	Solar Array of 6 Panels	Solar Array of 9 Panels
Area	9.82 m^2	14.73 m^2
Peak power	1.47 kW	2.2 kW
Voltage at MPP (series-connected)	181.2 V	271.8 V
Current at MPP (series-connected)	8.13 A	8.13 A

The characteristic current-voltage I-V and power-voltage P-V curves of the solar panel selected for different irradiance levels are presented in Figure 3.3 (a) and (b) respectively. The irradiance for each condition shown goes from 0 kW/m^2 to 1 kW/m^2. The maximum power point (MPP) for each irradiance is shown in Figure 3.3 (b) denoted by a circle. In the figure below, it can be seen that at an irradiance of 1 kW/m^2, the MPP is found at 245.53 W, with a voltage at the maximum power of 30.2 V and a current at the maximum power of 8.13 A.
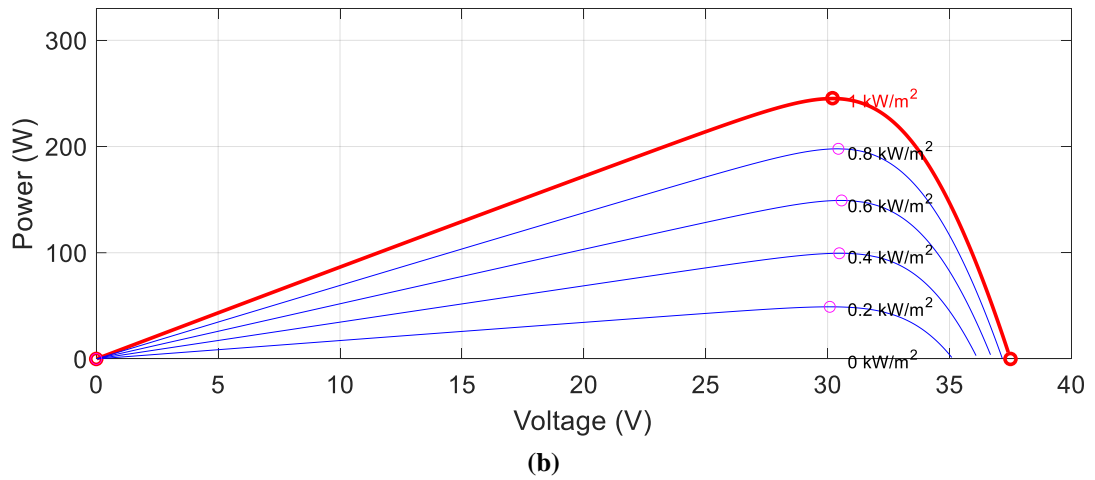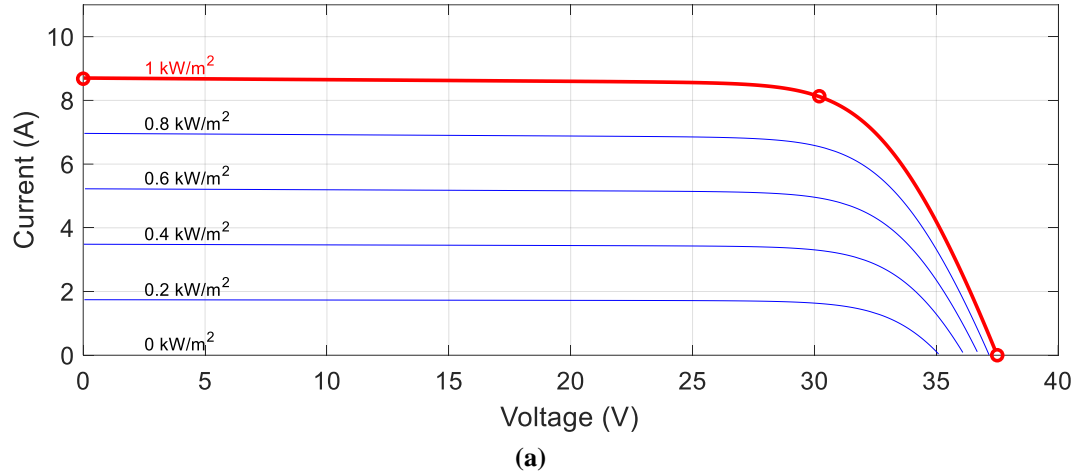
Figure 3.3. Characteristic Curves of PV module TSM-245-PA05. (a) Solar panel I-V curve; (b) Solar panel P-V curve.

However, the system proposed is compound of an array of 9 solar PV panels connected in series. Therefore, the MPP of the array is higher, keeping a constant current with an increased voltage at the maximum power. The I-V and P-V characteristic curves of the solar PV array for different irradiance levels are presented in Figure 3.4 (a) and (b) respectively. As before, the irradiance for each condition shown goes from 0 kW/m^2 to 1 kW/m^2. In this case, it can be seen that at an irradiance of 1 kW/m^2, the MPP is found at 2209.73 W, with a voltage at the MPP of 271.8 V and a current at the MPP of 8.13 A.
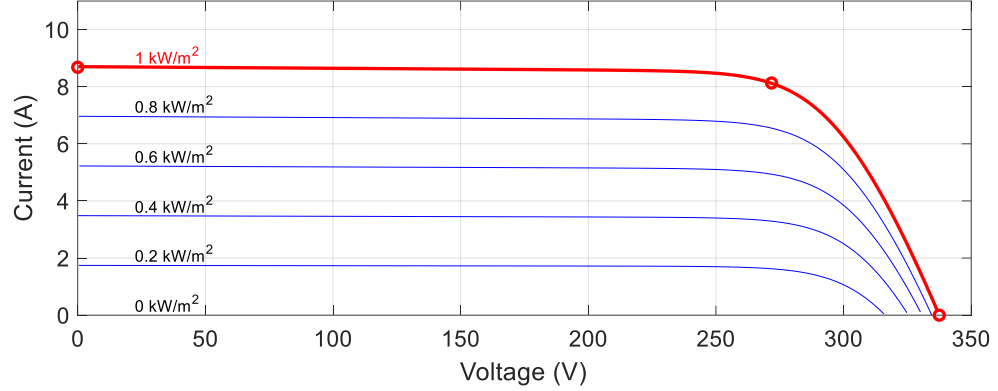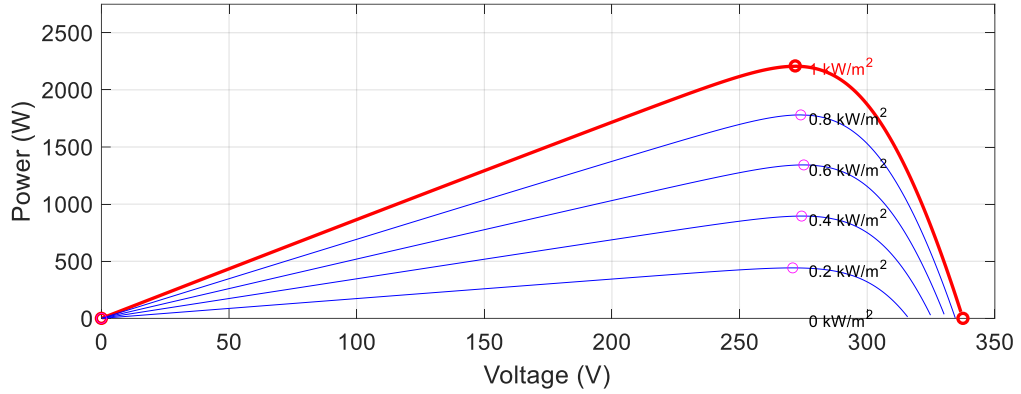
Figure 3.4. Characteristic curves of PV array of 9 TSM-245-PA05 solar PV modules series connected. (a) Solar PV array I-V curve; (b) Solar PV array P-V curve.

Using the main specifications of the solar panel mentioned above, the PV array can be modeled as explained in Section 2.2.1. The values for the equation of the simplified single diode model were identified by using the curve fitting tool of MATLAB. Then, the non-linear model of the PV array can be expressed as [77], [78]:

$$I_{pv} = 8.68 - 6.076 \cdot 10^{-6} e^{0.04199 \cdot Vpv} \tag{3.1}$$

However, as mentioned above, this model can only be used for electrical simulation purposes and not for control design. Therefore, a Norton equivalent circuit was calculated when the PV solar array is under standard conditions (irradiance equal to 1000 W/m² and ambient temperature equal to 25°C), obtaining the equivalent resistance R_{pv} as a result:

$$R_{pv} = \frac{271.8}{8.68 - 8.13} \Omega = 494.1818 \, \Omega \tag{3.2}$$

A comparison between the non-linear model and the linear model (Norton equivalent) of a solar PV array at its MPP under standard conditions is shown in Figure 3.5. The single-

diode simplified model is represented by the red line and the Norton model is represented by the blue line.
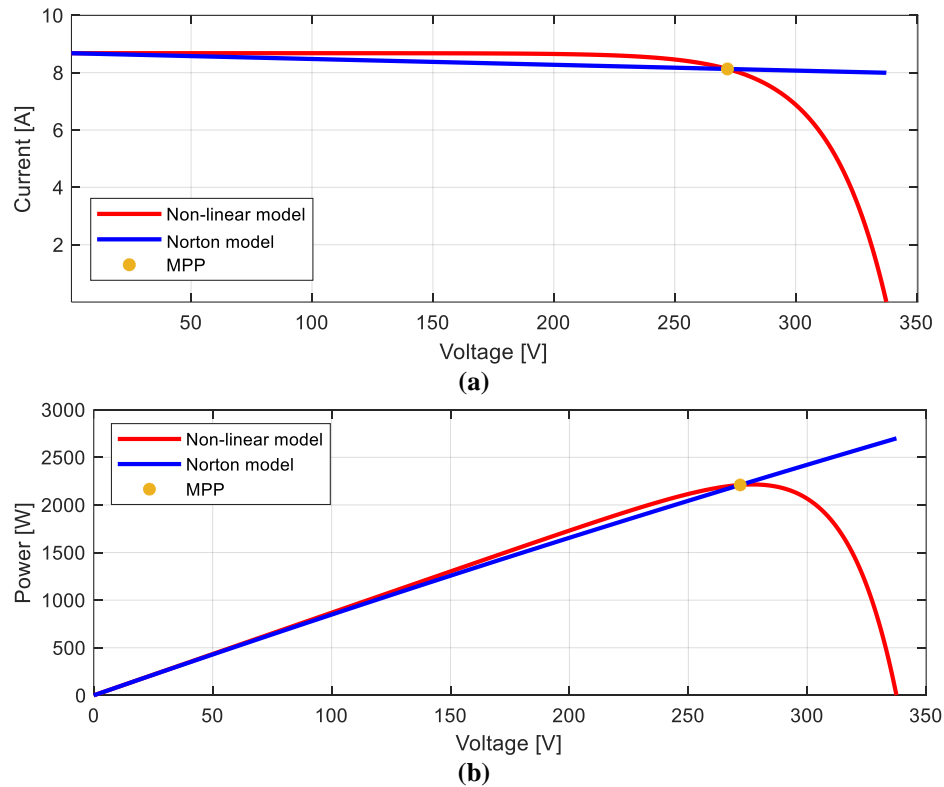
Figure 3.5. Comparison of I-V and P-V characteristic curves for the non-linear and linear models of the solar PV array calculated. (a) I-V Characteristic curve; (b) P-V characteristic curve.

From the previous figure, it can be concluded that the Norton model is a very accurate representation of the non-linear model at the MPP and very close for values lower than the MPP. Therefore, this model can be used for simulation and control design purposes.

3.2.2   Proposed Power Conversion Topology

As mentioned above, a power conversion topology is required that can be used in EV charging applications connected to solar PV panels. Moreover, it must be capable of extracting the maximum power point from a solar PV array to charge a battery pack as needed.

At the same time, the power conversion system must be able to provide a flow of energy in the opposite direction to provide reverse current into the solar PV array when needed. This will generate heat to melt the snow when the solar panels are covered with

snow in the winter time, aiming to improve the efficiency of the system. The power conversion system will be fed by discharging a backup battery pack via a bidirectional DC-DC converter in an off-grid system or via the power grid through a bidirectional DC-AC converter on a grid-connected system. Therefore, the converter topology used must have a bidirectional function.

Additionally, the power conversion system topology must be capable of handling voltage variations at the input and output of the system within a specified range. This due to the variable insolation obtained during the day, causing the voltage of the solar PV array to not be constant. In the same way, since the output is connected to a battery pack, the output voltage will also vary continuously. However, the input voltage will never exceed the output voltage. This means that the power conversion system must works as a boost converter in one direction and as a buck converter in the opposite direction.

Based on all the characteristics mentioned above, a controlled bidirectional buck-boost DC-DC converter, also known as bidirectional half-bridge converter (BHBC) or synchronous buck converter (SBC) has been chosen to be used for this application. A non-isolated topology was chosen because it is cheaper than the isolated topologies, and have less components. A part from that, the SBC has the advantage of keeping the same electrical reference for the input and output ports [144]. However, its main drawbacks are the pulsating current in the higher voltage port and the lack of insulation [144]. In Figure 3.6 it is shown the overall structure of the solar PV system with snow removal functionality for off-grid and grid-connected EV charger applications.
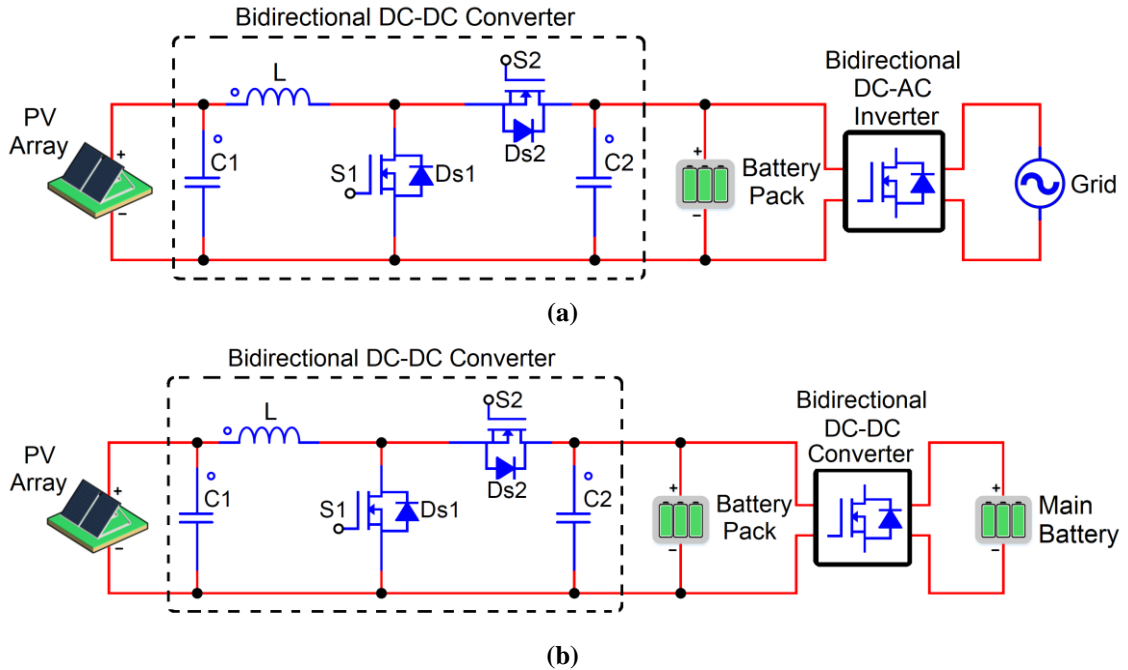
Figure 3.6. Overall structure of the solar PV system with snow removal functionality for off-grid and grid-connected EV charger applications. (a) grid-connected; (b) off-grid.

In order to proof the concept of functionality of the proposed bidirectional converter, it will be assumed that the voltage at the dc bus where the EV battery pack is connected, will be regulated by either the bidirectional AC-DC converter in the case of the grid-connected system; or by the bidirectional DC-DC converter that interconnects the battery pack and the main battery in the case of the off-grid system. Hence, the main battery/grid will serve as a power source to supply the reverse current flow necessary to heat the solar cells of the solar PV array, performing the snow removal functionality of the system.

For this application, the system is only composed of 2 stages, unlike the 3 stages used by the most common systems like the one shown in Figure 3.1. In this case, the bidirectional DC-DC converter connecting the EV battery pack to the DC bus was combined together with the unidirectional DC-DC converter with MPPT used for the solar PV array. In this way, the converter proposed will fulfill the functions of extracting the maximum power point, charging the battery, and additionally regulating the appropriate current level required for the solar PV array to melt the snow when necessary.

Although both systems showed above, i.e. grid-connected and off-grid, are composed of two bidirectional converters, this thesis only focuses on the analysis, design and modeling of the proposed bidirectional buck-boost DC-DC converter.

3.3 Analysis and Operation of the System

In the following sections, the modes of operation of the proposed converter and an example of an off-grid application will be explained in more detail.

3.3.1 Modes of Operation of the System

Figure 3.7 shows a block diagram of an off-grid PV solar EV charging system, which will be used as an example to analyze the operating modes of the entire system.
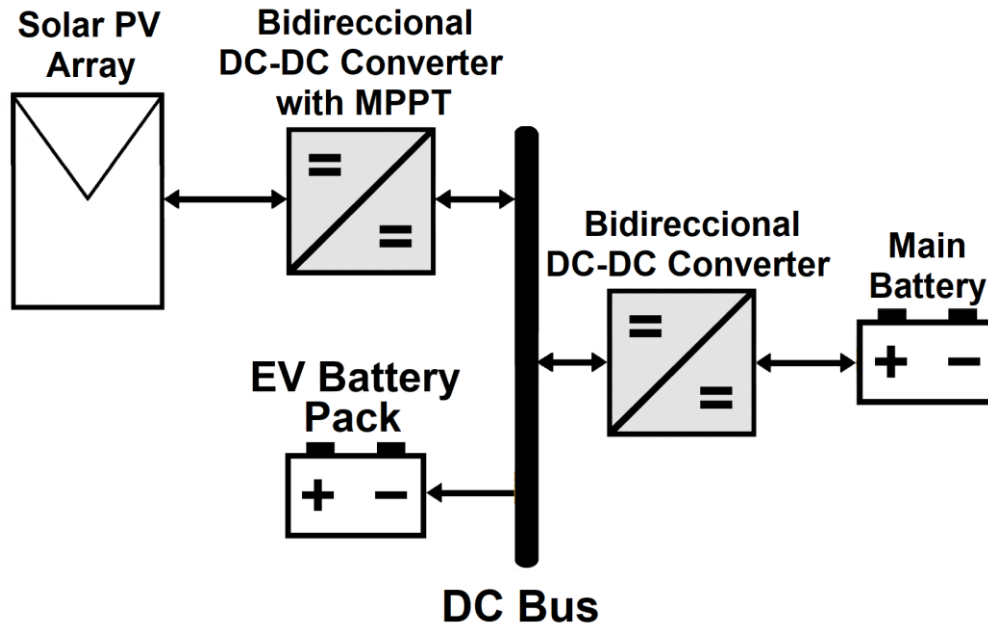
Figure 3.7. Block diagram of the off-grid solar PV EV charging system.

This application has 4 modes of operation that are shown in the Figure 3.8. Modes of operation include EV battery charging via solar PV array as shown in Figure 3.8 (a); EV battery charging via main battery as depicted in Figure 3.8 (c); power transfer from solar PV array to main battery as shown in Figure 3.8 (b); and snow removal function via reverse current flow towards the solar PV array as shown in Figure 3.8 (d).
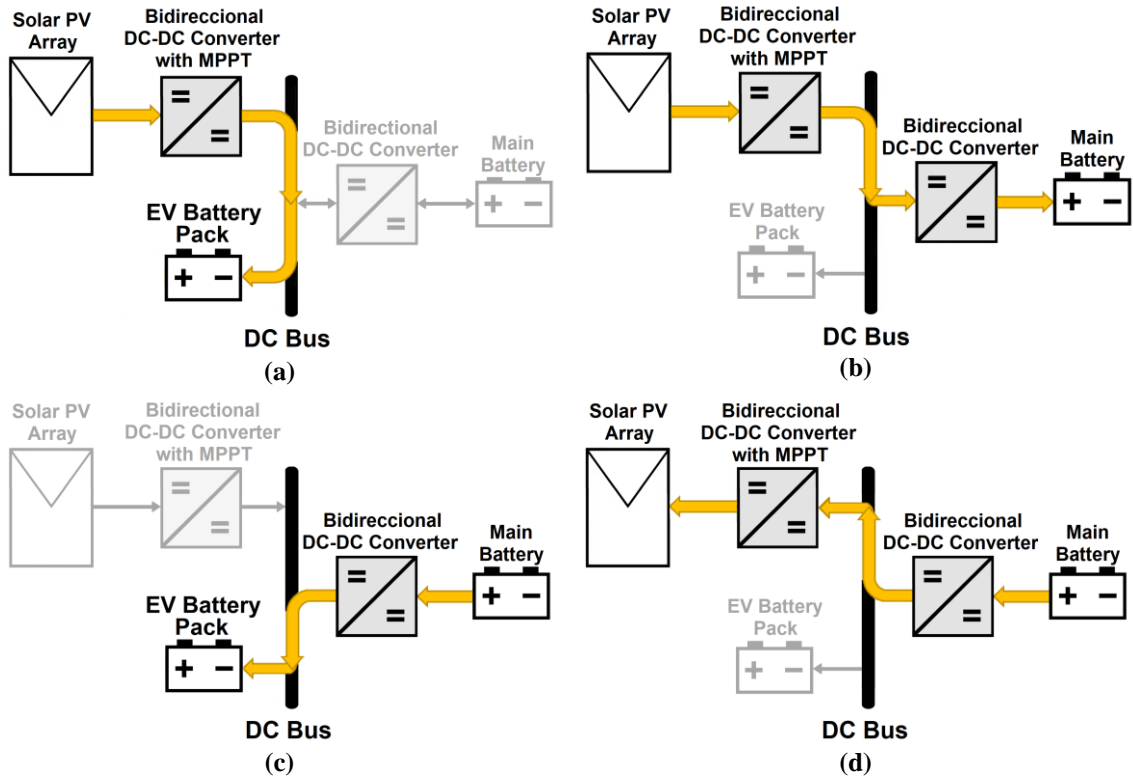
Figure 3.8. Modes of operation of the system. (a) Solar PV array to EV battery pack (charging EV battery); (b) Solar PV array to Main battery (charging energy storage); (c) Main battery to EV battery pack (charging EV battery); (d) Main battery to Solar PV array (reverse current flow).

This thesis will focus only on the modes of operation (a) and (d) described in Figure 3.8, since these are the ones that describe the operation of the proposed converter. Therefore, the main results of this thesis will include:

- Extracting maximum power point from the solar PV array to charge the EV battery pack;

- Providing reverse current flow to the solar PV array to heat the solar cells and as a result melt the snow covering the solar panels.

Since the literature covers many methods and topologies used to charge a battery using another backup battery, this will not be included in the thesis. Therefore, only the mathematical modelling of the proposed bidirectional converter will be included.

3.3.2 *Modes of Operation of the Proposed Bidirectional DC-DC Converter*

Figure 3.9 depicts the circuit diagram of the bidirectional buck-boost DC-DC converter. This converter interfaces the solar PV array and the EV battery pack. Depending on the operating scenario, two modes of operation can be set: boost and buck mode. The converter operates with two controllable switches (S_1, S_2); the operation of the two switches is complementary, meaning that when one is ON the other must be OFF. Depending on the maximum duty cycle, it will operate in boost mode when switch S_1 is triggered, while buck mode will operate when switch S_2 is triggered. An inductor L_1 at the input provides a non-pulsating current and can have a direct power transfer from source to load (EV battery pack). It is important to consider preventing the simultaneous conduction of both switches. The controller must ensure that both switches are not turned on simultaneously as this would place a very small parasitic resistance between the input and ground and destructive currents could flow through the switches. It must be ensured that there is a dead time in which both switches are off [145]. The bidirectional buck-boost DC-DC converter has three equivalent circuits for each mode of operation [146]. These will be explained below.
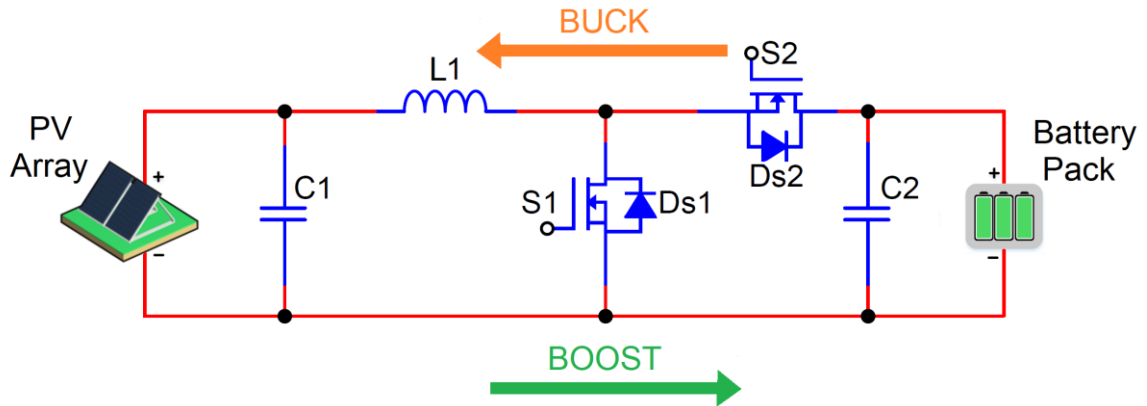
Figure 3.9. Modes of operation of the proposed converter (boost + buck).

a) **Boost Operation Mode**

In this mode of operation, the input voltage is always lower than the output voltage. This mode of operation will allow the power transfer from the solar PV array to charge the EV battery pack or if there is no EV battery pack connected to the system, it will allow the charging of the main battery, which acts as a backup energy storage as shown in Figure 3.8 (a) and (b).

Figure 3.10 depicts the three equivalent circuits when the converter is operating in Boost mode. The states are described as: ON time, when switch S1 is closed; DEAD time, when both switches S1 and S2 are open; and OFF time when switch S1 is open.

Figure 3.10 (a) shows the equivalent circuit of the converter during the ON time state, when switch S1 is closed. Since the two switches are complementary, switch S2 located on the high-voltage side is open. During the ON state, the inductor L1 is storing energy, therefore its current increases positively.

As it was mentioned before, both S1 and S2 switches cannot operate at the same time; therefore, it was included a state when both switches are open to allow the transition to the OFF state of switch S1 and ON state of switch S2. The equivalent circuit for this state is shown in Figure 3.10 (b). When both switches S1 and S2 are not conducting, the internal diode DS2 of the MOSFET S2 goes into operation transferring power from the source to the load, which in this case is the EV battery pack. However, diode DS1 is in the off state since it is reverse biased. The current flowing through the inductor L1 starts falling causing a back electromotive force (EMF) inducing a voltage across the inductor L1 in the opposite polarity to keep the current flowing. This energy stored is released towards the load [140]. This state of operation happens twice, when the switches are transitioning between ON state to the OFF state and vice versa.

Figure 3.10 (c) illustrates the equivalent circuit of the OFF-time state, when switch S1 is open. Switch S2 is closed allowing a direct power transfer from the solar PV array to the EV battery pack. During this state inductor L1 continues releasing its stored energy towards the load. Once the inductor has provided half of its stored energy to the load and the capacitor, the voltage in the load begins to drop and the stored energy in capacitor C2 begins to be released. In this way the current keeps flowing through the load until the ON period starts again.

(a)

(b)

(c)
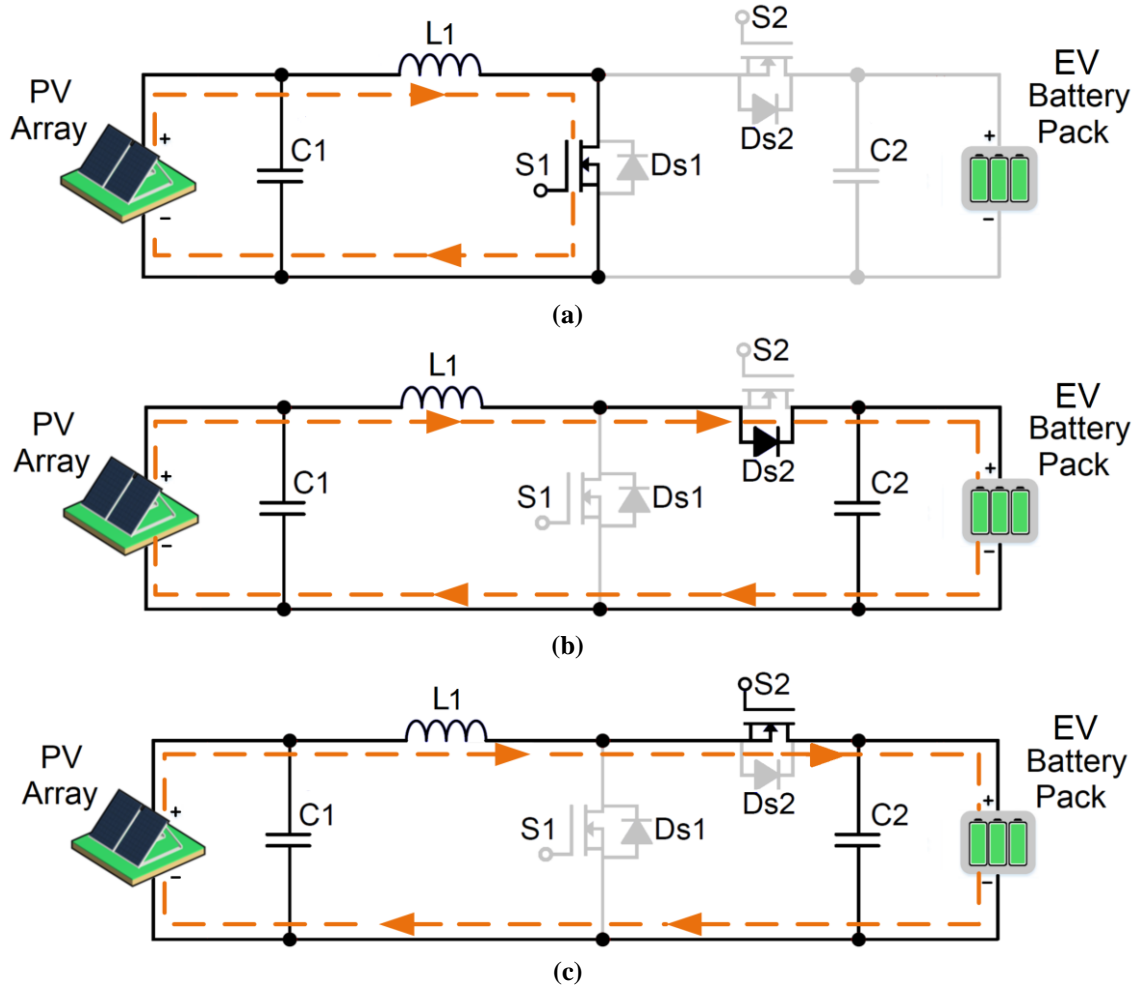
Figure 3.10. Converter operating in Boost mode. (a) Switch S1 during ON time ($0 \leq t \leq DT$); (b) Switch S1 and S2 during DEAD time ($DT \leq t \leq T_{dead}$); (c) Switch S1 during OFF time ($T_{dead} \leq t \leq (1-D)T - T_{dead}$).

b) Buck Operation Mode

In this mode of operation, the input voltage (EV battery pack side / DC bus) is always higher than the output voltage (solar PV array side). This mode of operation will allow the power transfer from the DC bus, where the EV battery pack and the main battery is connected through a DC-DC converter, to provide a reverse current flow towards the solar PV array that will produce heat in the solar cells to melt the snow in the winter season as shown in Figure 3.8 (d).
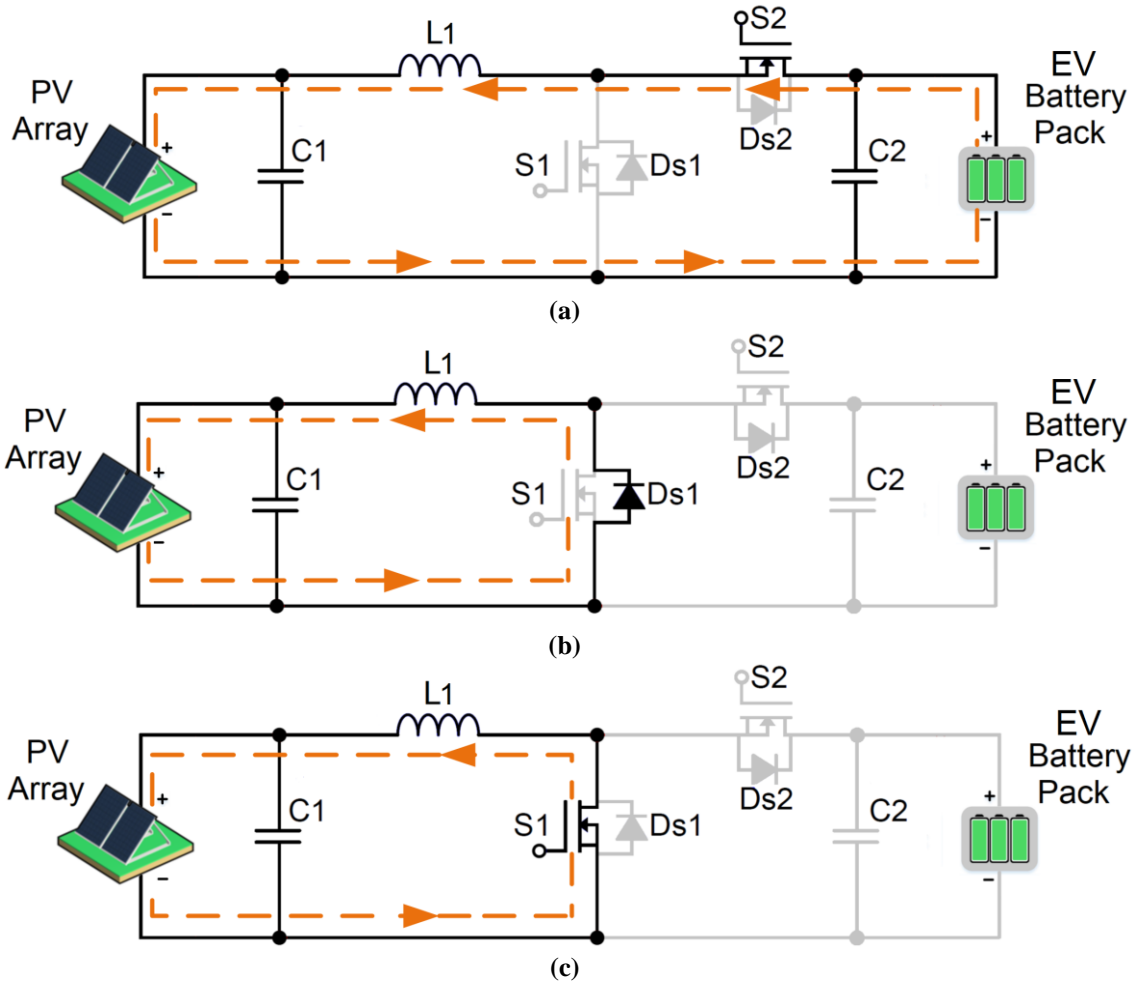
Figure 3.11. Converter operating in Buck mode. (a) Switch S2 during ON time ($0 \leq t \leq DT$); (b) Switch S1 and S2 during DEAD time ($DT \leq t \leq T_{dead}$); (c) Switch S2 during OFF time ($T_{dead} \leq t \leq (1-D)T - T_{dead}$).

Figure 3.11 depicts the three equivalent circuits when the converter is operating in Buck mode. The states are described as: ON time, when switch S2 is closed; DEAD time, when both switches S1 and S2 are open; and OFF time when switch S2 is open.

During ON time switch S2 is closed and switch S1 is open as shown in Figure 3.11 (a). The power provided by the main battery to the DC bus, now is supplying power to the load, which in this case is the solar PV array. In this scenario there is direct power transfer from the source to the load. Initially, the energy is being stored by the inductor L1, limiting the current flow towards the load. However, the voltage in the capacitor and the load starts rising gradually.

50

During the DEAD time, both switches S1 and S2 are open. In this state, the internal diode DS1 of the MOSFET S1 comes into operation conducting current to the inductor L1. However, due to the sudden change in current, the current in the inductor will start to fall. A back EMF is produced across the inductor, inducing a voltage in the opposite direction, to try to keep the current flow. Again, as in boost mode, the DEAD state is repeated twice, when the switches are transitioned between on and off.

In the OFF interval, switch S1 is closed and switch S2 continues open. The current flows through the channel of the MOSFET S1 towards the inductor L1 and the load. The inductor continues releasing its energy stored to the load. Once the inductor has released half of its stored energy to the load and the capacitor, the voltage in the load begins to drop and the stored energy in capacitor C1 begins to be released. Then, the current keeps flowing through the load until the ON period starts again.

Figure 3.12 shows the ideal waveforms of a bidirectional buck-boost converter or also known as synchronous buck converter operating in CCM in boost mode. The plot shows the signals during a period T, including the ON time and OFF time. As it can be seen in Figure 3.12, DEAD time (T_{dead}) intervals are included to avoid accidental turning on of both switches S1 and S2. Therefore, this state applies when both switches are transitioning from one state (ON) to the other (OFF). When developing a final prototype this has to be taken into consideration. However, for the simulations the dead time will not be considered.

The parameters shown in Figure 3.12 are as follows:

- V_{GS1} and V_{GS2}: Gate control signal of the MOSFET's S1 and S2. When V_{GS1} is on, V_{GS2} is zero and vice versa;
- i_L: Current of the inductor;
- v_L: Voltage of the inductor;
- i_{S1} and i_{S2}: Current of the switches S1 and S2 respectively;
- V_{DS1} and V_{DS2}: Voltage of the internal diodes of the switches S1 and S2 respectively;
- i_C: Current of the capacitor;
- v_2: Output voltage or voltage at the load.

51
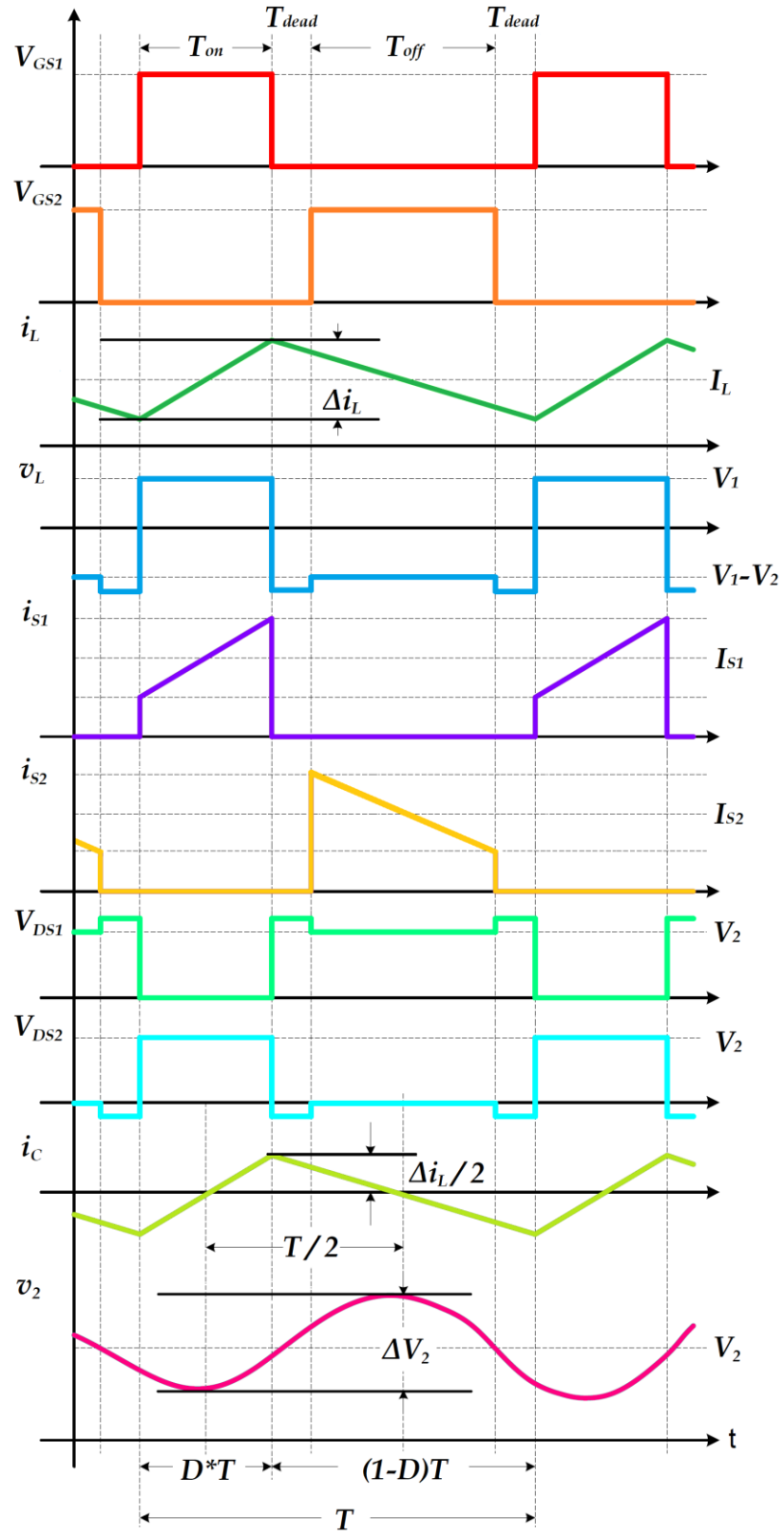
Figure 3.12. Waveforms of the bidirectional buck-boost converter operating under boost mode in steady state [146].

3.4 Design of Bidirectional DC/DC Converter

The following section provides detailed descriptions on the components design of the proposed bidirectional buck-boost converter that guarantee operation in any mode of operation. However, before going into details, the following assumptions will be considered during the analysis:

- All the components are considered ideal; ON period forward voltage drops and equivalent series resistance (ESR) of the components are neglected.
- The selection of the inductor (L_1) is such that the converter always operates in continuous conduction mode (CCM).
- The output voltage ripple is negligible.
- In steady state operation, both the integral of Volts-sec through an inductor, as well as the integral of Amp-sec through a capacitor, during one cycle will be equal to zero.

Figure 3.13 depicts the framework of the bidirectional buck-boost DC-DC converter proposed for the snow removal and charging application.
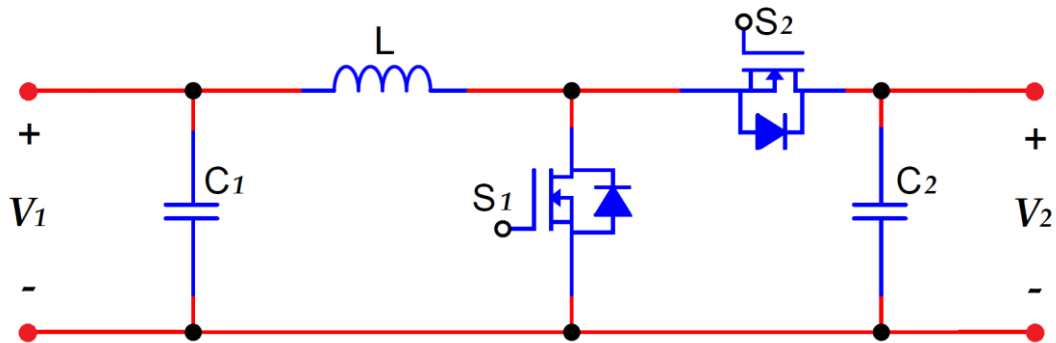
Figure 3.13. Framework of the bidirectional buck-boost DC-DC converter.

The following parameters are required to calculate the components of the proposed converter:

- PV panel string peak power: 2.2 kW

- PV panel voltage range: 225 to 320 VDC (considering 17% of losses due to heating of the solar panels at 65 °C and change in the irradiance)

- Nominal battery voltage range: 320 to 400 VDC

- Maximum output current: 5.5 A

Using the equations given by [147], [148] when the DC-DC converter works in the boost CCM the components can be designed as follows:

Duty cycle for minimum input voltage, where the efficiency estimated of the converter is 95%:

$$D = 1 - \frac{V_{1(min)}\eta}{V_2} = 1 - \frac{225 \, x \, 0.95}{400} = 0.4656 \tag{3.3}$$

Inductor ripple current estimation, considering the inductor ripple current as 20% of output current

$$\Delta I_L = \frac{(0.2 I_{2(Max)})V_2}{V_1} = \frac{(0.2 \, x \, 5.5)400}{225} A = 1.955 \, A \tag{3.4}$$

Then, the inductor calculation will be as follows, assuming a frequency of 30 kHz:

$$L = \frac{V_1(V_2 - V_1)}{\Delta I_L f_s V_2} = \frac{225(400 - 225)}{1.955 \, x \, 30x10^3 \, x \, 400} H = 1677.91 \, \mu H \tag{3.5}$$

A higher inductance was selected to keep the current ripple in the range. The value selected is $2100 \, \mu H$.

Then, the minimum output capacitance estimating an output voltage variation of 1% was calculated:

$$C_2 = \frac{I_{2(Max)}D}{\Delta V_2 f_s} = \frac{5.5 \, x \, 0.4656}{(0.01 \, x \, 400) \, (30x10^3)} F = 21.34 \, \mu F \tag{3.6}$$

A higher capacitance was selected to keep the voltage ripple in the range. The value selected is $27 \, \mu F$.

Using the equations given by [147], [149], when the DC-DC converter works in the Buck CCM, the maximum duty cycle with an estimated efficiency of 95% can be expressed as:

$$D = \frac{V_1}{V_2\eta} = \frac{320}{400 \ x \ 0.95} = 0.8421 \tag{3.7}$$

Then, the minimum input capacitance estimating an input voltage variation of 1%, in the buck CCM is calculated:

$$C_1 = \frac{V_2 D(1 - D)}{8f_s{}^2 L\Delta V_1} = \frac{400 \ x \ 0.8421(1 - 0.8421)}{8(30x10^3)^2(2.1x10^{-3})(0.01 \ x \ 225)} F = 1.56 \ \mu F \tag{3.8}$$

A higher capacitance was selected to keep the voltage ripple in the range. The value selected is $2 \ \mu F$. A summary with the parameter values is shown in Table 3.3.

Table 3.3. Parameters of the system.

Parameter	Value
Input Voltage Range ($V_{1Min} - V_{1Max}$)	225 – 320 V
PV Voltage at MPP (V_1)	271.8 V
Output Voltage (V_2)	400 V
Maximum Input Current ($I_{1(Max)}$)	8.13 A
Maximum Output Current ($I_{2(Max)}$)	5.5 A
Power Rating	2.2 kW
Efficiency (η)	95%
Inductance (L)	2100 μH
Output Capacitance (C_2)	27 μF
Input Capacitance (C_1)	2 μF
Switching Frequency (f_s)	30 kHz
Output and Input Voltage Variation	1%

3.5 Mathematical Modelling

The following section provides in-depth descriptions regarding the mathematical modelling of the proposed bidirectional buck-boost converter operating under boost and buck mode.

3.5.1 *Buck Operation Mode*

In this mode of operation, the converter is regulating the solar PV array (input port). It is assumed that an additional converter as the one shown in Figure 3.7, is regulating the voltage of the EV battery pack and at the same time supplying the required power to be transferred to the solar PV array in order to heat the PV cells. Figure 3.14 depicts the converter circuit operating in buck mode, where the solar PV array is represented by a load R_{PV} and the dc bus/EV battery pack is represented by a voltage source V_{bus}. Capacitance

C2 is not included in the circuit because it has no dynamic effect when the output port has a regulated voltage. The mathematical modelling was found by using the methodology applied by Dr. Ramos-Paja in [78], [150].
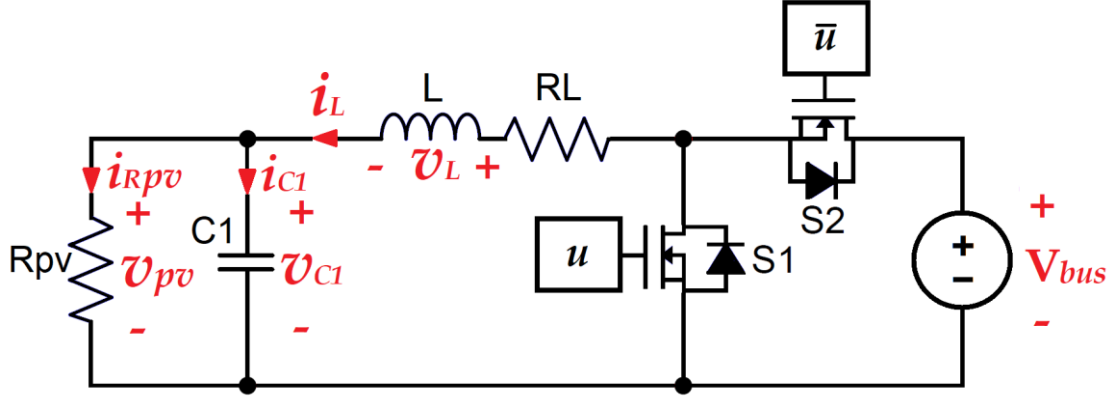
Figure 3.14. Circuit diagram of the bidirectional buck-boost DC-DC converter operating in buck mode.

Applying the state-space averaging method, the following model is obtained:

$$L\frac{di_L(t)}{dt} = v_{bus}(1-D) - i_L\alpha - v_{C1}\beta \qquad (3.9)$$

$$C_1\frac{dv_{C1}(t)}{dt} = i_L R_{PV}\gamma - v_{C1}\gamma \qquad (3.10)$$

Where:

$$\alpha = R_L + \frac{R_{PV}R_{C1}}{R_{PV} + R_{C1}}; \; \beta = 1 - \frac{R_{C1}}{R_{PV} + R_{C1}} \; ; \gamma = \frac{1}{R_{PV} + R_{C1}} \qquad (3.11)$$

This average system can be used to obtain the equilibrium points in steady state. To obtain the steady state currents and voltages, the left-hand side on equations (3.9) and (3.10) must be replaced with zero:

$$0 = V_{bus}(1-D) - I_L\alpha - V_{C1}\beta \qquad (3.12)$$

$$0 = I_L R_{PV}\gamma - V_{C1}\gamma \qquad (3.13)$$

Since the current through the capacitor C1 is equal to zero, in steady state I_L is equal to:

$$I_L = I_{PV} \qquad (3.14)$$

Replacing equation (3.14) into equation (3.13), V_{C1} will be found:

$$V_{C1} = I_{PV}R_{PV} \tag{3.15}$$

Replacing equations (3.14) and (3.15) into (3.12), D can be expressed as follows:

$$D = 1 - I_{PV}\left(\frac{R_{PV} + R_L}{V_{bus}}\right) \tag{3.16}$$

Applying the averaging small-signal dynamic modelling, the following linearized converter model is obtained, where the capital letters indicates the DC values (steady-state), and the superscript symbol (~) denotes the small AC perturbations of the variables of (3.9) and (3.10) around the equilibrium points [151], [152]:

$$L\frac{\tilde{di}_L(t)}{dt} = \underbrace{V_{bus}(1-D) - I_L\alpha - V_{C1}\beta}_{Equilibrium\ point} + \underbrace{\tilde{v}_{bus}(1-D) - \tilde{i}_L\alpha - \tilde{v}_{C1}\beta - \tilde{d}v_{bus}}_{Linear} \tag{3.17}$$
$$- \underbrace{\tilde{v}_{bus}\tilde{d}}_{Non-linear}$$

$$C_1\frac{dv_{C1}(t)}{dt} = \underbrace{I_LR_{PV}\gamma - V_{C1}\gamma}_{Equilibrium\ point} + \underbrace{\tilde{i}_LR_{PV}\gamma - \tilde{v}_{C1}\gamma}_{Linear} \tag{3.18}$$

In the above equations, it can be identified three components of the model: the equilibrium point which contain the DC terms; the linear dynamic component which include the first order AC terms; and the non-linear dynamic component which include second order AC terms [151].

By applying the Laplace transform to the linear part of equations (3.17) and (3.18) it is obtained the following equation:

$$\begin{cases} Ls\,I_L(s) = (1-D)V_{bus}(s) - \alpha I_L(s) - \beta V_{C1}(s) - V_{bus}D(s) \\ \quad . \\ C_1sV_{C1}(s) = R_{PV}\gamma I_L(s) - \gamma V_{C1}(s) \end{cases} \tag{3.19}$$

By modeling the dynamic behavior of the system, the following equations are obtained:

$$I_L(s) = \frac{\dfrac{-V_{bus}(C_1s + \gamma)}{LC_1}D(s) + \dfrac{(1-D)(C_1s + \gamma)}{LC_1}V_{bus}(s)}{s^2 + \dfrac{(L\gamma + C_1\alpha)}{LC_1}s + \dfrac{R_{PV}\gamma\beta}{LC_1}} \tag{3.20}$$

57

$$V_{C1}(s) = \frac{\dfrac{-V_{bus}R_{PV}\gamma}{LC_1}D(s) + \dfrac{R_{PV}\gamma(1-D)}{LC_1}V_{bus}(s)}{s^2 + \dfrac{(L\gamma + C_1\alpha)}{LC_1}s + \dfrac{R_{PV}\gamma\beta}{LC_1}} \qquad (3.21)$$

Omitting the disturbances in (3.20) and (3.21) the following transfer functions are obtained for the dynamic variables of the converter in relation to the duty cycle:

$$G_{id}(s) = \frac{I_L(s)}{D(s)} = \frac{\dfrac{-V_{bus}(C_1s + \gamma)}{LC_1}}{s^2 + \dfrac{(L\gamma + C_1\alpha)}{LC_1}s + \dfrac{R_{PV}\gamma\beta}{LC_1}} \qquad (3.22)$$

$$G_{vd}(s) = \frac{V_{C1}(s)}{D(s)} = \frac{\dfrac{-V_{bus}R_{PV}\gamma}{LC_1}}{s^2 + \dfrac{(L\gamma + C_1\alpha)}{LC_1}s + \dfrac{R_{PV}\gamma\beta}{LC_1}} \qquad (3.23)$$

As it can be noted in equation (3.22) $G_{id} = I_L(s)/D(s)$ has a negative sign and the transfer function shows a non-minimum phase nature, produced by a zero located in the right-half-plane. The control objective in this mode of operation is to enforce $i_L = I_{LRef}$. Therefore, to accomplish this, the proposed controller must have a negative sign. The controller C_{iL} selected is a PI compensator with a single negative feedback loop structure. By replacing all the values in the equilibrium point, the transfer function of G_{id} is obtained as follows:

$$G_{id}(s) = \frac{-1.905x10^5 s - 2.846x10^9}{s^2 + 1.529x10^4 s + 2.428x10^8} \qquad (3.24)$$

The open loop step response of G_{id} transfer function for a duty cycle perturbation from 0.6937 to 0.7437 is depicted in Figure 3.15. As it can be seen, the second order transfer function has an underdamped response with a settling time of 0.48 ms. The response is stable and presents an overshoot of 32.27% with a negative peak of 15.5.
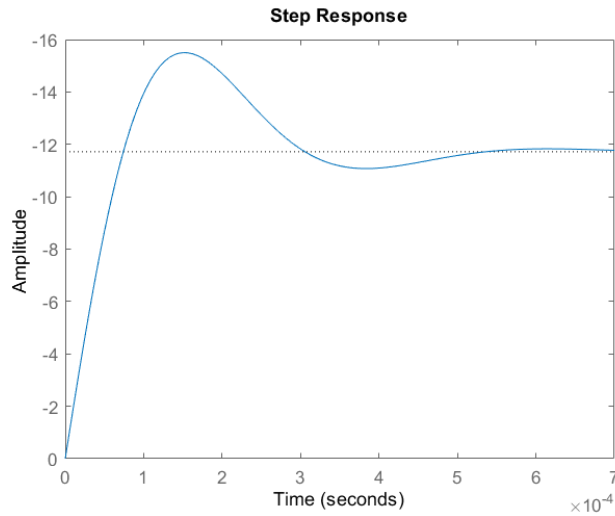
Figure 3.15. Open loop step response of $I_L(s)$ for a duty cycle perturbance of 0.05 (from 0.6937 to 0.7437).

Additionally, an AC analysis was performed using the AC sweep tool of PSIM. Both, the model and the circuit were analysed by injecting a small AC excitation signal as perturbation into the system input signal and the frequency responses of both were compared. The comparison of the frequency responses of the mathematical model and the circuital model for inductor current $I_L(s)$ and input capacitor voltage $V_{C1}(s)$ are shown in Figure 3.16.
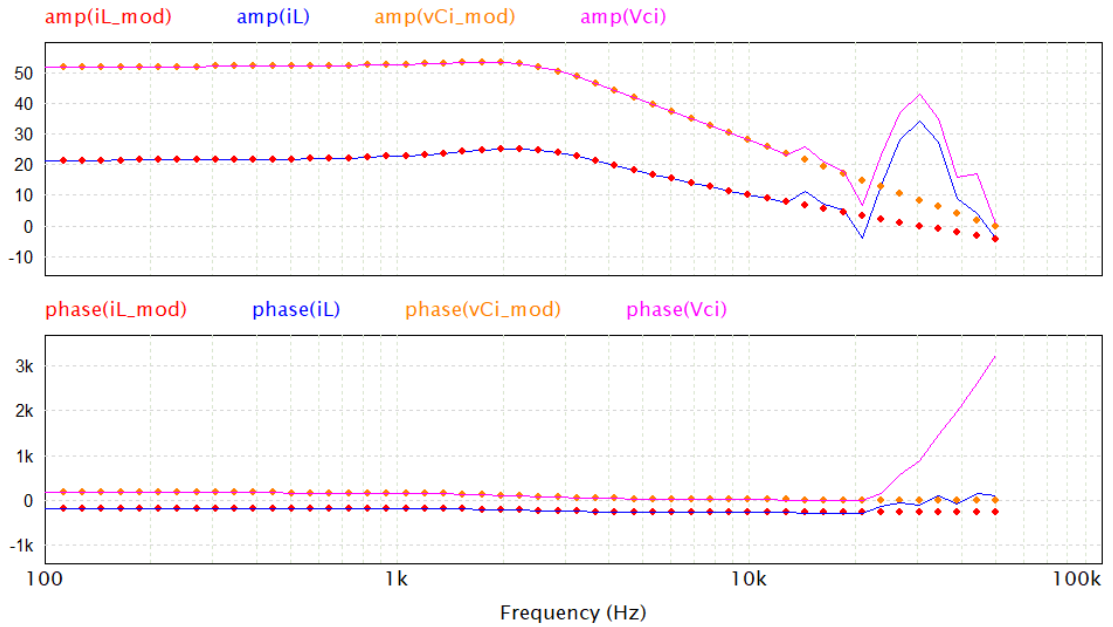
Figure 3.16. Comparison of the frequency responses of linear model and PSIM circuit in buck mode for inductor current $I_L(s)$ and input capacitor voltage $V_{C1}(s)$. Red and orange circles: mathematical model results. Blue and pink line: circuital simulation results.

59

The frequency responses of the circuital model simulated in PSIM compared with the analytical small-signal model exhibits a satisfactory agreement for i_L and V_{C1} variables up to 12kHz. According to these results it can be concluded that the adopted model accurately describes the system dynamics; therefore, it is suitable for control purposes.

Finally, the circuital model was simulated and evaluated at the equilibrium point. The duty cycle calculated for this mode was equal to 0.6937, according to equation (3.16). The circuit diagram is depicted in Figure 3.17 and its simulation results are shown in Figure 3.18. The simulation results satisfy the steady state calculations made before where the inductor current was regulated at 8.13 A and the PV voltage at MPP was 271.8 V.
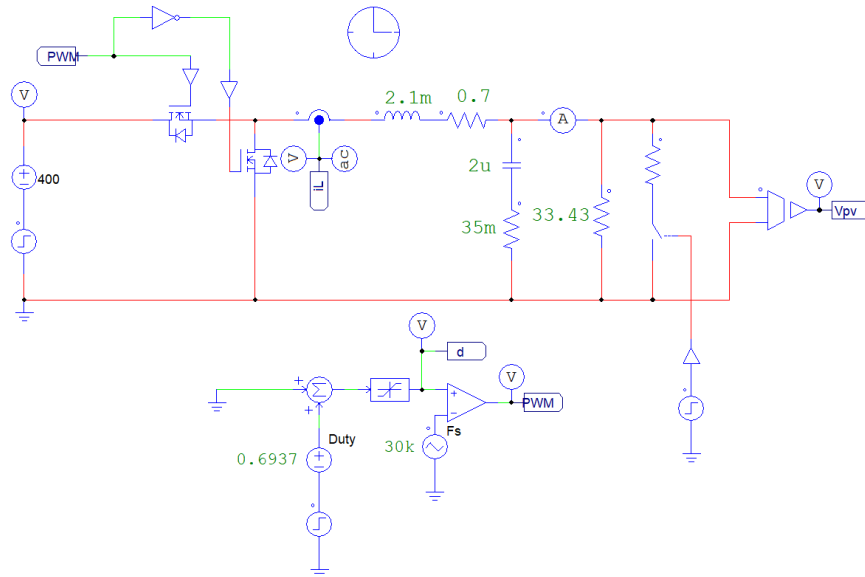
Figure 3.17. Circuit diagram operating in buck mode for open loop current control.
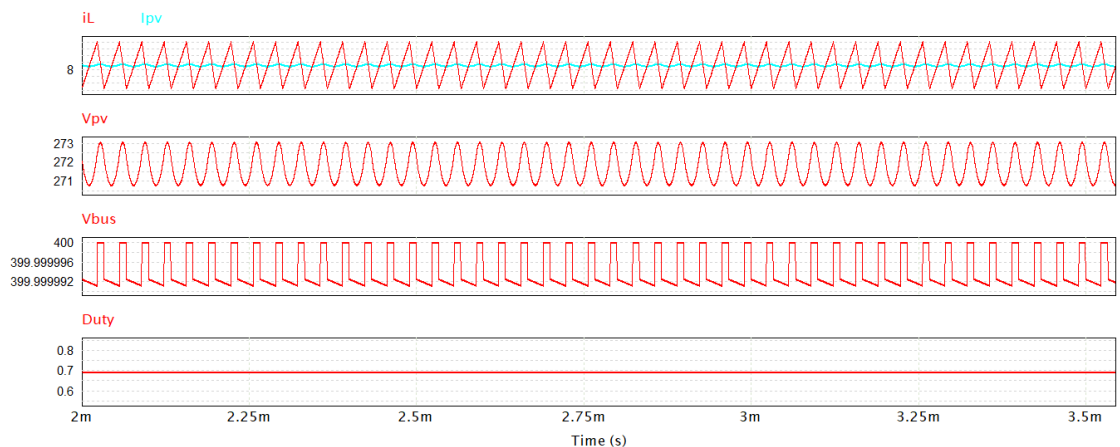
Figure 3.18. Simulation results of the circuit operating in buck mode for open loop current control.

60

3.5.2 *Boost Operation Mode*

In this mode of operation, the converter is fed by the solar PV array and has the function of regulating the maximum power point (MPP) provided by the solar PV array. Figure 3.19 depicts the converter equivalent circuit for the boost operation mode, where the EV battery pack connected at the dc bus is represented by a voltage source V_{bus} and the solar PV array is represented by the Norton equivalent model analyzed before. Again, capacitance C2 is not included for the same reason stated in the buck mode. The mathematical modelling was found by using the methodology applied by Dr. Ramos-Paja in [78], [150].
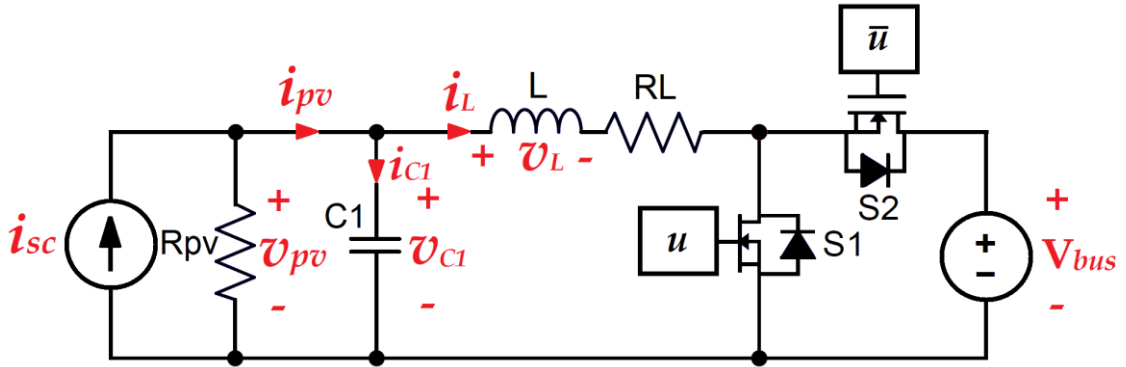
Figure 3.19. Circuit diagram of the bidirectional buck-boost DC-DC converter operating in boost mode.

Applying the state-space averaging method, the following model is obtained:

$$L\frac{di_L(t)}{dt} = -v_{bus}(1-D) - i_L\alpha + v_{C1}\beta + i_{sc}R_{PV}R_{C1}\gamma \tag{3.25}$$

$$C_1\frac{dv_{C1}(t)}{dt} = i_{c1} = -i_L R_{PV}\gamma - v_{C1}\gamma + i_{sc}R_{PV}\gamma \tag{3.26}$$

Where α, β *and* γ are as stated before in equation (3.11).

This average system can be used to obtain the equilibrium points in steady state. To obtain the steady state currents and voltages, the left-hand side on equations (3.25) and (3.26) must be replaced with zero:

$$0 = -V_{bus}(1-D) - I_L\alpha + V_{C1}\beta + I_{sc}R_{PV}R_{C1}\gamma \tag{3.27}$$

$$0 = -I_L R_{PV}\gamma - V_{C1}\gamma + I_{sc}R_{PV}\gamma \tag{3.28}$$

From the circuit it can be deduced that in steady state the inductor current I_L is equal to:

$$I_L = I_{PV} = I_{MPP} \tag{3.29}$$

Also, it can be deduced that the input capacitor voltage V_{C1} is equal to:

$$V_{C1} = V_{PV} = V_{MPP} \tag{3.30}$$

Replacing equations (3.29) and (3.30) into (3.28) and (3.27), D can be expressed as follows:

$$D = 1 - \frac{V_{MPP} - I_{MPP}R_L}{V_{bus}} \tag{3.31}$$

By replacing the parameters mentioned before ($V_{MPP} = 271.8$, $I_{MPP} = 8.13$) into equations (3.29) to (3.31), the following steady state operating point were obtained: $I_L = 8.13$, $V_{C1} = 271.8$ and D $= 0.3347$.

Applying the averaging small-signal dynamic modelling, the following linearized converter model is obtained, where the capital letters indicates the DC values (steady-state), and the superscript symbol (~) denotes the small AC perturbations of the variables of (3.32) and (3.33) around the equilibrium points [151], [152]:

$$L\frac{\widetilde{di_L}(t)}{dt} = -\underbrace{V_{bus}(1-D) - I_L\alpha + V_{C1}\beta + I_{sc}R_{PV}R_{C1}\gamma}_{Equilibrium\ point} +$$

$$\underbrace{-\tilde{v}_{bus}(1-D) - \tilde{\imath}_L\alpha + \tilde{v}_{C1}\beta + \tilde{\imath}_{sc}R_{PV}R_{C1}\gamma + \tilde{d}v_{bus}}_{Linear} + \underbrace{\tilde{v}_{bus}\tilde{d}}_{Non-linear} \tag{3.32}$$

$$C_1\frac{dv_{C1}(t)}{dt} = \underbrace{-I_LR_{PV}\gamma - V_{C1}\gamma + I_{sc}R_{PV}\gamma}_{Equilibrium\ point} - \underbrace{\tilde{\imath}_LR_{PV}\gamma - \tilde{v}_{C1}\gamma + \tilde{\imath}_{sc}R_{PV}\gamma}_{Linear} \tag{3.33}$$

By applying the Laplace transform to the linear part of equations (3.32) and (3.33) it is obtained the following equation:

$$\begin{cases} Ls\,I_L(s) = -(1-D)V_{bus}(s) - \alpha I_L(s) + \beta V_{C1}(s) + R_{PV}R_{C1}\gamma I_{sc}(s) \\ \qquad\qquad\qquad +V_{bus}D(s) \\ \\ C_1sV_{C1}(s) = -R_{PV}\gamma I_L(s) - \gamma V_{C1}(s) + R_{PV}\gamma I_{sc}(s) \end{cases} \tag{3.34}$$

The state space system is now characterized by the following vectors:

$$X = \begin{bmatrix} i_L \\ v_{C1} \end{bmatrix}; \quad U = \begin{bmatrix} d \\ i_{sc} \\ v_{bus} \end{bmatrix} \tag{3.35}$$

As well as, by the Jacobian matrices given as follows:

$$A_m = \begin{bmatrix} -\dfrac{\alpha}{L} & \dfrac{\beta}{L} \\ -\dfrac{R_{PV}\gamma}{C_1} & -\dfrac{\gamma}{C_1} \end{bmatrix}; \quad B_m = \begin{bmatrix} \dfrac{V_{bus}}{L} & \dfrac{R_{PV}R_{C1}\gamma}{L} & -\dfrac{1-D}{L} \\ 0 & 0 & \dfrac{R_{PV}\gamma}{C_1} \end{bmatrix} \tag{3.36}$$

The system output defined is the PV voltage V_{PV} which is expressed as follows:

$$V_{PV} = v_{C1} + i_{c1}R_{C1}\alpha \tag{3.37}$$

By replacing equation (3.26) into (3.37), matrices C_m and D_m where defined:

$$C_m = [-R_{PV}R_{C1}\gamma \quad \beta]; \quad D_m = [0 \quad 0 \quad R_{PV}R_{C1}\gamma] \tag{3.38}$$

To validate the proposed model, the transfer function between the duty cycle and the PV voltage $G_{vd}(s) = V_{pv}(s)/D(s)$ was calculated using MATLAB by replacing all the values in equilibrium point on the mathematical model found:

$$G_{vd}(s) = \frac{V_{pv}(s)}{D(s)} = \frac{-6666s - 9.523x10^{10}}{s^2 + 1362s + 2.384x10^8} \tag{3.39}$$

As it can be noted in equation (3.43), G_{vd} has the same characteristics as the transfer function found in the buck mode analysis. The control objective in this mode of operation is to enforce $v_{pv} = V_{pvRef}$. Therefore, to accomplish this, the proposed controller must have a negative sign. The controller C_{vpv} selected is a PI compensator with a single feedback loop structure.

Then, the open loop step response of the G_{vd} transfer function for a duty cycle perturbance from 0.3347 to 0.3847 is depicted in Figure 3.20. As can be seen, the transient response of the second order transfer function has an underdamped response with a high damping ratio which settles at 5.7 ms. Although, the response presents an overshoot of 87%, and then it stabilizes at -400 V.
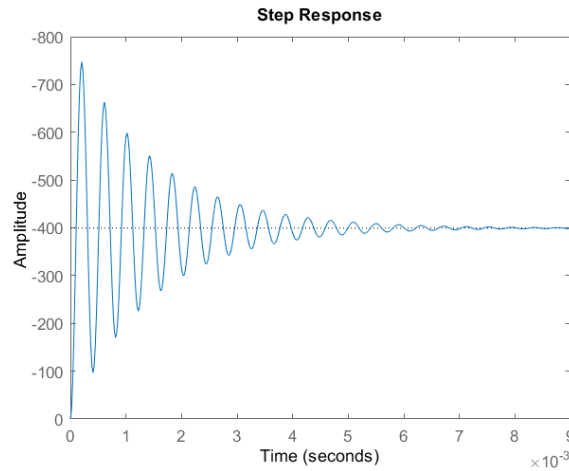
Figure 3.20. Open loop step response of $V_{pv}(s)$ for a duty cycle perturbance of 0.05 (from 0.3347 to 0.3847).

Furthermore, an AC analysis was performed using the AC sweep tool of PSIM as in the previous analysis for the buck mode. The comparison of the frequency responses of the mathematical model and the circuital model for solar PV array voltage $V_{pv}(s)$ are shown in Figure 3.21.
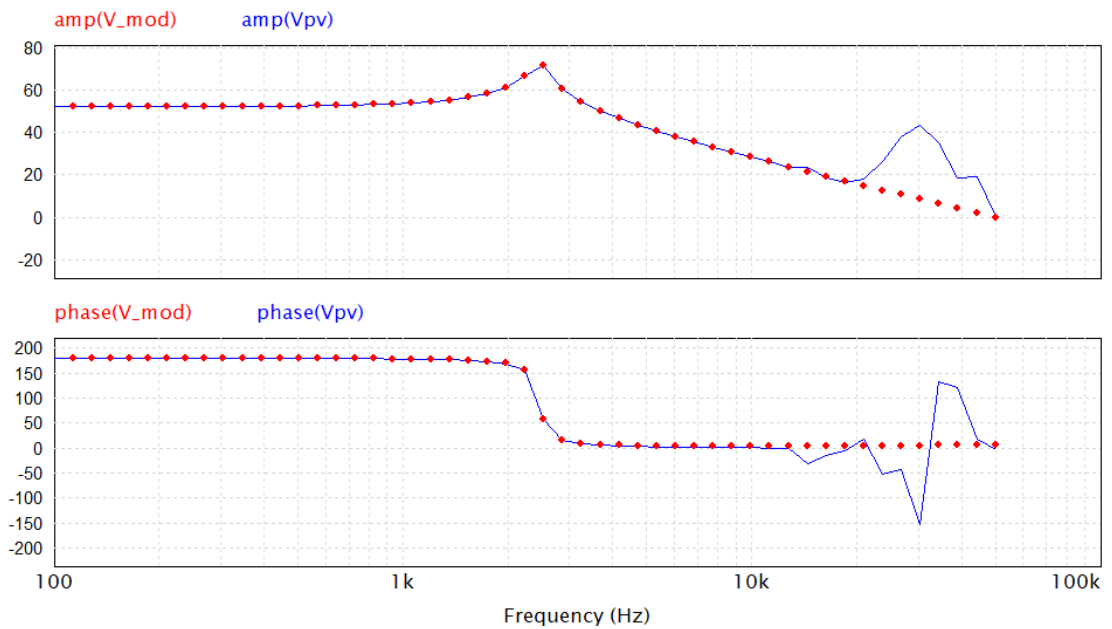
Figure 3.21. Comparison of the frequency responses of Norton model and PSIM circuit in boost mode for PV voltage V_{pv}. Red circles: mathematical model results. Blue line: circuital simulation results.

From the previous figure it can be concluded that the small-signal analytical model accurately describes the dynamics of the system operating in boost mode up to approximately 12 kHz for the variable V_{pv}; therefore, it is suitable for control purposes.

64

Finally, the circuital model for both, the non-linearized model and the linear model were simulated and evaluated at the equilibrium point. The duty cycle calculated for both models were equal to 0.3347 as mentioned before. The circuit diagram for the single-diode simplified model is depicted in Figure 3.22 and its simulation results are shown in Figure 3.23. On the other hand, the circuit diagram for the resistance linearized model (Norton Model) is depicted in Figure 3.24 and its simulation results are shown in Figure 3.25.
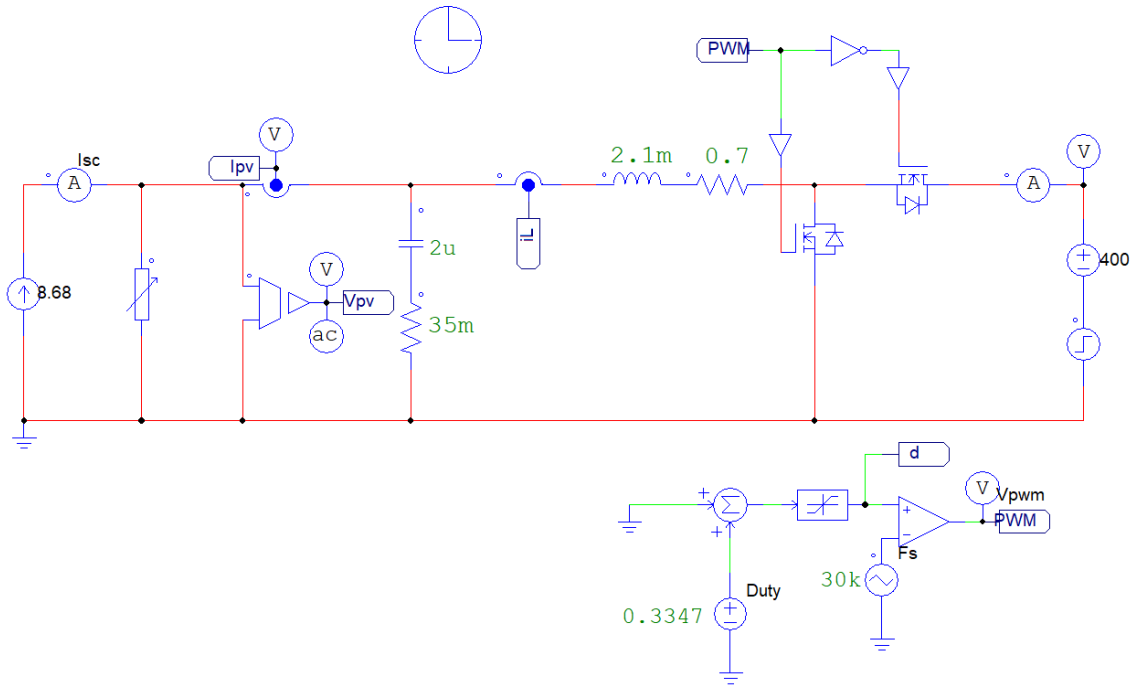
Figure 3.22. Circuit diagram of the non-linearized model operating in boost mode for open loop voltage control.
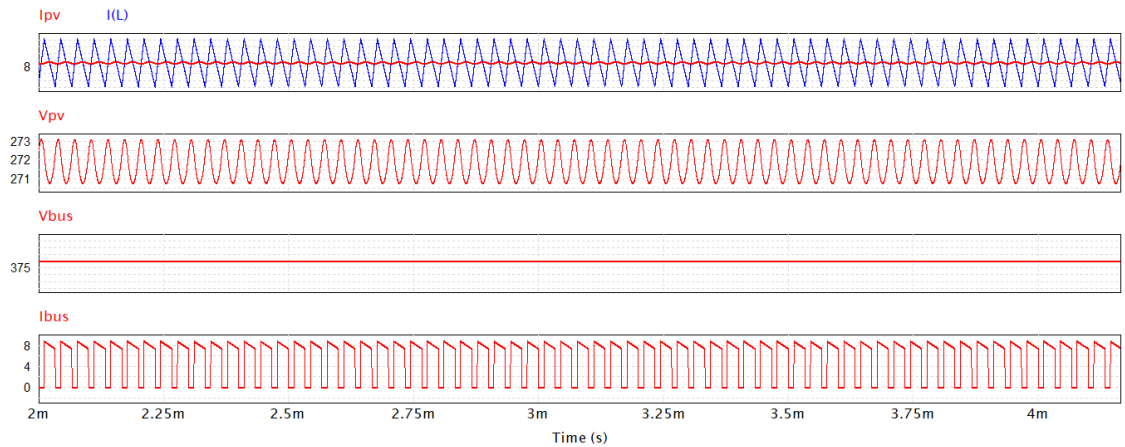
Figure 3.23. Simulation results for the non-linearized circuital model operating in boost mode for open loop voltage control.

65
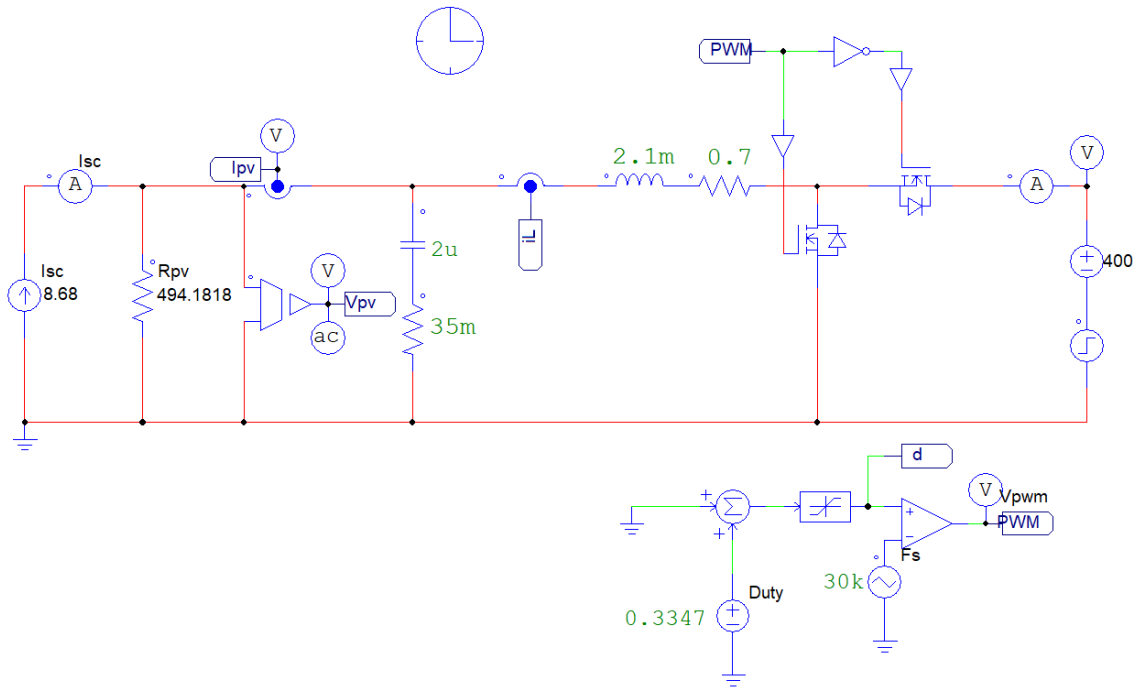
Figure 3.24. Circuit diagram of the linearized model operating in boost mode for open loop voltage control.
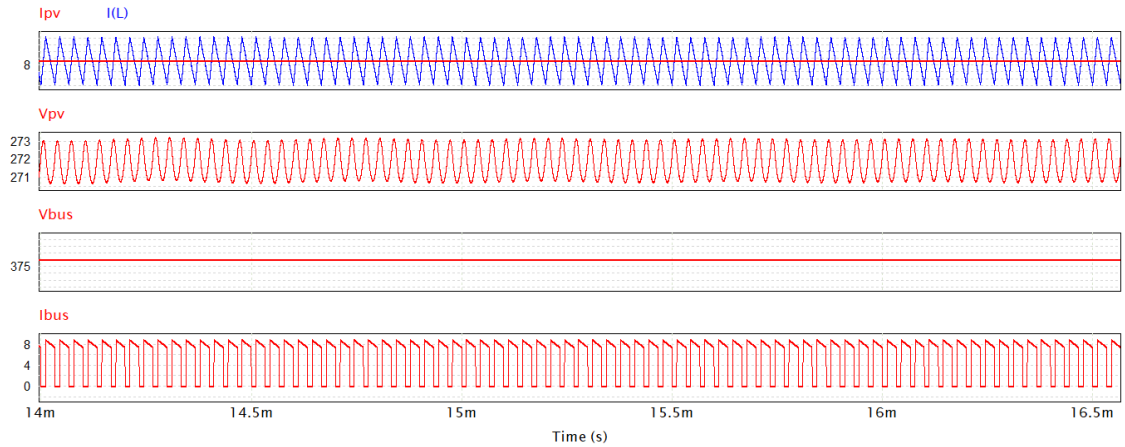
Figure 3.25. Simulation results for the linearized circuital model operating in boost mode for open loop voltage control.

As it can be noted, both models accurately satisfy the dynamics of the system. It can be seen in Figure 3.23 and Figure 3.25 that the inductor current was regulated at 8.13 A and the PV voltage was 271.8 V in both cases.

3.6 Control Design

In this section, the controller design will be explained in detail. The control technique used for the proposed converter topology is based on the pulse width modulation (PWM) by operating with a constant switching frequency [144]. A traditional proportional integral (PI) controller is designed for both modes of operation, i.e. boost mode and buck mode. However, for the buck operation mode, a current controller for inductor current $I_L(s)$ is designed, and for the boost operation mode, a voltage controller for PV voltage $V_{pv}(s)$ to optimize a perturb and observe (P&O) MPPT is designed [78], [87].

3.6.1 *Buck Operation Mode*

In this mode of operation, a PI current controller with a single negative feedback loop structure was designed to regulate the inductor current $I_L(s)$ by using a reference value defined. In this case, it is regulated to the rated current at the MPP of the solar PV array. The block diagram of the current controller is shown in Figure 3.26.
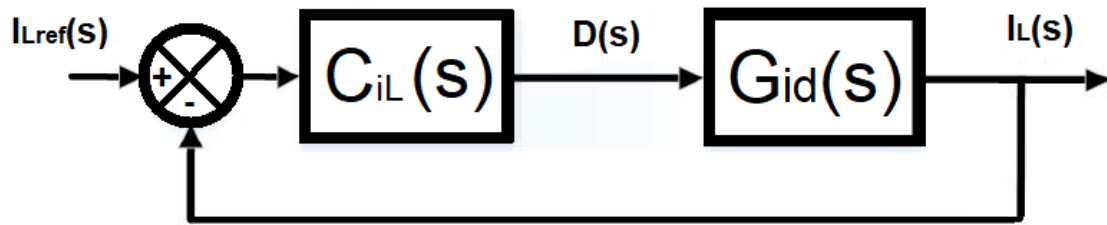
Figure 3.26. Block diagram of the current controller for the proposed converter operating in Buck mode.

The PI controller was tuned using the MATLAB SISO tool by adding a real zero and integrator to meet the desired dynamic behavior of the system. The PI controller was required to have a negative sign to compensate for the negative sign of the $G_{id}(s)$ transfer function. A damping ratio equal to or higher to 0.707 was defined, as well as a crossover frequency of 12 kHz with a gain margin of -3 dB according to the AC sweep results analyzed before and a settling time of less than 1 s. Satisfying the aforementioned design parameters as shown in Figure 3.27, the controller coefficients defined in equation (3.41) were obtained.
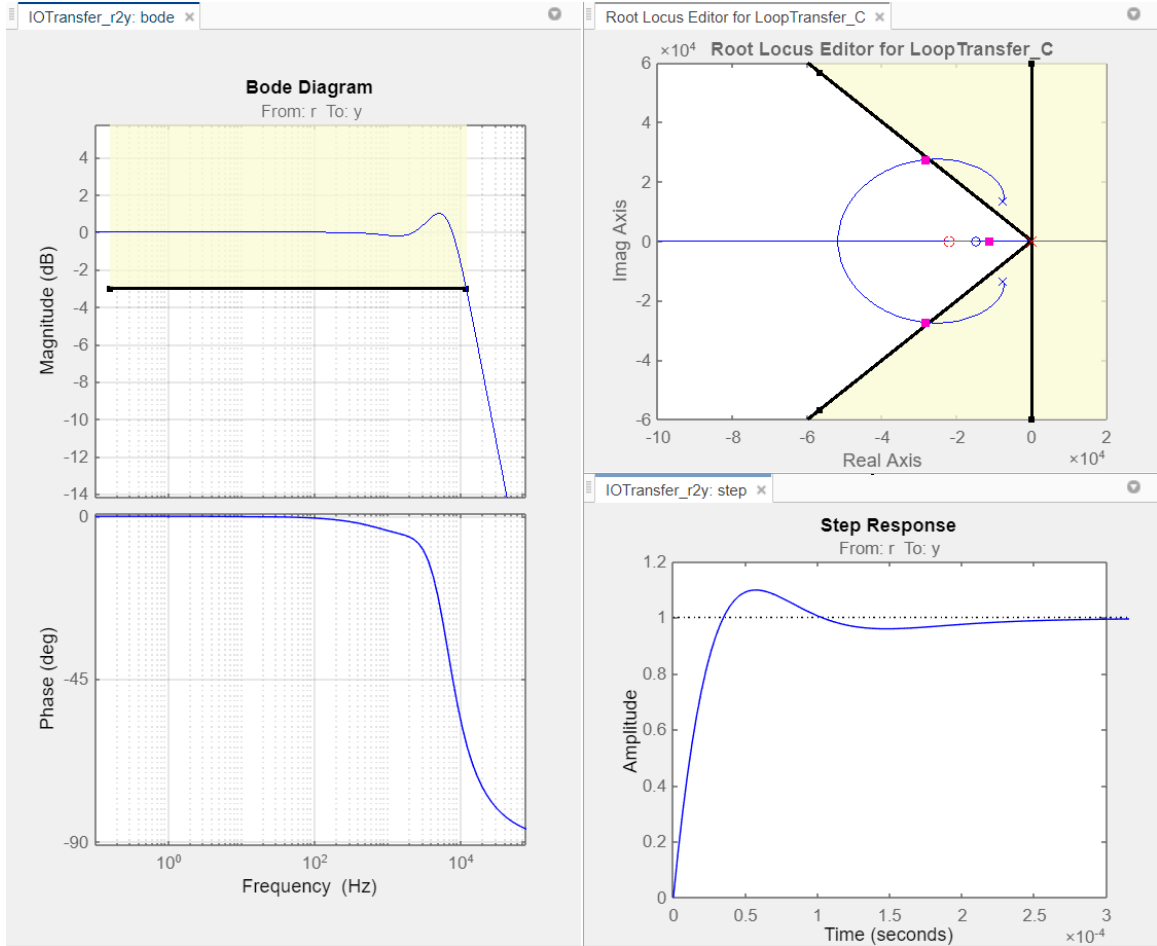
Figure 3.27. Tuning PI current controller for $I_L(s)$ using MATLAB SISO tool.

The equation of the compensator to control the current I_L is:

$$C_{iL} = K_p \left(1 + \frac{1}{T_i s} \right) \tag{3.40}$$

Where:

$$K_p = -0.2753 \; ; \; T_i = \; 4.5351 x 10^{-5} \tag{3.41}$$

3.6.2 *Boost Operation Mode*

In the boost operation mode, a PI voltage controller with a single negative feedback loop structure was designed to regulate the PV voltage $V_{PV}(s)$ using a reference value defined by a P&O MPPT [87]. Therefore, in the boost mode, the converter provides the maximum power to the load, keeping a constant voltage at the input. The block diagram of the voltage controller with MPPT is shown in Figure 3.28.

68
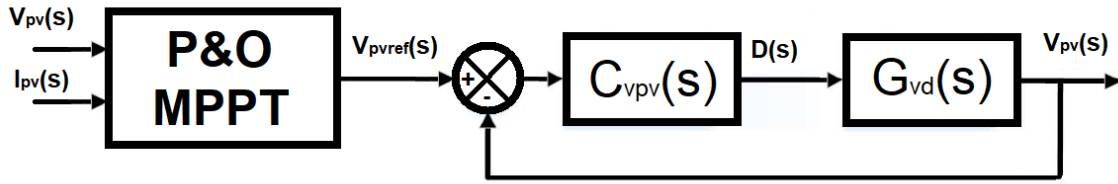
Figure 3.28. Block diagram of the voltage controller with MPPT for the proposed converter operating in Boost mode.

The PI controller was tuned using the MATLAB SISO tool by adding a real zero and integrator to meet the desired dynamic behavior of the system. The PI controller was required to have a negative sign to compensate for the negative sign of the $G_{vd}(s)$ transfer function. A damping ratio equal to or higher to 0.707 was defined, as well as a crossover frequency of 12 kHz at a magnitude of -3 dB according to the AC sweep results analyzed before and a settling time of less than 1 s. However, it was not possible to comply with the damping ratio design requirement, giving as a result a high underdamped response. Nevertheless, the other aforementioned design parameters were satisfied as shown in Figure 3.29, obtaining the controller coefficients defined in equation (3.43).
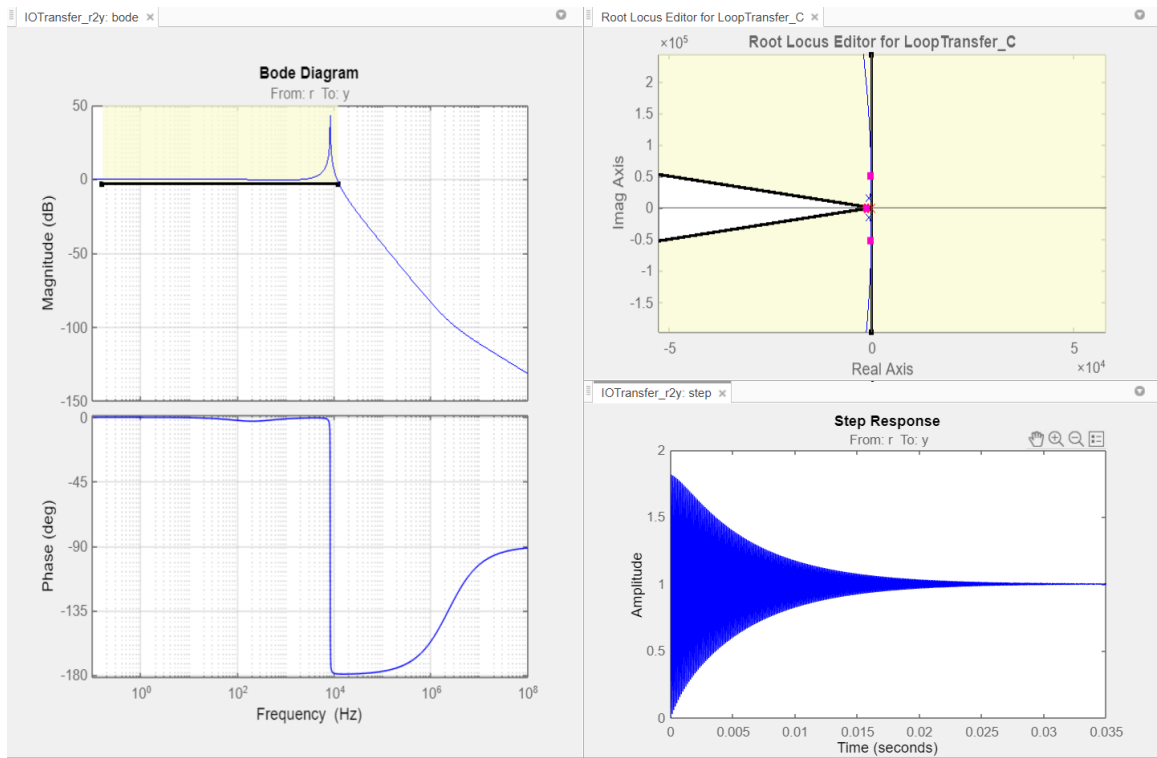
Figure 3.29. Tuning PI voltage controller for $V_{pv}(s)$ using MATLAB SISO tool.

69

The equation of the compensator to control the voltage V_{pv} is:

$$C_{vpv} = K_p \left(1 + \frac{1}{T_i s}\right)$$ (3.42)

Where:

$$K_p = -0.025015 \; ; \; T_i = 7.5758 x 10^{-4}$$ (3.43)

3.6.3 *Impact of Parasitics on the Controller*

As it is known all capacitors contain parasitic elements that can affect the performance of the circuit. A non-ideal capacitance is composed of an equivalent series resistance (ESR), and an effective series inductance (ESL). It is very important to ensure that the voltage ripple does not exceed the maximum rating of the capacitor as it can cause instability in the controller. This may be due to high internal ESR of the capacitor, which also causes excessive heating due to power dissipation.

On the other hand, to provide good high-frequency performance, it is necessary to bypass electrolytic capacitors by using film or ceramic capacitors, due to high ESL of the capacitor. Otherwise, ringing in the output voltage can be expected.

3.6.4 *Power Management*

A power management system will control the two separate buck and boost mode controllers through a power management command [153] as shown in Figure 3.30. A switch connected between both modes of operation will be operated according to the control algorithm flowchart shown in Figure 3.31.
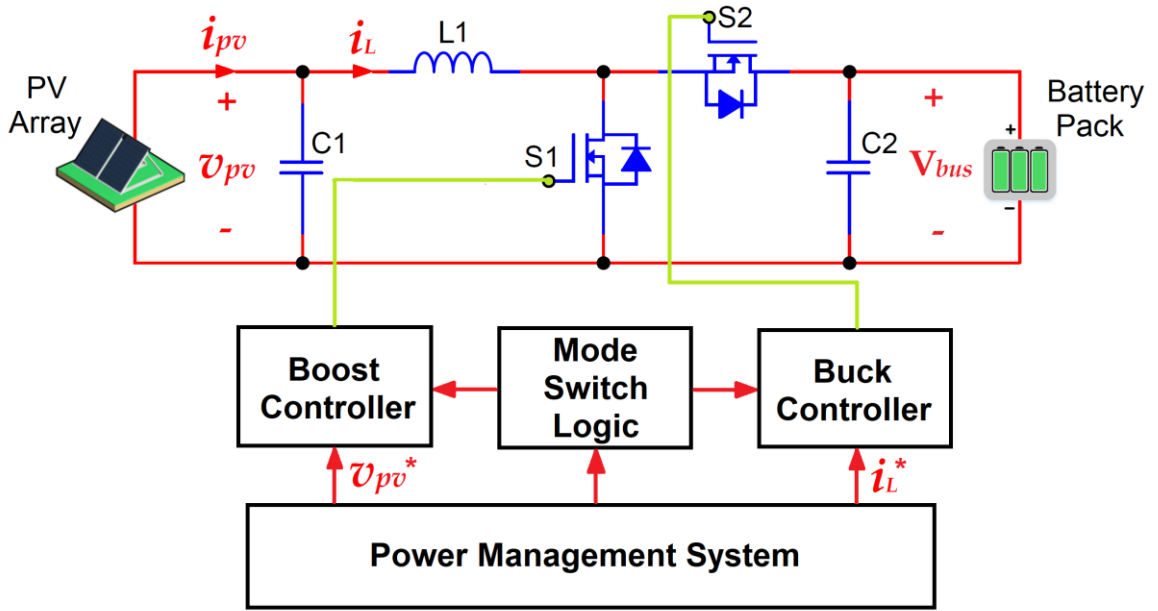
Figure 3.30. Circuit diagram of the power management control.

In the control algorithm flowchart, it can be noted that only when the EV battery pack is connected to the system and the power provided by the solar PV array is higher than 1000 W, then, the EV battery pack will be fed by the solar PV array (boost operation mode). Otherwise, a main storage or the grid will feed the solar PV array through a second bidirectional converter as shown before in Figure 3.6. However, when an EV battery pack is not connected to the system and the weather conditions meet the parameters (temperature below zero / snowing / freezing rain), then the buck mode will go into operation. If the weather conditions are not met, the solar PV array will feed the main battery or the grid, depending on the system configuration.
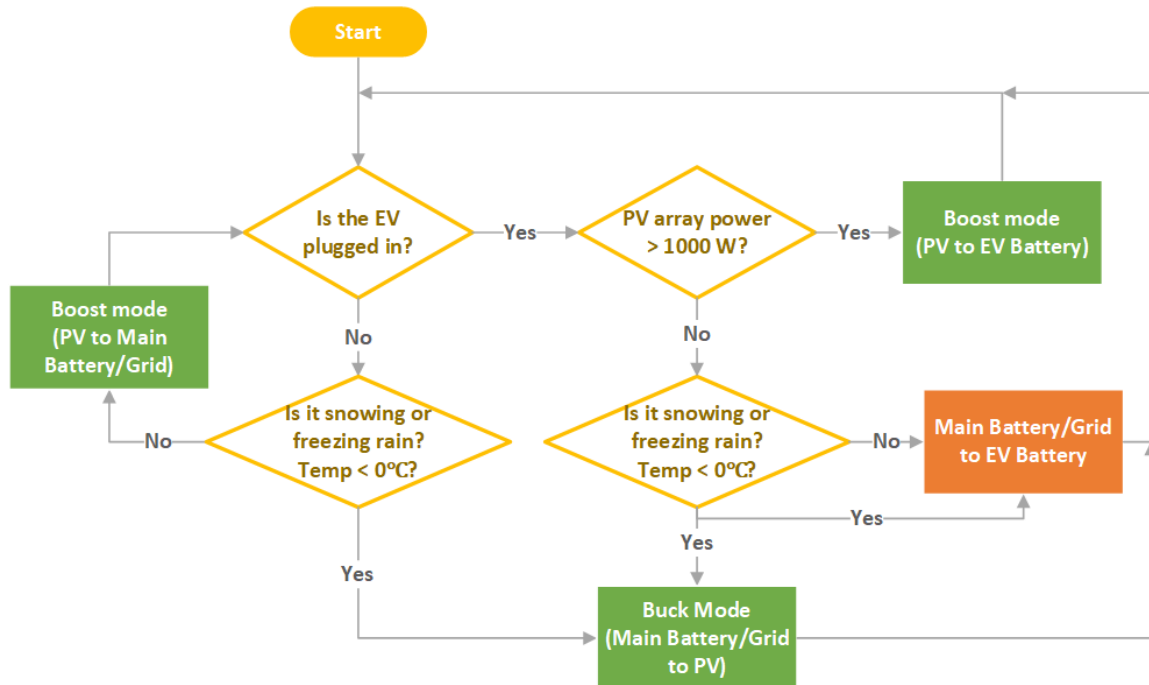
Figure 3.31. Control algorithm flowchart.

3.7 Simulation Results

This section shows the simulation results for the different operating modes of the proposed converter control.

3.7.1 Buck Operation Mode

The controller designed for the buck operation mode was simulated using the PSIM software. For control and simulation purposes the PV solar array was assumed as a load resistance. The circuit diagram is shown in Figure 3.32. The performance of the control was evaluated in terms of its capacity to reject perturbances in the inductor current reference, the bus voltage and the load.
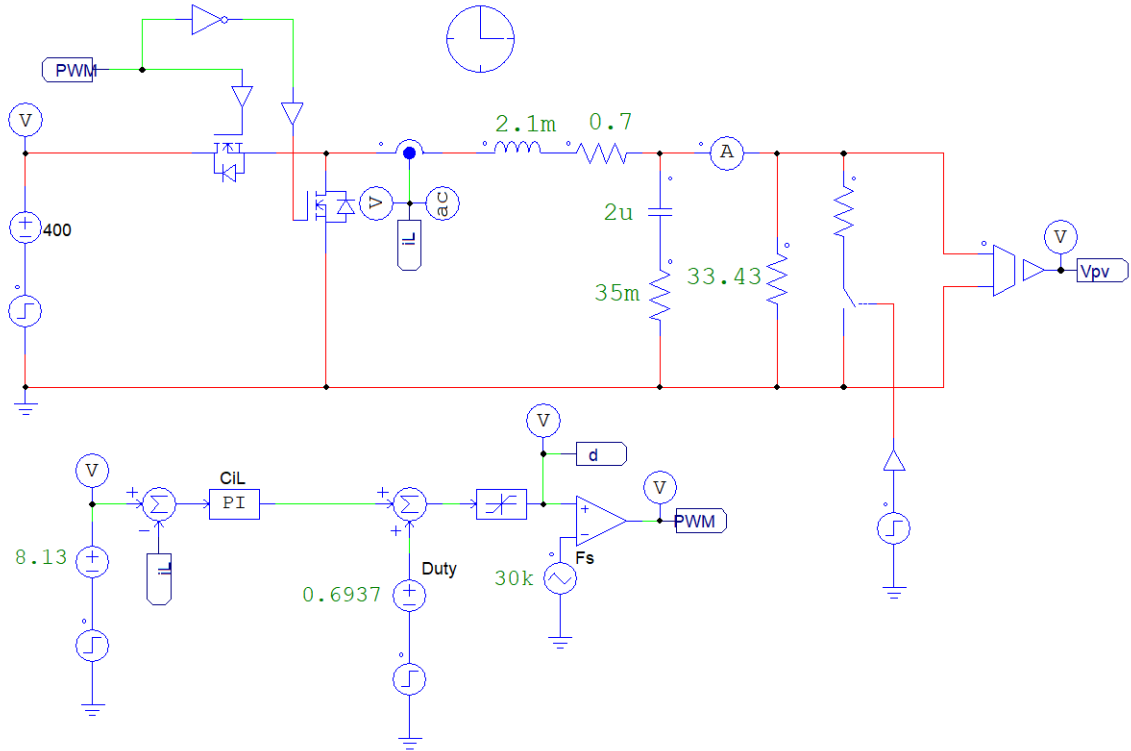
Figure 3.32. Circuit diagram for current controller for the proposed converter in buck mode.

The validation test applied in this mode of operation consisted of forcing the steady state of the converter by regulating the inductor current I_L and therefore the PV current I_{pv} to 8.13 A with a PV voltage V_{pv} of 271.8 V. Then, at 6ms a negative step was applied to the inductor current reference to validate the robustness of the system, changing from 8.13 to 7.13 A. After that, it was applied a disturbance in the bus voltage V_{bus}, where the EV battery pack is connected, at 10 ms setting a change of 5 V, from 400 to 405 V. Finally, a change on the load was set at 14 ms, decreasing the load from 33.43 Ω to 30.47 Ω.

Figure 3.33 shows the simulated waveforms for all the cases aforementioned. The first waveform shows the inductor current I_L, the solar PV array current I_{PV} and the control reference current I_{Lref}. The second waveform depicts the PV array voltage V_{PV}, while the third waveform shows the bus voltage V_{bus}. Finally, the last waveform shows the duty cycle applied to the controller.
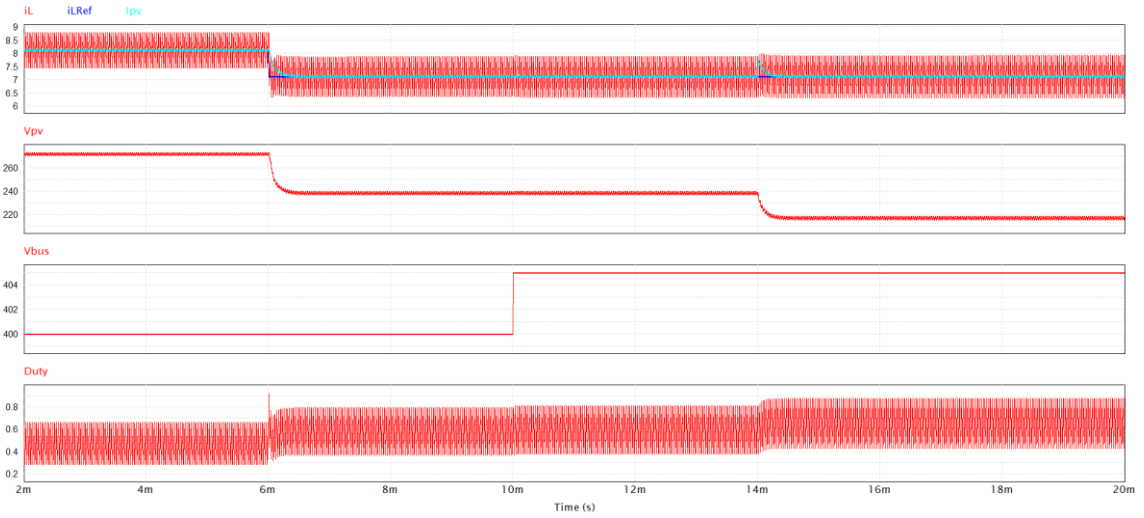
Figure 3.33. Performance analysis for different perturbances of the buck operating mode.

Figure 3.34 shows a close-up of the transient response for the different perturbations applied to the proposed converter. As can be seen, the proposed control accurately rejected all disturbances, showing a settling time below 0.1 ms with little noticeable deviation voltage. In all cases, the current was regulated uniformly to the set reference point which was 7.13 A, despite the applied disturbances.
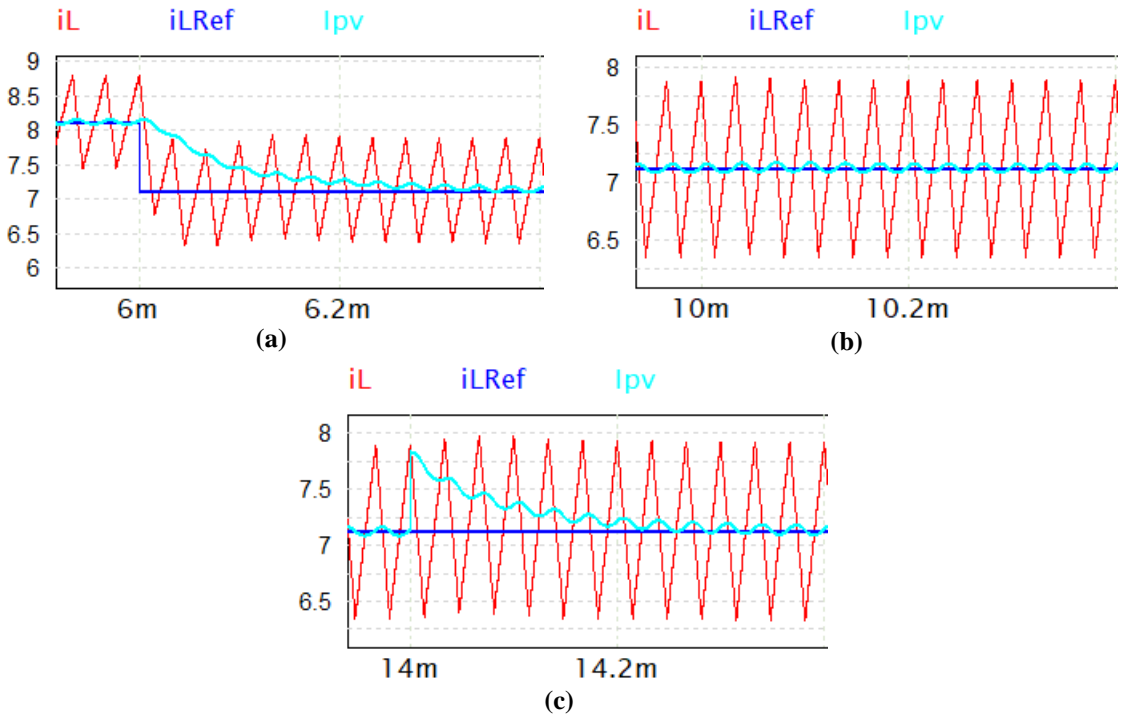
Figure 3.34. Zoom in of the simulated waveforms during validation test of the current controller for the proposed converter in buck mode. (a) Disturbance in inductor current reference; (b) Disturbance in the bus voltage; (c) Disturbance in the load.

74

3.7.2 Boost Operating Mode

In the boost operating mode, there were simulated two configurations using the PSIM software; first, the voltage controller applied to the proposed converter was simulated to observe the response of the system. Second, the P&O MPPT with the voltage controller applied to the proposed converter to validate the close-loop behaviour of the system under different irradiance conditions.

On the first case, the voltage controller designed to control the PV array voltage V_{pv} was simulated using the parameters calculated before. Figure 3.35 shows the circuit diagram of the DC-DC converter proposed with the voltage controller. In this case, the converter is simulated using the non-linear model (single-diode model).
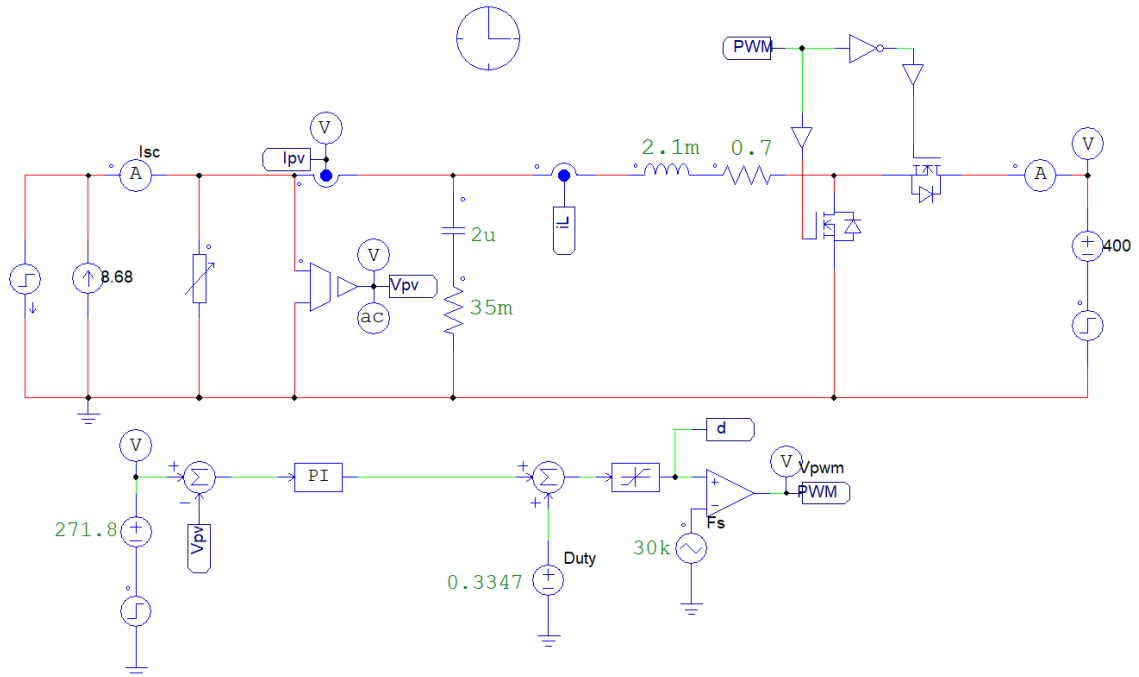
Figure 3.35. Circuit diagram for voltage controller applied to the non-linear model PV array for the proposed converter in boost mode.

To validate the response of the voltage controller in close-loop, the system was forced to operate at the equilibrium point using the steady state parameters. Therefore, from 2-6 ms, the proposed converter was operating on the steady state by setting a duty cycle of 0.3347 and a reference voltage of 271.8 V; then, a perturbance in the reference voltage was introduced by setting a negative step reducing the voltage to 270.8 V at 6 ms; after that a perturbance in the output voltage V_{bus} was set changing the output voltage from 400 to 405

V at 10 ms; finally, a negative step was introduced in the short-circuit current I_{sc} which simulate the change of irradiance in the non-linear model; the short-circuit current was reduced from 8.68 to 8.18A at 14 ms. The simulated waveforms are shown in Figure 3.36.
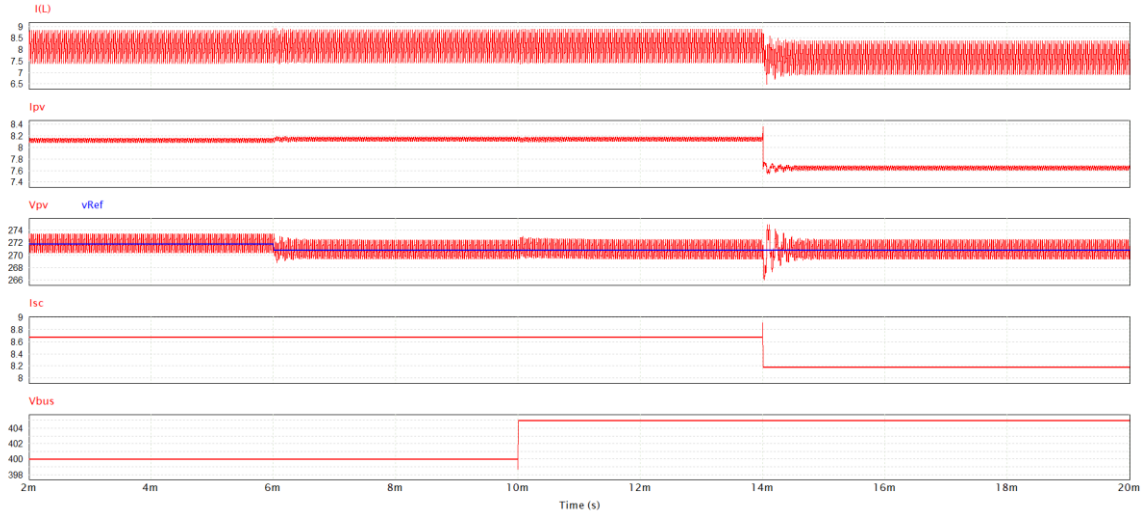
Figure 3.36. Simulated waveforms during validation test of the voltage controller for the proposed converter in boost mode.

In the above waveforms, the transient response is characterized by an underdamped ringing of the input voltage V_{PV} when there are sharp changes in irradiance as it can be seen at 14 ms. Due to this response, it is desirable that when the irradiance decreases to a certain point, in our case when the PV array produces less than half of the power produced at the MPP (1000 W), then, an energy storage system or grid must provide the required energy to charge the EV battery pack, as showed before in the control algorithm flowchart in Figure 3.31. In the other cases, when disturbances were applied in the voltage reference and in the output voltage, the control successfully rejected these disturbances with little noticeable voltage deviations as it can be seen in the third waveform for V_{PV} and V_{ref} in Figure 3.36.

Then, the P&O MPPT connected to the voltage controller was simulated. Figure 3.37 shows the circuit diagram for the final boost mode controller. For this simulation, it was used a PSIM PV model using the parameters given in Table 3.1. The behaviour of the system was evaluated by changing the irradiance conditions of the solar PV array, maintaining a constant temperature.
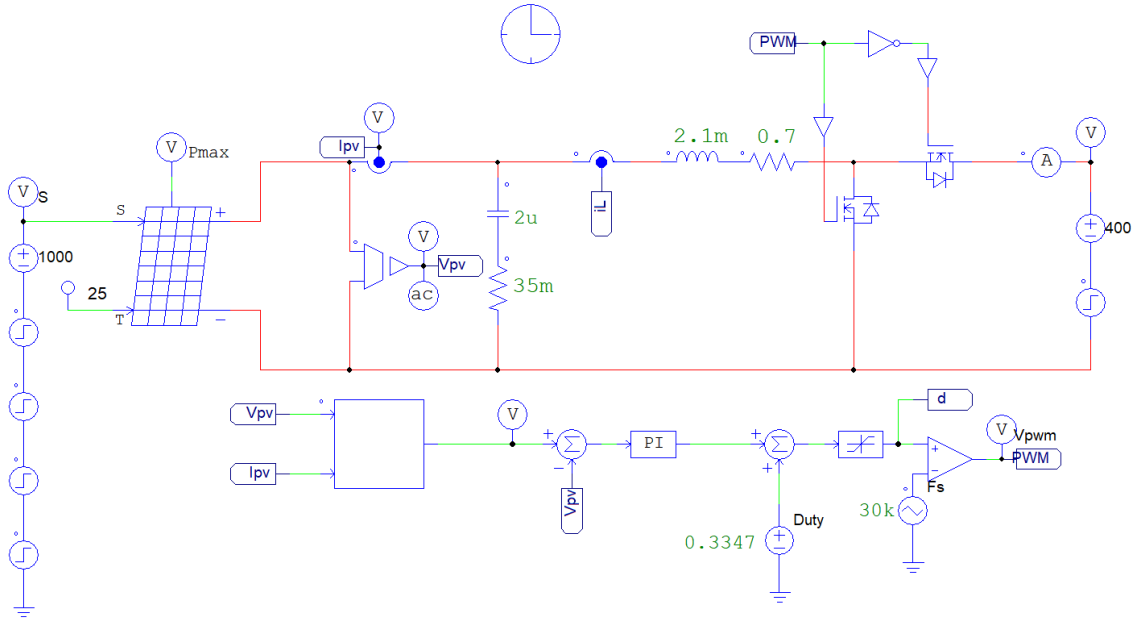
Figure 3.37. Circuit diagram for MPPT with voltage controller for proposed converter in boost mode.

The profile of irradiation used to validate the operation of the proposed converter in boost mode was set to force a steady state at the maximum power point of the converter, by starting with an irradiance of 1000 W/m^2 for time 2-6 ms; after that the irradiance was changed by introducing negative steps of 4 ms resulting the following values: 900 W/m^2 for time 6-10 ms, 800 W/m^2 for time 10-14 ms, 400 W/m^2 for time 14-18 ms and finally a positive step, resulting on a irradiance of 1000 W/m^2 for time 18-20 ms. Temperature is kept constant at 25 ºC throughout the simulation. The profile of irradiation is depicted in the S waveform shown in Figure 3.39.

Figure 3.38 shows the simulation results that validates the response of the proposed converter in steady state. The P&O MPPT developed is a digital control that looks for the MPP by changing the voltage reference every 0.35 ms. The control increases or decreases the voltage in steps of 250 mV depending on the measured power of the PV array and when the stable condition is reached the algorithm oscillates around the peak power point as it can be seen in the first waveform of the solar PV voltage (V_{pv}) and in the third waveform of the solar PV power ($V_{pv}*I_{pv}$) in Figure 3.38.

77
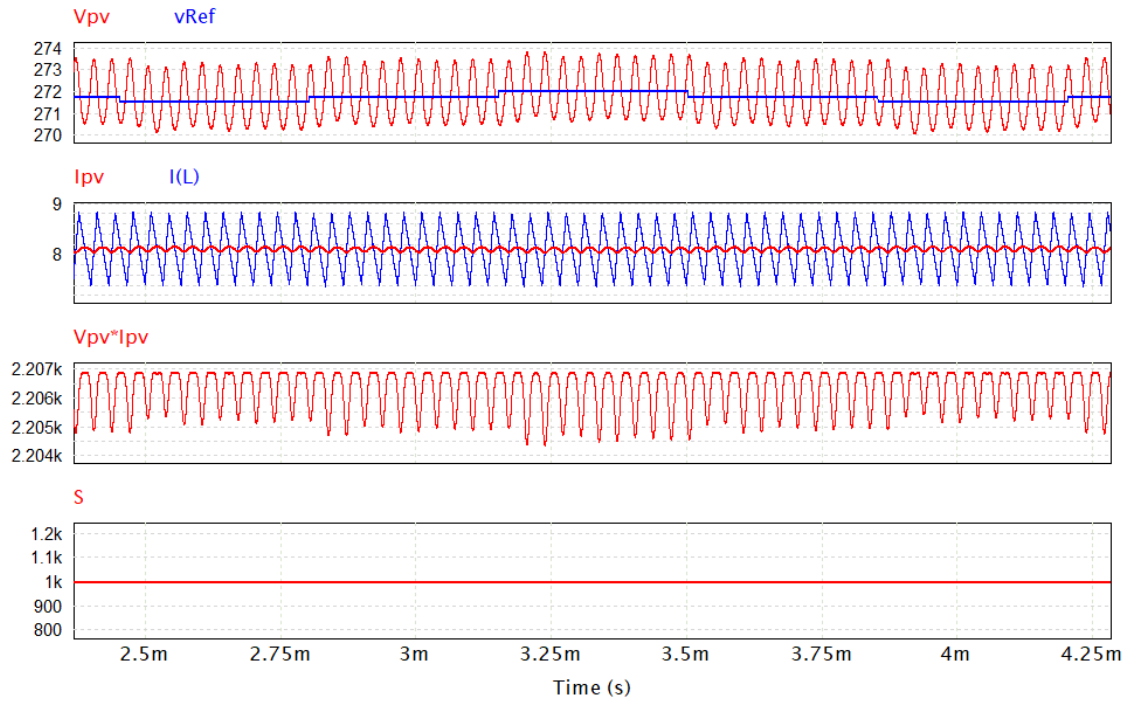
Figure 3.38. Simulated waveforms during validation test of the P&O MPPT with voltage controller for an irradiance of 1000 W/m² for the proposed converter in boost mode.
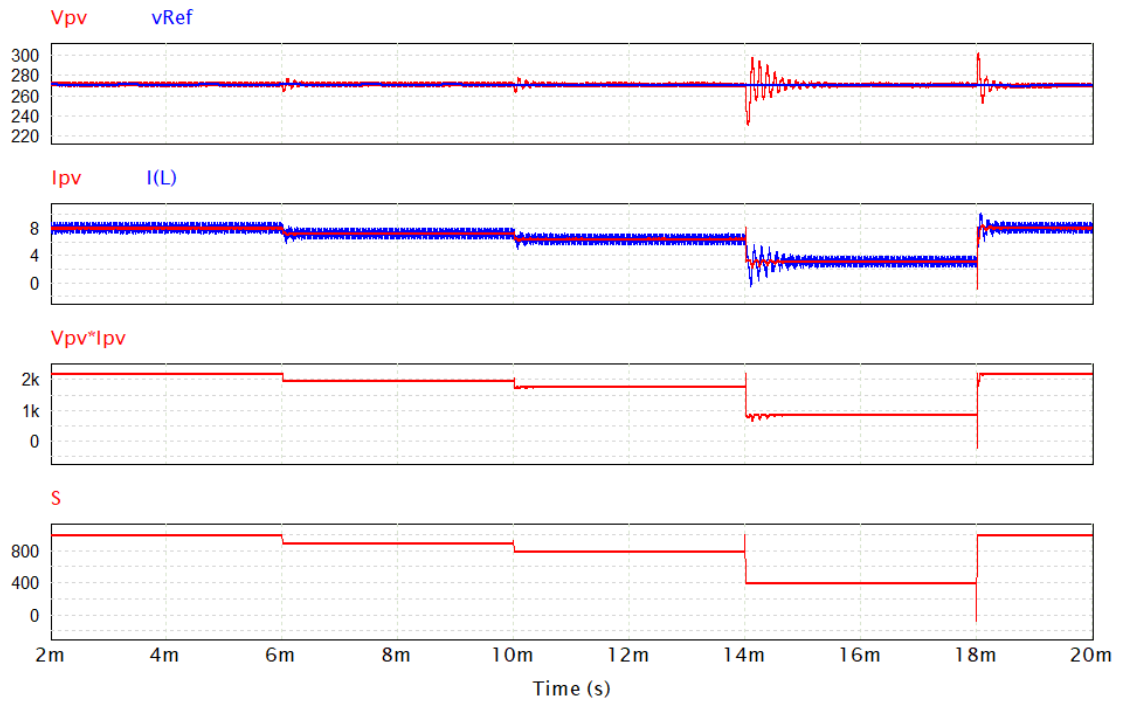
Figure 3.39. Simulated waveforms during validation test of the P&O MPPT with voltage controller for different irradiances for the proposed converter in boost mode.

78

Figure 3.40 shows a zoom in of the transient response simulation results for small changes in irradiance. The first set of waveforms shows the transient response for a negative step change of 100 W/m² (from 1000 to 900 W/m²) in the irradiance. The waveforms show a rejection of the perturbation with a voltage deviation below 6.58 V (2.42%) and a settling time of about 0.17 ms to recover to steady state. The second set of waveforms shows a similar transient response. It was applied again a negative step change of 100 W/m² (from 900 to 800 W/m²) in the irradiance. In this case, the waveforms show a rejection of the perturbance producing a voltage deviation below 6.94 V (2.55%) and a settling time of about 0.17 ms to recover to steady state. It can be noted that when the power of the PV array is close to the MPP, the control rejects the perturbances producing a smaller overshoot peak voltage than when the PV array power is getting away of the MPP.
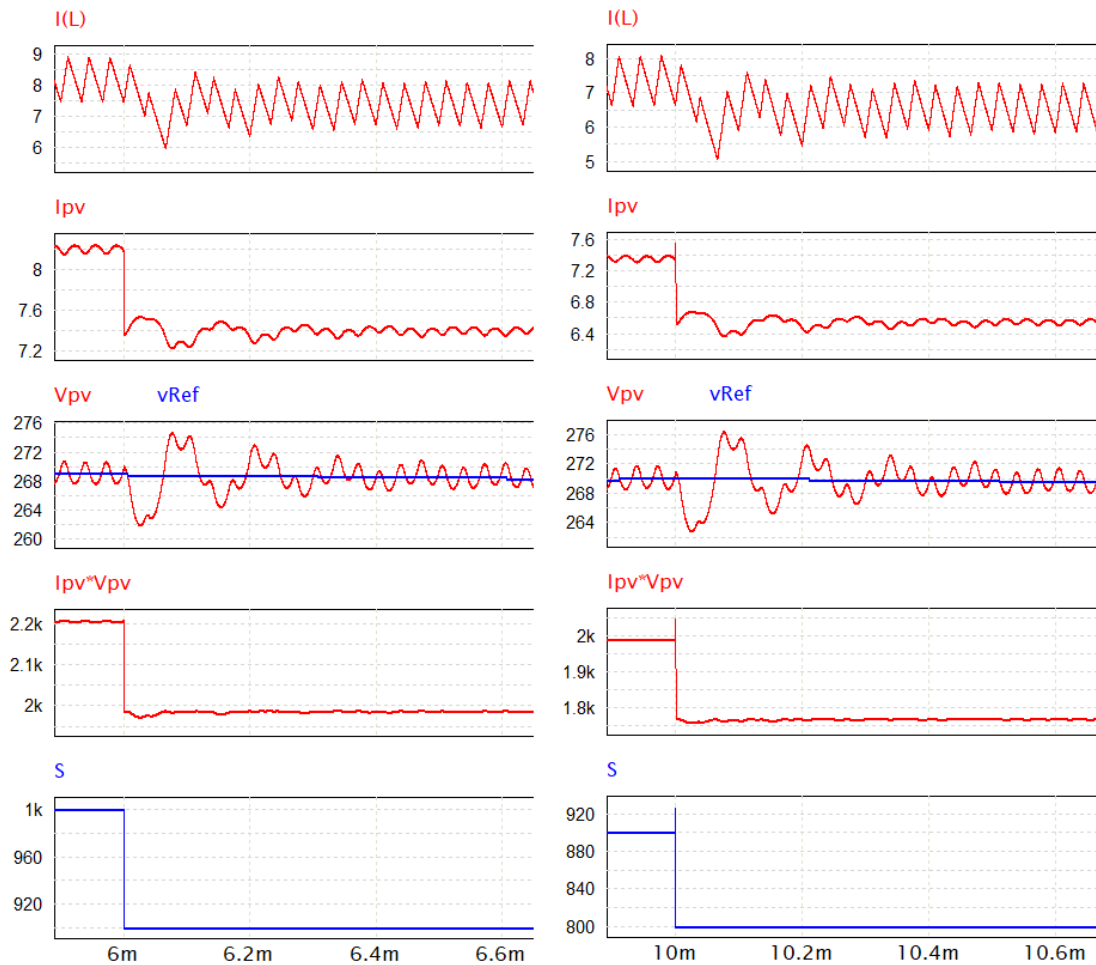
Figure 3.40. Zoom in of the simulated waveforms during validation test of the P&O MPPT with voltage controller for small changes in irradiance for the proposed converter in boost mode.

Figure 3.41 shows a zoom in of the transient response simulation results for sharp changes in irradiance. In the first case, at 14 ms, there was an abrupt decrease of 400 W/m^2 (from 800 to 400 W/m^2) in the irradiance, the proposed control rejected this perturbation producing a voltage deviation below 14.7% (39.55 V) and showed a settling time of about 0.73 ms to recover the steady state. In the second case, at 18 ms, when there was a sharp increase in the irradiance of 600 W/m^2 (from 400 to 1000 W/m^2), the proposed control again rejected the perturbance with voltage deviations below 31.71 V (11.7%) and showed a faster settling time of about 0.26 ms to recover the steady state.
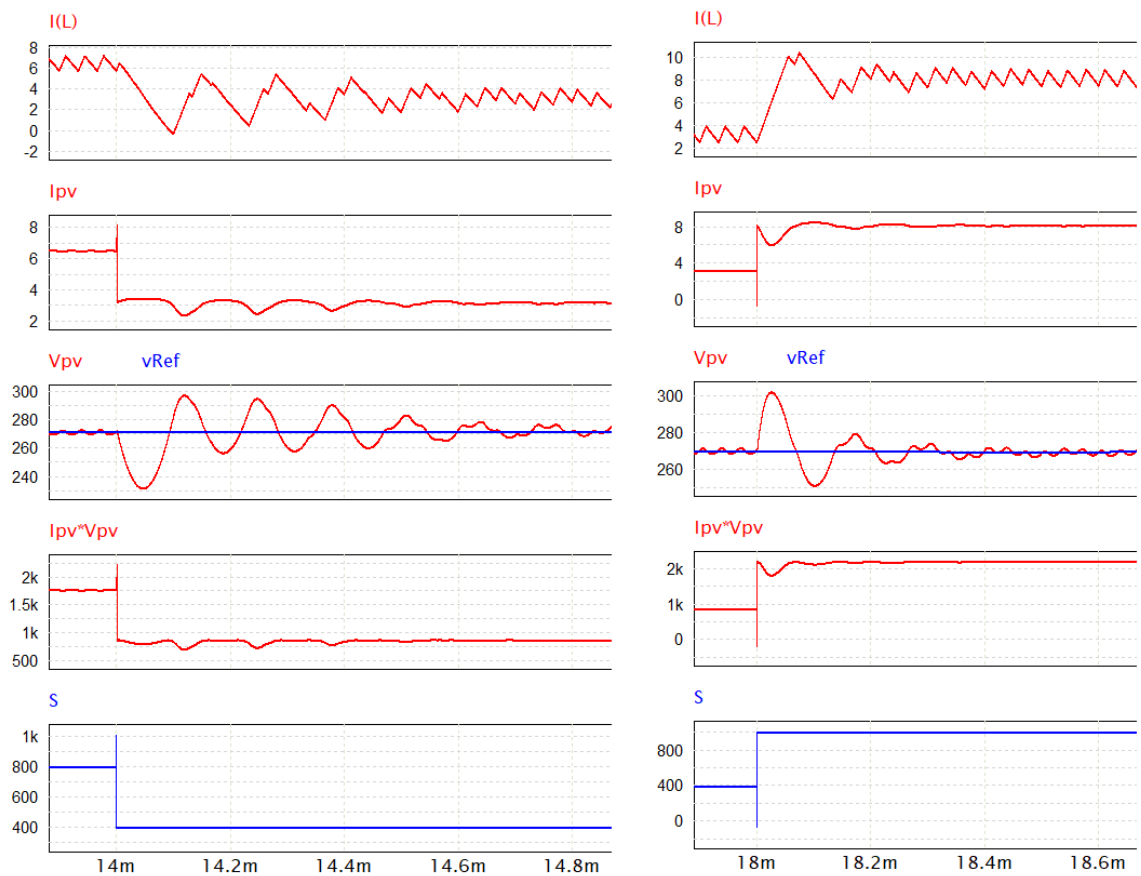
Figure 3.41. Zoom in of the simulated waveforms during validation test of the P&O MPPT with voltage controller for sharp changes in irradiance for the proposed converter in boost mode.

It is worth mentioning that the system transient response for abrupt increase in irradiance disturbances shows faster recovery and lower overshoot peak voltage when it is getting close to the maximum power point of the PV array than when the system is exposed to abrupt decrease in irradiance, moving away from the maximum power point.

3.8 Summary

This chapter presented a detailed description of the design and modelling of a solar PV array and the proposed bidirectional DC-DC buck-boost converter with snow removal functionality to be used in EV charging applications. The design of the controller for the two modes of operation (buck and boost) of the proposed converter was presented, as well as the flowchart of the control algorithm that will be operated by the power management system through a power management command.

The design and simulations satisfactorily evidenced the fulfillment of the functions of the proposed converter: providing a regulated current in direction to the solar PV array that will produce heat in the PV cells to melt the snow cover from the solar panels; and providing maximum power to charge the EV battery pack.

The proposed control provided a robust dynamic response to different disturbances in both modes of operation, as demonstrated by the simulations.

Chapter 4. Experimental Results for Snow Removal Functionality

This chapter describes the implementation of the snow removal functionality in a commercially available power conversion system (PCS). First, the equipment used and the methodology implemented for the test are described. After that, the experimental results are shown followed by discussions. It is worth mentioning that the tests were performed in one of the climatic chambers of the ACE facilities at Ontario Tech University and all the equipment was provided by the company "*Upstartz* Energy Ltd.", who participated as a sponsor in this study.

4.1 Experimental Setup and Equipment

The experimental setup developed for validation of the snow removal functionality was implemented in a commercially available power conversion system that was connected to the solar PV array and was fed by the grid. The block diagram of the experimental setup is shown in Figure 4.1. The system also included an external fused circuit protection on the DC port for safety purposes. The solar PV array consisted of 6 solar PV panels connected in series with different orientations and tilt angles.
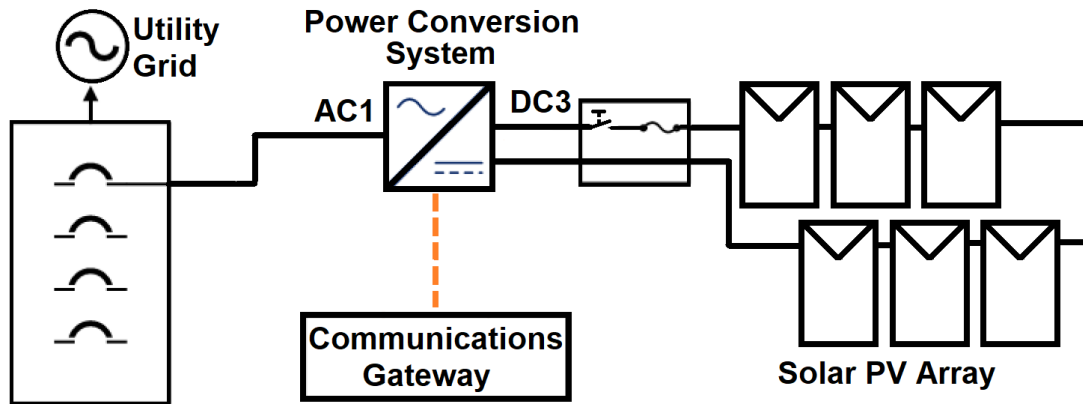
Figure 4.1. Experimental setup block diagram.

The entire installation of the system was developed by personnel from the ACE facilities and by members of the "Upstarz Energy Ltd" company, following the requirements of the manufacturer's guide. In addition, the communication gateway/control management implementation was developed by Sherif Abdelsamad, a member of the "Upstartz Energy Ltd." company. A Raspberry Pi board was used as the system controller

to configure, control and monitor the PCS in real time connected via ethernet through the Modbus TCP interface of the PCS.

4.1.1 *Solar PV Panels*

As it was mentioned before in Chapter 3, there were used Trina Solar PV panels, model TSM-245-PA05 (245 W) for the experimental tests. The characteristics of the solar PV panel were shown in Table 3.1. The voltage and current at MPP of the panel are 30.2 V and 8.13 A, respectively, and the open circuit voltage and short circuit current were 37.5 V and 8.68 A, respectively.

The structure to support each solar PV panel was designed for different inclinations and orientations. The panels were positioned in a horizontal and vertical orientation as shown in Figure 4.2, to identify if there were any difference when producing heat on the solar PV cells.

| (a) | (b) |
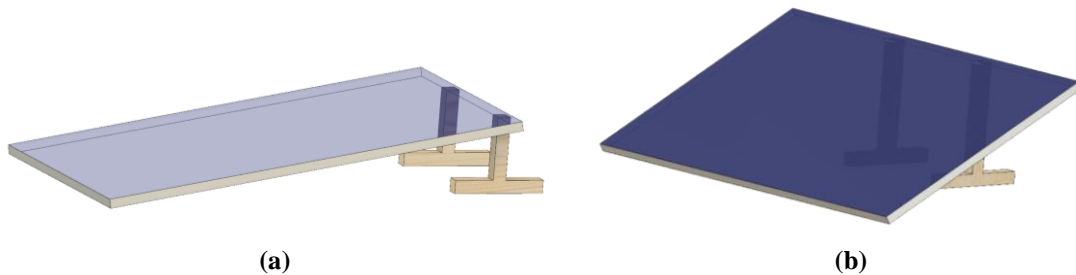
Figure 4.2. Orientation of the solar PV panels for the test validation. (a) Vertical orientation; (b) Horizontal orientation.

The 6 solar PV panels were mounted at tilt angles of 10, 30 and 50 degrees (two panels at each angle); each pair of panels was installed in a horizontal and vertical orientation as mentioned above. All the solar PV panels were connected in series to the PCS to test the snow removal functionality applied to the system. Figure 4.3 shows the setup of the solar PV array for the validation test. At the bottom there can be seem the solar PV panels placed in a horizontal position, while the three solar panels in the back are placed in a vertical position. From left to right they are placed at 50, 30- and 10-degrees tilted angle. The solar PV array had a total voltage and current at MPP of 181.2 V and 8.13 A, respectively as mentioned in Table 3.2.

Figure 4.3. Solar PV array setup for validation test.

4.1.2 *Power Conversion System*

The power conversion system used was the Stabiliti 30 kW Multiport 30C from Ideal Power. This power conversion system has three ports, two of them DC ports to connect a battery and a solar PV array, and one AC port to be connected to the utility grid. It also offers a full galvanic isolation between the AC and DC ports. The specifications of the power conversion system are shown in Table 4.1 and the equipment is shown in Figure 4.4.

Table 4.1. Technical specifications of the Stabiliti 30kW Multiport 30C PCS [154].

AC PORT:	Utility grid
Wiring Configuration	3 wire delta
Maximum AC Power	29.99 kW
Nominal AC Current	37 A
Maximum AC Current	44 A
Nominal Output Voltage	480 Vac
Output Voltage Range	422 Vac to 528 Vac
Nominal Output Frequency	60 Hz
Nominal Power Factor	> 0.99 at rated output power
Peak Efficiency	95.5%
Current Harmonics	< 5% THD
DC PORTS:	**Battery or PV**
Maximum DC Power	30 kW
Maximum DC Current	60 A
Absolute Max Voltage (Voc)	1000 Vdc
Operating Voltage Range	100 Vdc to 1000 Vdc
Full Power Voltage Range	500 Vdc to 1000 Vdc
Integrated DC Filter Yes:	Differential Choke
Wiring Configurations	Grounded Monopolar / Grounded Bipolar / Floating
Ground-Fault Detector Interrupter protection	1 A: fused
Available Control Methods	IDLE, NET, POWER, CURRENT, MPPT

Figure 4.4. Stabiliti 30kW Multiport 30C Power Conversion System.

4.2 Experimental Test Results and Discussion

4.2.1   Test Description and Methodology

The test was performed in one of the climatic chambers of the ACE facility at Ontario Tech University. The test was set for an ambient temperature of -20 C with a 1 cm snow depth over 6 solar panels. The test consisted of 3 pairs of horizontally and vertically oriented solar PV panels with tilt angles of 10°, 30° and 50°, respectively. The test was run for 4 hours (240 min) to identify the performance of the snow removal functionality applied to a commercially available power conversion system.

The test was conducted in one of the climatic chambers at the ACE facility at Ontario Tech University. This chamber is completely insulated from the exterior. The climatic conditions of the chamber were set as follows: at an ambient temperature of -20 C, with 100% humidity, without irradiance, or wind. In the chamber, snow was produced until the 6 solar panels were covered with a snow depth of 1 cm. The solar array configuration consisted of 3 pairs of solar PV panels oriented horizontally and vertically with tilt angles of 10°, 30° and 50°, respectively.

The test was conducted for 4 hours (240 min) to identify the performance of snow removal functionality applied to a commercially available power conversion system.

During the entire test, the temperature, voltage and current of the solar panels were measured approximately every 6 minutes.

The PCS was configured in such a way that it supplied a current of 8 A to the array of solar panels for the first 2 hours of the validation test. Selecting a higher current may produce a faster melting process, however there may be a risk of damaging the solar panels. To avoid damage to the solar panels, it was decided to use the value of current at MPP under standard test conditions provided by the manufacturer. After the first 2 hours of the test, the current was increased to 10 A (25% above the rated current at MPP) to see what the effect was in terms of temperature with respect to time.

4.2.2 Experimental Results

Figure 4.5 shows the initial conditions of the solar PV array. As it was mentioned before, each solar panel had a snow cover of 1cm. The voltage measured in the solar PV array was constant throughout the test. The measured value was 259 V and the measured voltage on each solar panel was approximately 43 V.

Figure 4.5. Initial condition of the solar panels.

The initial current supplied to the solar PV array was equal to the rated current of the solar panels (8 A), however the current measured was 7.5 A during the first two hours of the test. This current caused the photodiodes in the solar panels to dissipate heat, increasing the temperature in the solar panels. In Figure 4.6, it can be seen the first test results after 30 minutes, showing that the solar panels are melting the snow at different rates. For

example, you can see that the two solar panels with a 10° tilt angle are heating up faster than the others, however, the one that is oriented horizontally is the one that has been faster than all of them.
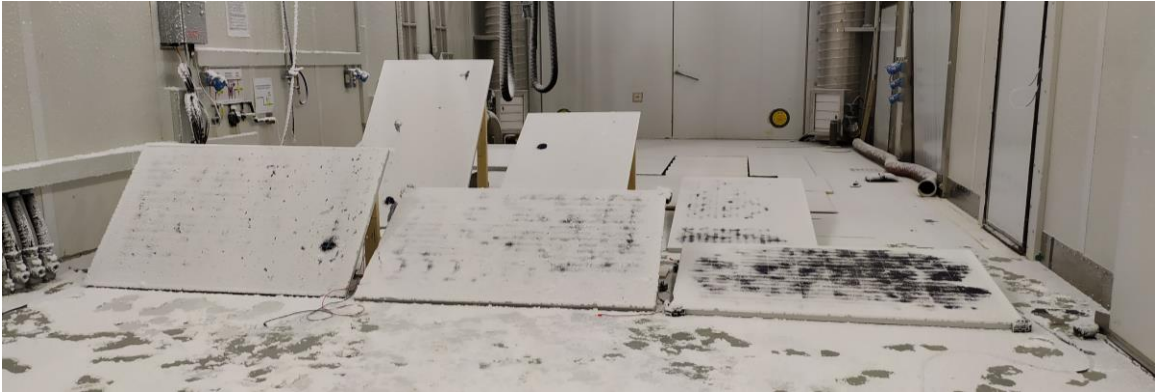
Figure 4.6. Experimental results after 30 minutes of running the test.

After 2 hours of running the tests, it was identified that none of the solar panels completely melted the snow on its surface, so the current was increased to 10 A to increase the speed of the snow melting process. The results after 2 hours of running the tests can be seen on Figure 4.7. In the figure it can be seen that the solar panels placed in a horizontal position had better results than their pairs in a vertical position. They have less snow on their surfaces. Another observation is that at a lower angle of inclination, better results are also obtained for removing snow.
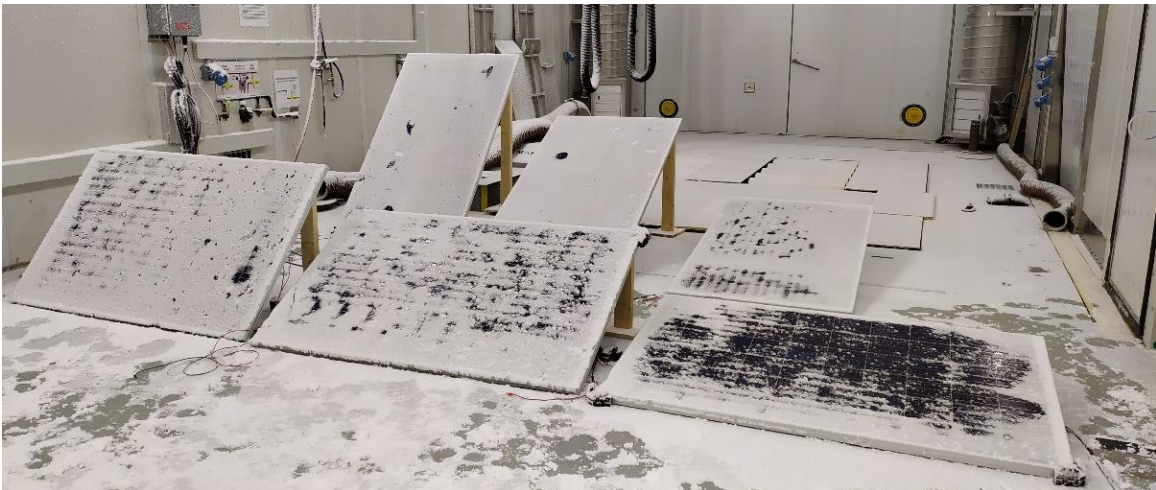
Figure 4.7. Experimental results after 2 hours of running the test.

Based on the results, it is necessary to identify the current required to heat the solar panels to a temperature above 0°C based on the tilt angle of the solar panels and the ambient

temperature, so that it will melt the snow faster and prevent that snow converts into ice as seen on some of the solar panels. This effect can be observed in Figure 4.8.

Figure 4.8. Ice effect over the solar panels.

Figure 4.9. depicts the experimental results obtained from the snow removal test during the first 2 hours. In Figure 4.9 (a) it can be observed the results of all the solar panels combined. As noted in the photo of the solar panels shown in Figure 4.7, the solar panel that heated up the most was the horizontally oriented 10° tilt panel, achieving temperatures close to 0 °C. Worst case scenarios evidenced were from the vertical solar panels of 30° and 50° tilt angle, which increased its temperature to approximately -10 °C only.
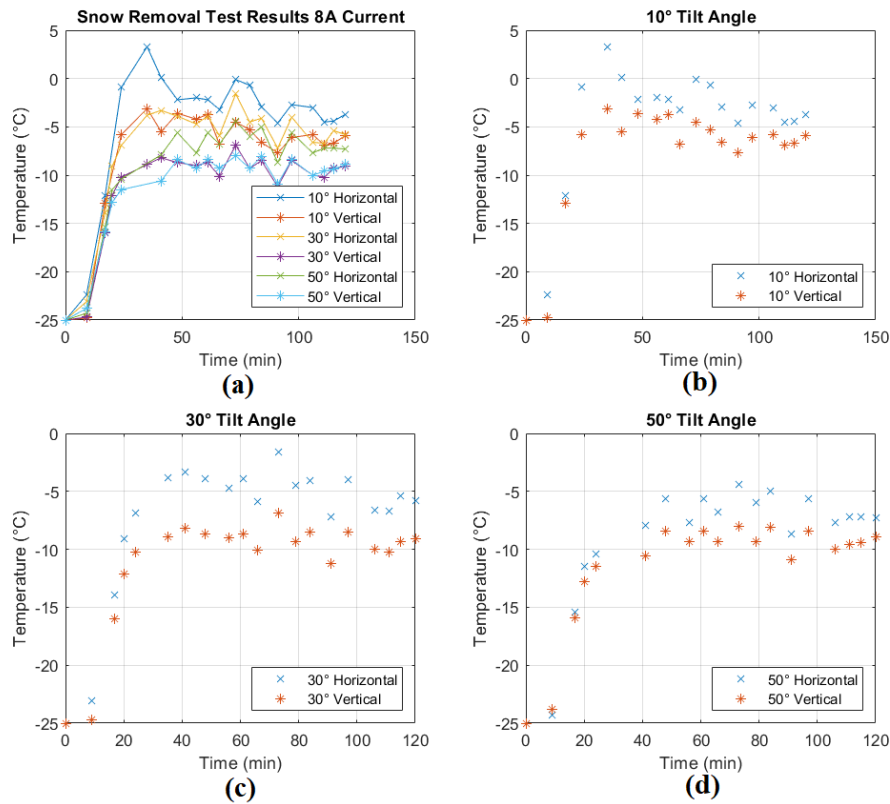
Figure 4.9. Experimental results of the test during the first 2 hours. (a) all the cases; (b) 10° tilt angle solar panels; (c) 30° tilt angle solar panels; (d) 50° tilt angle solar panels (all the measures are not continuous on time).

In Figure 4.9 (b), (c) and (d), it can be seen that solar panels that were placed in a horizontal orientation have a higher temperature than their pairs placed in a vertical orientation.

Using the measured data, a first-order heating model was calculated for each of the cases, obtaining the fitted curves shown in Figure 4.10 and the temperature rise for each case shown in Table 4.2, which confirms the conclusions discussed above.
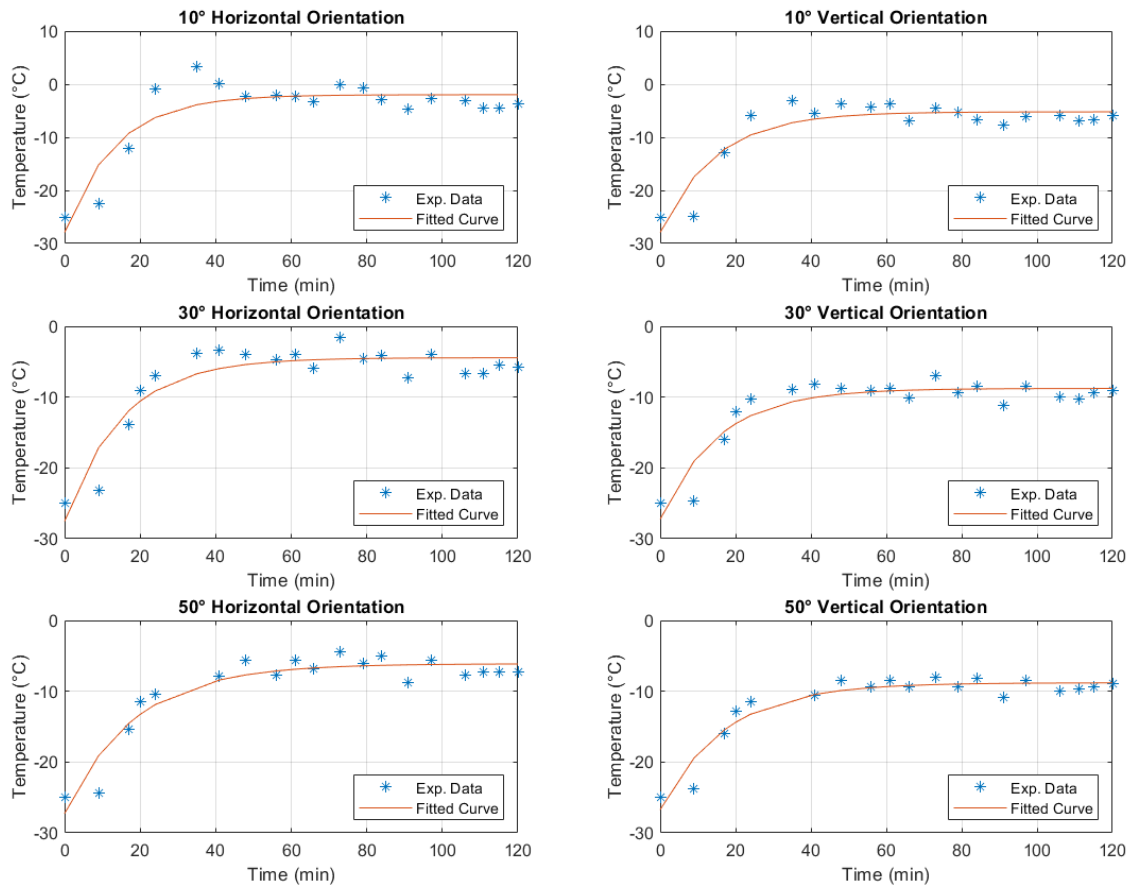
Figure 4.10. Experimental results versus fitted curves for each case during the first 2 hours.

Table 4.2. Temperature rise calculated based on the first-order temperature model obtained from the data.

Case	Initial Temperature	Settling Temperature	Temperature Rise
10° tilt angle – horizontal orientation	-25°C	-1.977°C	23.03°C
10° tilt angle – vertical orientation	-25°C	-5.204°C	19.8°C
30° tilt angle – horizontal orientation	-25°C	-4.435°C	20.55°C
30° tilt angle – vertical orientation	-25°C	-8.774°C	16.23°C
50° tilt angle – horizontal orientation	-25°C	-6.116°C	18.82°C
50° tilt angle – vertical orientation	-25°C	-8.8°C	16.2°C

From the table above, it can be concluded that although the snow removal system can be applied to any solar panel placed in any orientation or angle of inclination, it would be ideal if the solar PV panel was placed in a horizontal orientation so that the snow melts faster, since higher temperatures are reached.

Considering the results obtained from the test and the results of the calculated model shown in Figure 4.10, it can be inferred that at higher ambient temperatures the snow removal system can act faster. If the ambient temperature were -10 °C or higher, the snow melting process would be much more effective and faster, allowing the snow to melt in less than 20 minutes for most of the cases when the surface is cover by 1 cm of snow. Also, for the system to be most efficient, the proper current for a given ambient temperature, depth of snow to melt and different irradiances must be calculated.

After the first 2 hours of the test, the current supplied to the solar PV array was increased to 10 A for a further 2 hours. The current measured was in the range of 9.8 to 10.5 A during the last 2 hours of the test. However, the voltage measured on the solar PV array was a constant 265 V and approximately 44 V on each solar panel.

The final result of the snow removal test performed on the solar PV panels is shown in Figure 4.11. As seem in Figure 4.11, the snow did not completely melt in all cases; this due to the fact that although the surface temperature of the solar panel was higher than the ambient temperature, it did not exceed 0 °C, at which point the solid state of the water changes to a liquid.
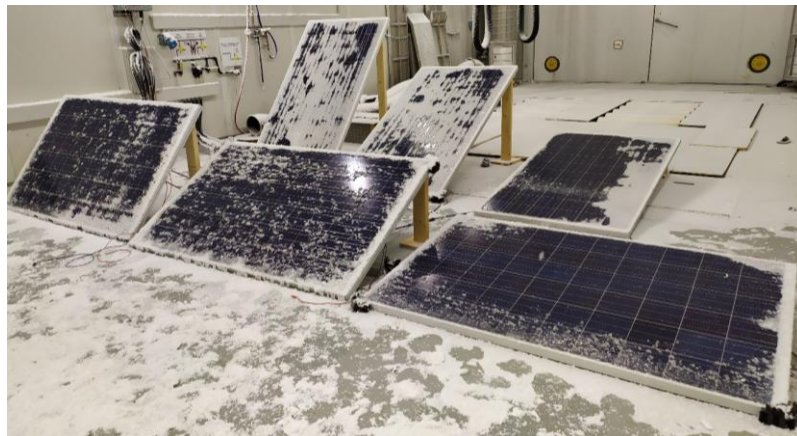
Figure 4.11. Final result of the snow removal test performed for 4 hours on a solar PV array.

In the case of the 10° tilt angle horizontal oriented solar panel, the snow melted almost completely, however, a layer of ice was created at the bottom of the panel surface. The same effect occurred in the other two horizontally oriented modules but over the entire surface of the panel.

The data measured when increased the current to 10 A is depicted in Figure 4.12. There it can be noticed the same behaviour as it was discussed before in Figure 4.9. The horizontal oriented solar panels have a higher temperature rise than their vertical oriented pairs.
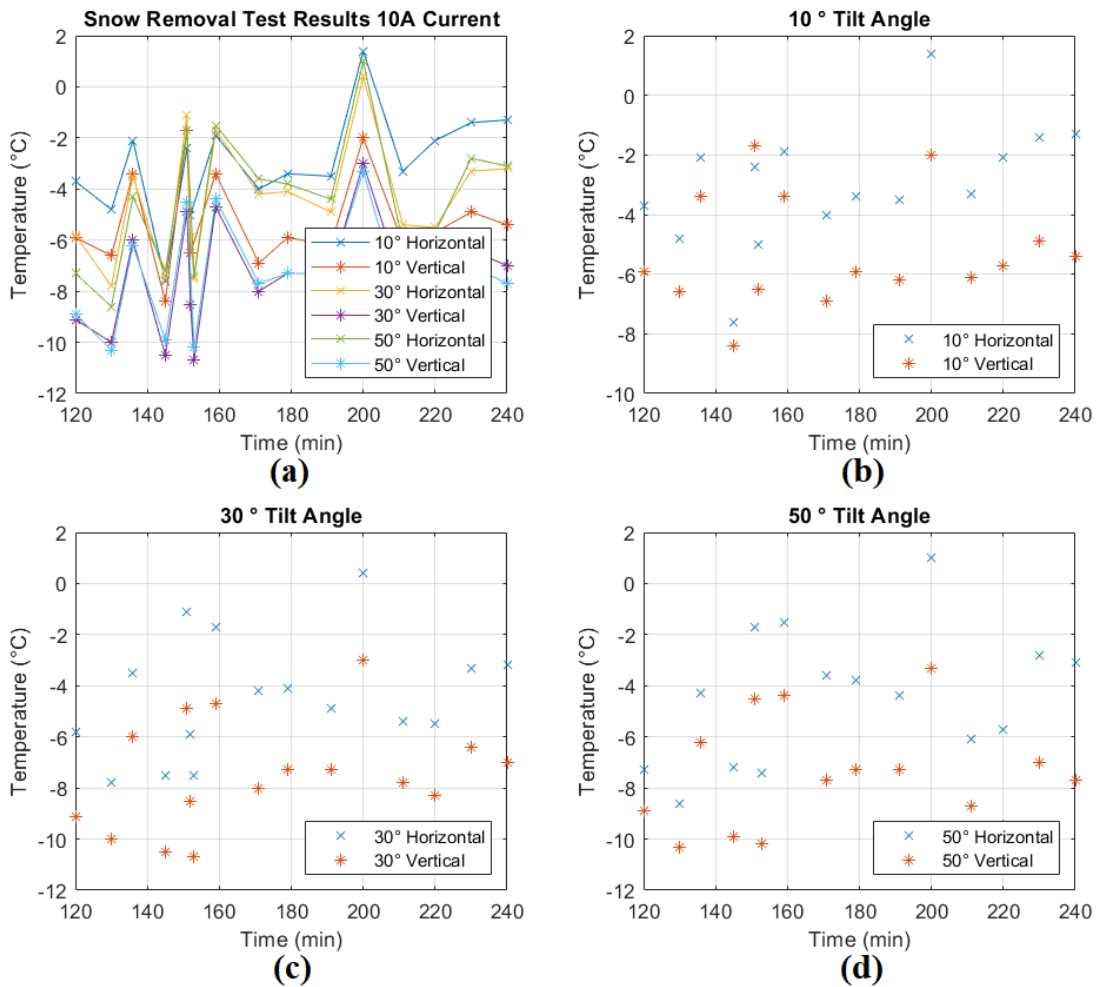
Figure 4.12. Experimental results for each case when current set to 10 A after 2 hours running the test. (a) all the cases; (b) 10° tilt angle solar panels; (c) 30° tilt angle solar panels; (d) 50° tilt angle solar panels (all the measures are not continuous on time).

All the experimental results of the test carried out for 4 hours are shown in Figure 4.13. It is worth mentioning that the results shown in Figure 4.13 from 0 to 120 minutes represent

the temperature data obtained on the surface of the solar panels when the reverse current flow was set to 8 A. After 120 minutes, the data depicted corresponds to the temperature obtained when the current was increased to 10 A.

When the current was increased, the temperature in the solar panels surface increased by a couple of degrees in all cases; however, the maximum temperature reached did not exceed 0 °C, which caused ice to form on the surface of the solar panels as it was discussed before. The temperature difference between the results obtained when the current was set to 8 A and 10 A was calculated using the average temperature after the first 60 minutes of the test, when the temperature settled. The results are shown in Table 4.3.
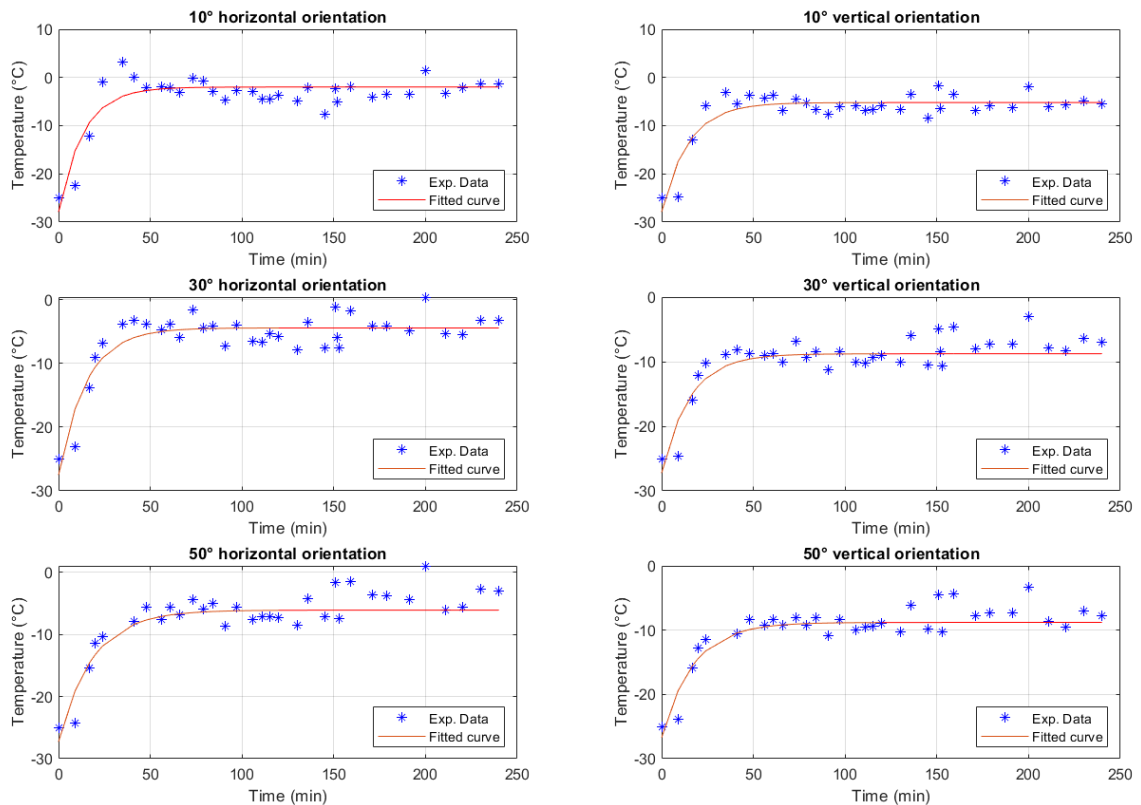
Figure 4.13. Experimental results of the complete test versus fitted curves for each case scenario.

From Table 4.3, it can be identified that the temperature increased for all the cases when increasing the current supplied to the solar PV panels. In this case, there was no clear trend in the results depending on the tilt angle of the vertically oriented solar panels. However, for horizontally oriented solar panels, it was clear that the greater the tilt angle, the greater the temperature rise.

92

Table 4.3. Temperature difference when increasing the current supplied to the PV panels from 8 A to 10 A.

	10° HORIZ ORIEN	10° VERT ORIEN	30° HORIZ ORIEN	30° VERT ORIEN	50° HORIZ ORIEN	50° VERT ORIEN
Last 2 hrs of test (10 A)	-2.78°C	-4.97°C	-4.15°C	-7.18°C	-4.09°C	-7.23°C
First 2 hrs of test (8 A)	-2.91°C	-6.00°C	-5.06°C	-9.25°C	-6.50°C	-9.12°C
Temperature Difference	0.13°C	1.03°C	0.91°C	2.07°C	2.41°C	1.89°C

Finally, it was not clear why the solar panels that had a horizontal orientation had a faster snow melting process than those that had a vertical orientation. However, one hypothesis could be that since a greater surface area of the solar PV panels was closer to the ground, this could have caused the temperature dissipated by the solar cells to remain in this area, decreasing heat losses. It should be noted that the chamber is completely insulated, so there was no other source of heat in the room other than the solar PV panels.

4.3 Summary

In this chapter it was discussed the hardware implementation of the snow removal functionality in a commercially available power conversion system. All the equipment used for the test was described, as well as the methodology and description of the experimental test performed. Afterwards, experimental data was presented and analyzed which indicated that for better results in terms of the speed of the snow melting process, it was better to install the solar PV panels in a horizontal orientation and with low tilt angles. From the results, it was also concluded that solar PV panels with a horizontal orientation placed at the same tilt angle had a higher surface temperature than their pairs in a vertical orientation.

Additionally, the data results in terms of temperature rise on the surface of the solar PV panels suggested that if the ambient temperature is 15 °C higher than the initial temperature of the solar panels (-25 °C), the time required to melt the snow could decrease from 2 hours to less than one hour, since the settling temperature would reach values above 0 °C.

Finally, an effect of ice formation was noted on the surfaces of the solar PV panels because, although the temperature on the surface of the solar panels was higher than ambient temperature, it did not reach values above 0 °C.

Chapter 5. Conclusions and Future Work

5.1 Conclusions

In this thesis, the design, modeling and simulation of a bidirectional DC-DC power converter with snow removal functionality in winter climates to be used in electric vehicle charging applications connected to solar PV systems is presented. In addition, the experimental results obtained using the control algorithm applied to a commercially available energy conversion system for snow removal in a solar PV array are described.

Initially, Chapter 1 presented a general introduction on the importance of solar energy in reducing global CO_2 emissions as well as its available global capacity over the last years. The role played by the rise of electric vehicles and the rapid growth of their demand in the world was also discussed. The effects of snow cover on solar PV systems and a summary of active and passive solutions that have been researched and developed were also presented.

Chapter 2 presented a detailed description of the classification of electric vehicle chargers and the most widely used standards worldwide for power levels, interface, communication, infrastructure and safety in electric vehicle charging applications. The terminology used to describe EV battery packs was discussed and the characteristics for various EV models was presented, suggesting that a range between 320 V to 400 V represented a reasonable assumption for the voltage of the battery to be used for the design of the proposed converter. A complete analysis of the characteristics and modeling of solar PV panels using the single diode model and the Norton equivalent model was also presented. Several MPPT algorithms were discussed and it was suggested to use the perturb and observe algorithm due to its simplicity in its implementation and cost-effectiveness.

Later, a comprehensive study on power electronic topologies used in grid-connected and off-grid solar photovoltaic systems for electric vehicle charger applications was provided. The different circuit topologies for DC-DC and AC-DC converters used in each stage were described including its advantages and disadvantages. Then, a detailed review of the effects of snow on solar PV systems was presented, as well as different active and

passive solutions found in the academic literature to remove snow cover on solar PV systems located in places with extreme winter conditions. However, it was evidenced that there are no electrical solutions analyzed in detail and in depth in the academic literature. Therefore, a bidirectional DC-DC buck-boost converter or also called synchronous buck converter was proposed to meet these needs in electric vehicle charging applications.

Chapter 3 described in detail the design, modelling and control of the proposed bidirectional DC-DC buck-boost converter. A linearized and non-linearized electrical model of the solar PV array was calculated by using the methodology proposed by Dr. Carlos Ramos-Paja in [78]. Then, the different components of the proposed converter were calculated and analyzed for control purposes. A PI current controller (buck operation mode) was designed in order to control the current to be provided to the solar PV array when the heating system is required. Additionally, a PI voltage controller and an perturb and observe MPPT (boost operation mode) were designed to extract the maximum power from the solar PV array to be supplied to the EV battery pack for charging.

The design and simulations evidenced satisfactorily the fulfillment of the two modes of operation of the proposed converter: providing a regulated current in direction to the solar PV array that will produce heat in the PV cells to melt the snow cover from the solar panels; and providing maximum power to charge the EV battery pack. It was identified that the proposed control provides a robust dynamic response to different disturbances in both modes of operation, as demonstrated by the simulations.

Finally, Chapter 4 described the implementation of the snow removal functionality in a commercially available power conversion system (PCS) and the experimental results obtained. The experimental setup developed for validation of the snow removal functionality was implemented in a commercially available power conversion system that was connected to a solar PV array and was fed by the grid. The solar PV array consisted of 3 pairs of solar PV panels connected in series with different orientations (horizontal and vertical) and tilt angles (10°, 30° and 50°). The test was performed in a climatic chamber at an ambient temperature of -20 °C, although the temperature measured by an IR thermal

camera reported -25 °C. In addition, the solar PV panels were covered with 1 cm of snow for validation tests.

The results obtained showed that for better results in terms of the speed of the snow melting process, it was better to install the solar PV panels in a horizontal orientation and with low tilt angles. From the results, it was also concluded that solar PV panels with a horizontal orientation had a higher surface temperature than their pairs placed at the same tilt angle in a vertical orientation for a snow cover of 1 cm.

It was concluded that the current supplied to the solar PV panels throughout the test was not enough to cause the photodiodes to dissipate the heat necessary to completely melt the snow, since in none of the cases, the temperature exceeded 0 °C. An effect of ice formation was noted on the surfaces of the solar PV panels because, although the temperature on the surface of the solar panels was higher than ambient temperature, it did not reach values above 0 °C. This suggested the need to perform a study on what would be the necessary current to increase the temperature on the surface of solar PV panels above 0 °C for different ambient temperatures and amounts of snow, and even for different irradiances.

Additionally, the data results in terms of temperature rise on the surface of the solar PV panels suggested that if the ambient temperature is 15 °C higher than the initial temperature of the solar panels (-25 °C), the time required to melt the snow could decrease from 2 hours to less than one hour, since the settling temperature would reach values above 0 °C, which suggest that possibly all the snow would melt.

The implementation of the current control algorithm in a commercially available PCS suggested that this could be an effective solution for snow removal in existing solar PV systems without requiring the installation of external equipment or expensive components, unlike other solutions found such as mobile robot cleaners, reverse current using external voltage sources, or even resistive layers to be placed on the surface of solar panels.

5.2 Future Work

Suggestions for future work are summarized here:

- **Effects of reverse current on the life cycle of solar PV panels.** Although in this thesis a bidirectional converter was proposed to provide reverse current that would take advantage of the heat dissipation of the PV cells to melt the snow cover on the surface of solar PV panels, and the experimental results showed that it is a feasible solution, the main disadvantage of this proposal is the adverse effects that this may have on the life cycle of solar PV panels. However, there is no study in the academic literature that describes what the short, medium- and long-term effects of solar panels are. For this reason, it is essential that this be carried out in the future to identify if this proposal is viable.

- **Series and parallel configuration of the solar PV array.** The test was implemented using series-connected solar panels, however, it would be interesting to see what the result would be when connecting the solar panels in a series-parallel configuration again using different orientations and tilt angles.

- **Current required to melt snow on the surface of solar PV panels for ambient temperatures starting from -20 °C to 0 °C, for different depths of snow and irradiance.** According to the results obtained for the test performed under an ambient temperature of -20 °C, it was suggested that at higher temperatures the snow cover on the surface of the solar PV panels could melt faster, however, to design a more efficient system, it is necessary to know what the specific current is to melt a certain amount of snow on the solar panels at a specific ambient temperature. This will prevent energy loss. In addition, if the analysis includes the irradiance variation, this will guarantee a more accurate result.

- **What is the percentage of efficiency when implementing this system in a solar PV system?** It is essential to identify what the efficiency gain is during the winter months for a solar PV system using the proposed converter for snow removal functionality.

- **Correlations in transport phenomena to evaluate why horizontally oriented solar panels are more efficient at melting snow than their pairs placed at the same tilt angle in a vertically oriented position.** It is important to identify if the same result can be obtained for larger amounts of snow, different solar PV panels or even different climatic conditions (temperature, wind, solar irradiance), since many factors must be taken into consideration.

Bibliography

[1]   A. Zidan and H. A. Gabbar, "Design and control of V2G," in *Smart Energy Grid Engineering*, Elsevier, 2017, pp. 187–205. Accessed: May 04, 2020. [Online]. Available: https://linkinghub.elsevier.com/retrieve/pii/C20150047086

[2]   IEA, "CO2 emissions from fuel combustion 2019 - Highlights," International Energy Agency (IEA), Highlights 2019 edition, 2019.

[3]   K. V. Singh, H. O. Bansal, and D. Singh, "A comprehensive review on hybrid electric vehicles: architectures and components," *J. Mod. Transp.*, vol. 27, no. 2, pp. 77–107, Jun. 2019, doi: 10.1007/s40534-019-0184-3.

[4]   R. Zhang and S. Fujimori, "The role of transport electrification in global climate change mitigation scenarios," *Environ. Res. Lett.*, vol. 15, no. 3, p. 034019, Feb. 2020, doi: 10.1088/1748-9326/ab6658.

[5]   N. Shaukat *et al.*, "A survey on electric vehicle transportation within smart grid system," *Renew. Sustain. Energy Rev.*, vol. 81, pp. 1329–1349, Jan. 2018, doi: 10.1016/j.rser.2017.05.092.

[6]   F. Badin, J. Scordia, R. Trigui, E. Vinot, and B. Jeanneret, "Hybrid electric vehicles energy consumption decrease according to drive train architecture, energy management and vehicle use," in *IET Hybrid Vehicle*, Coventry, UK, Dec. 2006, vol. 11, pp. 213–223. doi: 10.1049/cp:20060610.

[7]   A. Narayan, "The electrification of transport could transform our future – if we are prepared for it," *World Economic Forum*, Aug. 16, 2018. https://www.weforum.org/agenda/2018/08/we-must-get-it-right-with-electric-vehicles-for-the-sake-of-our-planet/ (accessed May 06, 2020).

[8]   H. A. Gabbar, *Smart Energy Grid Engineering*. Elsevier, 2017. doi: 10.1016/C2015-0-04708-6.

[9]   W. Su, H. Eichi, W. Zeng, and M.-Y. Chow, "A Survey on the Electrification of Transportation in a Smart Grid Environment," *IEEE Trans. Ind. Inform.*, vol. 8, no. 1, pp. 1–10, Feb. 2012, doi: 10.1109/TII.2011.2172454.

[10]   X. Cheng *et al.*, "Electrified Vehicles and the Smart Grid: The ITS Perspective," *IEEE Trans. Intell. Transp. Syst.*, vol. 15, no. 4, pp. 1388–1404, Aug. 2014, doi: 10.1109/TITS.2014.2332472.

[11]   F. Mwasilu, J. J. Justo, E.-K. Kim, T. D. Do, and J.-W. Jung, "Electric vehicles and smart grid interaction: A review on vehicle to grid and renewable energy sources integration," *Renew. Sustain. Energy Rev.*, vol. 34, pp. 501–516, Jun. 2014, doi: 10.1016/j.rser.2014.03.031.

[12]   IRENA, "Renewable capacity statistics 2020," International Renewable Energy Agency (IRENA), Abu Dhabi, 2020.

[13]   A. R. Bhatti, Z. Salam, M. J. B. A. Aziz, K. P. Yee, and R. H. Ashique, "Electric vehicles charging using photovoltaic: Status and technological review," *Renew. Sustain. Energy Rev.*, vol. 54, pp. 34–47, Feb. 2016, doi: 10.1016/j.rser.2015.09.091.

[14]   Y. Ueda *et al.*, "Performance Ratio and Yield Analysis of Grid Connected Clustered PV Systems in Japan," in *2006 IEEE 4th World Conference on Photovoltaic Energy Conference*, Waikoloa, HI, 2006, pp. 2296–2299. doi: 10.1109/WCPEC.2006.279631.

[15] E. Klugmann-Radziemska, "Shading, Dusting and Incorrect Positioning of Photovoltaic Modules as Important Factors in Performance Reduction," *Energies*, vol. 13, no. 8, p. 1992, Apr. 2020, doi: 10.3390/en13081992.

[16] P. Sathyanarayana, R. Ballal, P. L. Sagar, and G. Kumar, "Effect of shading on the performance of solar PV panel," *Energy Power*, vol. 5, no. 1A, pp. 1–4, 2015.

[17] A. Tabanjat, M. Becherif, and D. Hissel, "Reconfiguration solution for shaded PV panels using switching control," *Renew. Energy*, vol. 82, pp. 4–13, 2015.

[18] S. R. Potnuru, D. Pattabiraman, S. I. Ganesan, and N. Chilakapati, "Positioning of PV panels for reduction in line losses and mismatch losses in PV array," *Renew. Energy*, vol. 78, pp. 264–275, 2015.

[19] H. Patel and V. Agarwal, "MATLAB-based modeling to study the effects of partial shading on PV array characteristics," *IEEE Trans. Energy Convers.*, vol. 23, no. 1, pp. 302–310, 2008.

[20] B. Alsayid, S. Alsadi, J. Jallad, and M. Dreidy, "Partial shading of PV system simulation with experimental results," *Smart Grid Renew. Energy*, vol. 4, pp. 429–435, 2013.

[21] M. Fouad, L. A. Shihata, and E. I. Morgan, "An integrated review of factors influencing the perfomance of photovoltaic panels," *Renew. Sustain. Energy Rev.*, vol. 80, pp. 1499–1511, 2017.

[22] M. H. Taghvaee, M. A. M. Radzi, S. M. Moosavain, H. Hizam, and M. Hamiruce Marhaban, "A current and future study on non-isolated DC–DC converters for photovoltaic applications," *Renew. Sustain. Energy Rev.*, vol. 17, pp. 216–227, Jan. 2013, doi: 10.1016/j.rser.2012.09.023.

[23] S. B. Kjaer, J. K. Pedersen, and F. Blaabjerg, "A review of single-phase grid-connected inverters for photovoltaic modules," *IEEE Trans. Ind. Appl.*, vol. 41, no. 5, pp. 1292–1306, 2005.

[24] A. Lohner, T. Meyer, and A. Nagel, "A new panel-integratable inverter concept for grid-connected photovoltaic systems," in *Proceedings of IEEE International Symposium on Industrial Electronics*, 1996, vol. 2, pp. 827–831.

[25] N. P. Papanikolaou, E. C. Tatakis, A. Critsis, and D. Klimis, "Simplified high frequency converter in decentralized grid-connected PV systems: a novel low-cost solution," 2003.

[26] L. Powers, J. Newmiller, and T. Townsend, "Measuring and modeling the effect of snow on photovoltaic system performance," in *2010 35th IEEE Photovoltaic Specialists Conference*, Honolulu, HI, USA, Jun. 2010, pp. 000973–000978. doi: 10.1109/PVSC.2010.5614572.

[27] G. Becker, B. Schiebelsberger, and W. Weber, "An approach to the impact of snow on the yield of grid connected PV systems," *Bavar. Assoc. Promot. Sol. Energy*, p. 4, 2006.

[28] S. Nakagawa, T. Tokoro, T. Nakano, K. Hayama, H. Ohyama, and T. Yamaguchi, "An effect of snow for electric energy generation by 40 kW PV system," p. 4, 2003.

[29] A. Rahmatmand, S. J. Harrison, and P. H. Oosthuizen, "Numerical and experimental study of an improved method for prediction of snow melting and snow sliding from photovoltaic panels," *Appl. Therm. Eng.*, vol. 158, p. 113773, Jul. 2019, doi: 10.1016/j.applthermaleng.2019.113773.

[30] R. W. Andrews, A. Pollard, and J. M. Pearce, "The effects of snowfall on solar photovoltaic performance," *Sol. Energy*, vol. 92, pp. 84–97, Jun. 2013, doi: 10.1016/j.solener.2013.02.014.

[31] R. W. Andrews and J. M. Pearce, "Prediction of energy effects on photovoltaic systems due to snowfall events," in *2012 38th IEEE Photovoltaic Specialists Conference*, Austin, TX, USA, Jun. 2012, pp. 003386–003391. doi: 10.1109/PVSC.2012.6318297.

[32] R. W. Andrews, A. Pollard, and J. M. Pearce, "A new method to determine the effects of hydrodynamic surface coatings on the snow shedding effectiveness of solar photovoltaic modules," *Sol. Energy Mater. Sol. Cells*, vol. 113, pp. 71–78, Jun. 2013, doi: 10.1016/j.solmat.2013.01.032.

[33] H. Awad, M. Gül, K. M. E. Salim, and H. Yu, "Predicting the energy production by solar photovoltaic systems in cold-climate regions," *Int. J. Sustain. Energy*, vol. 37, no. 10, pp. 978–998, Nov. 2018, doi: 10.1080/14786451.2017.1408622.

[34] B. Brench, "Snow-covering effects on the power output of solar photovoltaic arrays," THE U.S. DEPARTMENT OF ENERGY, Lexington, Massachusetts, COO--4094-61, 5232456, Dec. 1979. doi: 10.2172/5232456.

[35] N. Heidari, J. Gwamuri, T. Townsend, and J. M. Pearce, "Impact of Snow and Ground Interference on Photovoltaic Electric System Performance," *IEEE J. Photovolt.*, vol. 5, no. 6, pp. 1680–1685, Nov. 2015, doi: 10.1109/JPHOTOV.2015.2466448.

[36] B. Marion, J. Rodriguez, and J. Pruett, "Instrumentation for Evaluating PV System Performance Losses from Snow: Preprint," Buffalo, New York, May 2009, p. 9.

[37] B. Marion, R. Schaefer, H. Caine, and G. Sanchez, "Measured and modeled photovoltaic system energy losses from snow for Colorado and Wisconsin locations," *Sol. Energy*, vol. 97, pp. 112–121, Nov. 2013, doi: 10.1016/j.solener.2013.07.029.

[38] R. E. Pawluk, "Observations of Snow and Ice Formation on Solar Photovoltaic Panels and an Enhanced Method of Modelling Snow Melting from Solar Photovoltaic Panels," Master dissertation, University of Alberta, Edmonton, Alberta, 2019.

[39] R. E. Pawluk, Y. Chen, and Y. She, "Photovoltaic electricity generation loss due to snow – A literature review on influence factors, estimation, and mitigation," *Renew. Sustain. Energy Rev.*, vol. 107, pp. 171–182, Jun. 2019, doi: 10.1016/j.rser.2018.12.031.

[40] D. Riley, L. Burnham, B. Walker, and J. M. Pearce, "Differences in Snow Shedding in Photovoltaic Systems with Framed and Frameless Modules," in *2019 IEEE 46th Photovoltaic Specialists Conference (PVSC)*, Chicago, IL, USA, Jun. 2019, pp. 0558–0561. doi: 10.1109/PVSC40753.2019.8981389.

[41] G. Becker *et al.*, "Energy Yields of PV Systems - Comparison of Simulation and Reality," *Bavar. Assoc. Promot. Sol. Energy*, p. 3, 2008.

[42] B. P. Jelle, "The challenge of removing snow downfall on photovoltaic solar cell roofs in order to maximize solar energy efficiency—Research opportunities for the future," *Energy Build.*, vol. 67, pp. 334–351, Dec. 2013, doi: 10.1016/j.enbuild.2013.08.010.

[43] D. Brearley, "Designing PV systems for environmental extremes," *SolarPro*, vol. 8, no. 5, pp. 54–70, 2015.

[44] E. Andenæs, B. P. Jelle, K. Ramlo, T. Kolås, J. Selj, and S. E. Foss, "The influence of snow and ice coverage on the energy generation from photovoltaic solar cells," *Sol. Energy*, vol. 159, pp. 318–328, Jan. 2018, doi: 10.1016/j.solener.2017.10.078.

[45] T. Townsend and L. Powers, "Photovoltaics and snow: An update from two winters of measurements in the SIERRA," in *2011 37th IEEE Photovoltaic Specialists Conference*, Seattle, WA, USA, Jun. 2011, pp. 003231–003236. doi: 10.1109/PVSC.2011.6186627.

[46] A. Rahmatmand, S. J. Harrison, and P. H. Oosthuizen, "An improved numerical method for predicting snow melting on photovoltaic panels," in *Conference Proceedings of the eSIM*, 2016, pp. 286–296.

[47] M. Ross and E. Usher, "Photovoltaic Array Icing and Snow Accumulation: A Study of a Passive Melting Technology," *RERinfo.ca*, p. 16, 1995.

[48] M. Ross, "Snow and Ice Accumulation on Photovoltaic Arrays: An Assessment of the TN Conseil Passive Melting Technology," Energy Diversification Research Laboratory, CANMET, Natural Resources Canada, Varennes, EDRL 95-68 (TR), Sep. 1995.

[49] Innos, "Weight Watcher – Innos," *INNOS INNOVATIVE SOLUTIONS*. https://www.innos.no/weight-watcher/ (accessed Jan. 06, 2021).

[50] Laurent Aubert, Martigny, "Les panneaux solaires qui défient la neige," *24 heures*, Dec. 29, 2014. https://www.24heures.ch/suisse/suisse-romande/panneaux-solaires-defient-neige/story/20491743 (accessed Jan. 06, 2021).

[51] A. Weiss and H. Weiss, "Photovoltaic cell electrical heating system for removing snow on panel including verification," in *2016 IEEE International Conference on Renewable Energy Research and Applications (ICRERA)*, Birmingham, United Kingdom, Nov. 2016, pp. 995–1000. doi: 10.1109/ICRERA.2016.7884484.

[52] E. Bellini, "Heating solar panels to clear snow," *pv magazine International*, Mar. 18, 2020. https://www.pv-magazine.com/2020/03/18/heating-solar-panels-to-clear-snow/ (accessed Jan. 06, 2021).

[53] Van Straten, George A., "Heated Solar Panel System and Method," 20150021310, Jan. 22, 2015 [Online]. Available: http://appft.uspto.gov/netacgi/nph-Parser?Sect1=PTO2&Sect2=HITOFF&u=%2Fnetahtml%2FPTO%2Fsearchadv.html&r=5548&p=111&f=G&l=50&d=PG01&S1=20150122.PD.&OS=PD/20150122&RS=PD/20150122

[54] D. Asthana, M. Zinaddinov, M. Ushakov, and S. Mil'shtein, "Cost-Effective Snow Removal from Solar Panels," in *2019 IEEE 46th Photovoltaic Specialists Conference (PVSC)*, Chicago, IL, USA, Jun. 2019, pp. 1312–1315. doi: 10.1109/PVSC40753.2019.8980479.

[55] A. G. Husu, M. F. Stan, C. Cobianu, N. Fidel, and O. Nedelcu, "An inedited solution to increase the energy efficiency of photovoltaic panels for regions with snow," in *2015 13th International Conference on Engineering of Modern Electric Systems (EMES)*, Oradea, Romania, Jun. 2015, pp. 1–4. doi: 10.1109/EMES.2015.7158450.

[56] B. P. Jelle, T. Gao, S. A. Mofid, T. Kolås, P. M. Stenstad, and S. Ng, "Avoiding Snow and Ice Formation on Exterior Solar Cell Surfaces – A Review of Research

Pathways and Opportunities," *Procedia Eng.*, vol. 145, pp. 699–706, 2016, doi: 10.1016/j.proeng.2016.04.084.

[57] A. Rahmatmand, S. J. Harrison, and P. H. Oosthuizen, "An experimental investigation of snow removal from photovoltaic solar panels by electrical heating," *Sol. Energy*, vol. 171, no. July 2018, pp. 811–826, 2018.

[58] A. Weiss and H. Weiss, "Photovoltaic cell electrical heating system for removing snow on panel including verification," *Environ. Sci. Pollut. Res.*, vol. 25, no. 25, pp. 24561–24568, Sep. 2018, doi: 10.1007/s11356-017-0251-4.

[59] J. Popović-Gerber *et al.*, "Power Electronics Enabling Efficient Energy Usage: Energy Savings Potential and Technological Challenges," *IEEE Trans. Power Electron.*, vol. 27, no. 5, pp. 2338–2353, May 2012, doi: 10.1109/TPEL.2011.2171195.

[60] G. Preetham and W. Shireen, "PV Integrated Smart Charging of PHEVs Based on DC Link Voltage Sensing," *IEEE Trans. Smart Grid*, vol. 5, no. 3, pp. 1421–1428, May 2014, doi: 10.1109/TSG.2013.2286745.

[61] S. S. Williamson, A. K. Rathore, and F. Musavi, "Industrial Electronics for Electric Transportation: Current State-of-the-Art and Future Challenges," *IEEE Trans. Ind. Electron.*, vol. 62, no. 5, pp. 3021–3032, May 2015, doi: 10.1109/TIE.2015.2409052.

[62] K. T. Chau, "Pure electric vehicles," in *Alternative Fuels and Advanced Vehicle Technologies for Improved Environmental Performance*, Woodhead, 2014, pp. 655–684. Accessed: May 02, 2020. [Online]. Available: https://www.sciencedirect.com/book/9780857095220/alternative-fuels-and-advanced-vehicle-technologies-for-improved-environmental-performance

[63] A. Sharma and S. Sharma, "Review of power electronics in vehicle-to-grid systems," *J. Energy Storage*, vol. 21, pp. 337–361, Feb. 2019, doi: 10.1016/j.est.2018.11.022.

[64] L. Rubino, C. Capasso, and O. Veneri, "Review on plug-in electric vehicle charging architectures integrated with distributed energy sources for sustainable mobility," *Appl. Energy*, vol. 207, pp. 438–464, Dec. 2017, doi: 10.1016/j.apenergy.2017.06.097.

[65] Q.-S. Jia and T. Long, "A review on charging behavior of electric vehicles: data, model, and control," *Control Theory Technol.*, vol. 18, no. 3, pp. 217–230, Aug. 2020, doi: 10.1007/s11768-020-0048-8.

[66] SAE International, "Surface Vehicle Standard J1772, SAE Electric Vehicle and Plug in Hybrid Electric Vehicle Conductive Charge Coupler." Oct. 2017. [Online]. Available: https://www.sae. org/standards/content/j1772_201710/

[67] National Renewable Energy Laboratory, "Electric Vehicle and Infrastructure Codes and Standards Citations." NREL, Jul. 2010. [Online]. Available: https://afdc.energy.gov/files/pdfs/48605.pdf

[68] B. Lunz and D. U. Sauer, "Electric road vehicle battery charging systems and infrastructure," in *Advances in Battery Technologies for Electric Vehicles*, Elsevier, 2015, pp. 445–467. doi: 10.1016/C2014-0-02665-2.

[69] F. Berthold, "Integration of Plug-In Hybrid Electric Vehicle with the Grid Using Vehicle-to-Home and Home-to-Vehicle Capabilities," Doctor of Philosophy, Concordia University, Montréal, Canada, 2014.

[70] M. A. Delucchi and T. E. Lipman, "Lifetime Cost of Battery, Fuel-Cell, and Plug-in Hybrid Electric Vehicles," in *Electric and hybrid vehicles: power sources, models, sustainability, infrastructure and the market*, Elsevier, 2010, p. 39.

[71] G. Carli, "Photovoltaic based electric and plug-in hybrid electric vehicle battery charging infrastructure using a modified Z-converter topology," Master of Applied Science, Concordia University, Montréal, Canada, 2009.

[72] "EVSpecifications - Electric vehicle specifications, electric car news, EV comparisons," *EVSpecifications*. https://www.evspecifications.com (accessed Nov. 09, 2021).

[73] The Car Guide, "Car manufacturers," *The Car Guide*. https://www.guideautoweb.com/en/makes/ (accessed Nov. 09, 2021).

[74] A. Trejos, D. Gonzalez, and C. A. Ramos-Paja, "Modeling of Step-up Grid-Connected Photovoltaic Systems for Control Purposes," *Energies*, vol. 5, no. 6, pp. 1900–1926, Jun. 2012, doi: 10.3390/en5061900.

[75] M. O. Badawy, "Grid Tied PV/Battery System Architecture and Power Management for Fast Electric Vehicle Charging," Doctor of Philosophy, University of Akron, 2016.

[76] M. A. Hasan and S. K. Parida, "An overview of solar photovoltaic panel modeling based on analytical and experimental viewpoint," *Renew. Sustain. Energy Rev.*, vol. 60, pp. 75–83, Jul. 2016, doi: 10.1016/j.rser.2016.01.087.

[77] G. Petrone, C. A. Ramos-Paja, and G. Spagnuolo, *Photovoltaic Sources Modeling*. John Wiley & Sons Ltd, 2017.

[78] Carlos Andres Ramos Paja, *Modelado de un sistema fotovoltaico*, (Oct. 28, 2020). Accessed: Dec. 22, 2021. [Online]. Available: https://www.youtube.com/watch?v=NlIk3gf36EA

[79] C. A. Ramos-Paja, A. J. Saavedra-Montes, and J. D. Bastidas-Rodríguez, "Cargador de baterías fotovoltaico con control por modos deslizantes y limitación de la derivada de corriente de carga," *TecnoLógicas*, vol. 21, no. 42, pp. 129–145, May 2018, doi: 10.22430/22565337.784.

[80] G. Spagnuolo, E. Franco, J. D. Bastidas-Rodriguez, C. A. Ramos-Paja, and G. Petrone, "Maximum power point tracking architectures for photovoltaic systems in mismatching conditions: a review," *IET Power Electron.*, vol. 7, no. 6, pp. 1396–1413, Jun. 2014, doi: 10.1049/iet-pel.2013.0406.

[81] T. Esram and P. L. Chapman, "Comparison of Photovoltaic Array Maximum Power Point Tracking Techniques," *IEEE Trans. Energy Convers.*, vol. 22, no. 2, pp. 439–449, Jun. 2007, doi: 10.1109/TEC.2006.874230.

[82] F. Schimpf and L. E. Norum, "Grid connected Converters for Photovoltaic, State of the Art, Ideas for Improvement of Transformerless Inverters," p. 6.

[83] V. K. Pathipati, A. Shafiei, G. Carli, and S. S. Williamson, "Integration of Renewable Energy Sources into the Transportation and Electricity Sectors," in *Technologies and Applications for Smart Charging of Electric and Plug-in Hybrid Vehicles*, O. Veneri, Ed. Cham: Springer International Publishing, 2017, pp. 65–110. doi: 10.1007/978-3-319-43651-7_3.

[84] Y. Jiang, "Power Electronics Architectures and Controls for Photovoltaic Solar Energy Systems," Doctor of Philosophy, University of Alabama, Tuscaloosa, Alabama, 2013.

[85] S. Dutta and K. Chatterjee, "A Buck and Boost Based Grid Connected PV Inverter Maximizing Power Yield From Two PV Arrays in Mismatched Environmental Conditions," *IEEE Trans. Ind. Electron.*, vol. 65, no. 7, pp. 5561–5571, Jul. 2018, doi: 10.1109/TIE.2017.2774768.

[86] S. H. Hanzaei, S. A. Gorji, and M. Ektesabi, "A Scheme-Based Review of MPPT Techniques With Respect to Input Variables Including Solar Irradiance and PV Arrays' Temperature," *IEEE Access*, vol. 8, pp. 182229–182239, 2020, doi: 10.1109/ACCESS.2020.3028580.

[87] N. Femia, G. Petrone, G. Spagnuolo, and M. Vitelli, "Optimization of Perturb and Observe Maximum Power Point Tracking Method," *IEEE Trans. Power Electron.*, vol. 20, no. 4, pp. 963–973, Jul. 2005, doi: 10.1109/TPEL.2005.850975.

[88] O. Lopez-Santos *et al.*, "Analysis, Design, and Implementation of a Static Conductance-Based MPPT Method," *IEEE Trans. Power Electron.*, vol. 34, no. 2, pp. 1960–1979, Feb. 2019, doi: 10.1109/TPEL.2018.2835814.

[89] Z. Salam, J. Ahmed, and B. S. Merugu, "The application of soft computing methods for MPPT of PV system: A technological and status review," *Appl. Energy*, vol. 107, pp. 135–148, Jul. 2013, doi: 10.1016/j.apenergy.2013.02.008.

[90] J. Ahmed and Z. Salam, "An improved perturb and observe (P&O) maximum power point tracking (MPPT) algorithm for higher efficiency," *Appl. Energy*, vol. 150, pp. 97–108, Jul. 2015, doi: 10.1016/j.apenergy.2015.04.006.

[91] P. Bharadwaj and V. John, "Direct duty ratio controlled MPPT algorithm for boost converter in continuous and discontinuous modes of operation," in *2014 IEEE 6th India International Conference on Power Electronics (IICPE)*, Kurukshetra, India, Dec. 2014, pp. 1–6. doi: 10.1109/IICPE.2014.7115801.

[92] N. Femia, G. Petrone, G. Spagnuolo, and M. Vitelli, "A Technique for Improving P&O MPPT Performances of Double-Stage Grid-Connected Photovoltaic Systems," *IEEE Trans. Ind. Electron.*, vol. 56, no. 11, pp. 4473–4482, Nov. 2009, doi: 10.1109/TIE.2009.2029589.

[93] S. Khadidja, M. Mountassar, and B. M'hamed, "Comparative study of incremental conductance and perturb & observe MPPT methods for photovoltaic system," in *2017 International Conference on Green Energy Conversion Systems (GECS)*, Hammamet, Tunisia, Mar. 2017, pp. 1–6. doi: 10.1109/GECS.2017.8066230.

[94] S. K. Kollimalla and M. K. Mishra, "A Novel Adaptive P&O MPPT Algorithm Considering Sudden Changes in the Irradiance," *IEEE Trans. Energy Convers.*, vol. 29, no. 3, pp. 602–610, Sep. 2014, doi: 10.1109/TEC.2014.2320930.

[95] P. Mohanty, G. Bhuvaneswari, R. Balasubramanian, and N. K. Dhaliwal, "MATLAB based modeling to study the performance of different MPPT techniques used for solar PV system under various operating conditions," *Renew. Sustain. Energy Rev.*, vol. 38, pp. 581–593, Oct. 2014, doi: 10.1016/j.rser.2014.06.001.

[96] E. Mamarelis, G. Petrone, and G. Spagnuolo, "A two-steps algorithm improving the P&O steady state MPPT efficiency," *Appl. Energy*, vol. 113, pp. 414–421, Jan. 2014, doi: 10.1016/j.apenergy.2013.07.022.

[97] S. Chakraborty, H.-N. Vu, M. M. Hasan, D.-D. Tran, M. E. Baghdadi, and O. Hegazy, "DC-DC Converter Topologies for Electric Vehicles, Plug-in Hybrid Electric Vehicles and Fast Charging Stations: State of the Art and Future Trends," *Energies*, vol. 12, no. 8, p. 1569, Apr. 2019, doi: 10.3390/en12081569.

[98] N. Sujitha and S. Krithiga, "RES based EV battery charging system: A review," *Renew. Sustain. Energy Rev.*, vol. 75, pp. 978–988, Aug. 2017, doi: 10.1016/j.rser.2016.11.078.

[99] S. Dahale, A. Das, Naran. M. Pindoriya, and S. Rajendran, "An overview of DC-DC converter topologies and controls in DC microgrid," in *2017 7th International Conference on Power Systems (ICPS)*, Pune, Dec. 2017, pp. 410–415. doi: 10.1109/ICPES.2017.8387329.

[100] V. T. Tran, D. Sutanto, and K. M. Muttaqi, "The state of the art of battery charging infrastructure for electrical vehicles: Topologies, power control strategies, and future trend," in *2017 Australasian Universities Power Engineering Conference (AUPEC)*, Melbourne, VIC, Nov. 2017, pp. 1–6. doi: 10.1109/AUPEC.2017.8282421.

[101] Jun-Young Lee, Gun-Woo Moon, and Myung-Joong Youn, "Design of high quality AC/DC converter with high efficiency based on half bridge topology," in *PESC 98 Record. 29th Annual IEEE Power Electronics Specialists Conference (Cat. No.98CH36196)*, May 1998, vol. 2, pp. 1054–1060 vol.2. doi: 10.1109/PESC.1998.703135.

[102] N. Wong and M. Kazerani, "A review of bidirectional on-board charger topologies for plugin vehicles," in *2012 25th IEEE Canadian Conference on Electrical and Computer Engineering (CCECE)*, Apr. 2012, pp. 1–6. doi: 10.1109/CCECE.2012.6334957.

[103] D. C. Erb, O. C. Onar, and A. Khaligh, "Bi-directional charging topologies for plug-in hybrid electric vehicles," in *2010 Twenty-Fifth Annual IEEE Applied Power Electronics Conference and Exposition (APEC)*, Feb. 2010, pp. 2066–2072. doi: 10.1109/APEC.2010.5433520.

[104] S. Dusmez, A. Cook, and A. Khaligh, "Comprehensive analysis of high quality power converters for level 3 off-board chargers," in *2011 IEEE Vehicle Power and Propulsion Conference*, Sep. 2011, pp. 1–10. doi: 10.1109/VPPC.2011.6043096.

[105] S. Rivera, B. Wu, S. Kouro, V. Yaramasu, and J. Wang, "Electric Vehicle Charging Station Using a Neutral Point Clamped Converter With Bipolar DC Bus," *IEEE Trans. Ind. Electron.*, vol. 62, no. 4, pp. 1999–2009, Apr. 2015, doi: 10.1109/TIE.2014.2348937.

[106] E. Sanchis *et al.*, "Bidirectional High-Power High-Efficiency non-isolated step-up DC-DC Converter," *PESC Rec. - IEEE Annu. Power Electron. Spec. Conf.*, Jan. 2006, doi: 10.1109/PESC.2006.1711736.

[107] J. Zhang, J.-S. Lai, R.-Y. Kim, and W. Yu, "High-Power Density Design of a Soft-Switching High-Power Bidirectional dc–dc Converter," *IEEE Trans. Power Electron.*, vol. 22, no. 4, pp. 1145–1153, Jul. 2007, doi: 10.1109/TPEL.2007.900462.

[108] G. R. Chandra Mouli, J. Schijffelen, M. van den Heuvel, M. Kardolus, and P. Bauer, "A 10 kW Solar-Powered Bidirectional EV Charger Compatible With Chademo and

COMBO," *IEEE Trans. Power Electron.*, vol. 34, no. 2, pp. 1082–1098, Feb. 2019, doi: 10.1109/TPEL.2018.2829211.

[109] B. Mouawad, J. Espina, J. Li, L. Empringham, and C. M. Johnson, "Novel Silicon Carbide Integrated Power Module for EV application," Xi'an, China, 2018, pp. 176–180. doi: 10.1109/WiPDAAsia.2018.8734672.

[110] S. A. Singh, G. Carli, N. A. Azeez, and S. S. Williamson, "Modeling, Design, Control, and Implementation of a Modified Z-Source Integrated PV/Grid/EV DC Charger/Inverter," *IEEE Trans. Ind. Electron.*, vol. 65, no. 6, pp. 5213–5220, Jun. 2018, doi: 10.1109/TIE.2017.2784396.

[111] A. Bassa de los Mozos, G. R. Chandra Mouli, and P. Bauer, "Evaluation of topologies for a solar powered bidirectional electric vehicle charger," *IET Power Electron.*, vol. 12, no. 14, pp. 3675–3687, 2019, doi: 10.1049/iet-pel.2018.5165.

[112] S. A. Singh, "Design and Implementation of a Single Phase Modified Z-source Inverter Topology for Photovoltaic-Grid Interconnected DC Charging Applications," Doctor of Philosophy, University of Ontario Institute of Technology, Oshawa, Canada, 2018.

[113] B. Singh, B. N. Singh, A. Chandra, K. Al-Haddad, A. Pandey, and D. P. Kothari, "A review of single-phase improved power quality ac~dc converters," *IEEE Trans. Ind. Electron.*, vol. 50, no. 5, pp. 962–981, Oct. 2003, doi: 10.1109/TIE.2003.817609.

[114] B. Singh, B. N. Singh, A. Chandra, K. Al-Haddad, A. Pandey, and D. P. Kothari, "A Review of Three-Phase Improved Power Quality AC–DC Converters," *IEEE Trans. Ind. Electron.*, vol. 51, no. 3, pp. 641–660, Jun. 2004, doi: 10.1109/TIE.2004.825341.

[115] A. Verma and B. Singh, "Control and Implementation of Renewable Energy Based Smart Charging Station Beneficial for EVs, Home and Grid," in *2019 IEEE Energy Conversion Congress and Exposition (ECCE)*, Baltimore, MD, USA, Sep. 2019, pp. 5443–5449. doi: 10.1109/ECCE.2019.8913253.

[116] C.-T. Ma, "System Planning of Grid-Connected Electric Vehicle Charging Stations and Key Technologies: A Review," *Energies*, vol. 12, no. 21, p. 4201, Nov. 2019, doi: 10.3390/en12214201.

[117] A. Meintz, T. Markel, M. Jun, and J. Zhang, "Integrating PEVs with Renewables and the Grid," presented at the 2016 IEEE Transportation Electrification Conference and Expo, Dearborn, Michigan, Jun. 29, 2016.

[118] M. Kisacikoglu, "EV-Grid Integration (EVGI) Control and System Implementation," presented at the APEC 2016, Long Beach, CA, Mar. 23, 2016.

[119] A. Shafiei, "Modeling, Analysis, and Design of a PV-Based Grid-tied Plug-in Hybrid Electric Vehicle Battery Pack Charger," Master of Applied Science, Concordia University, Montréal, Canada, 2013.

[120] T. Kamal, S. Mumtaz, S. Z. Hassan, and L. Khan, "PV based PHEVs smart charging station facility," in *2015 Power Generation System and Renewable Energy Technologies (PGSRET)*, Jun. 2015, pp. 1–6. doi: 10.1109/PGSRET.2015.7312255.

[121] G. Preetham and W. Shireen, "Photovoltaic charging station for Plug-In Hybrid Electric Vehicles in a smart grid environment," in *2012 IEEE PES Innovative Smart Grid Technologies (ISGT)*, Jan. 2012, pp. 1–8. doi: 10.1109/ISGT.2012.6175589.

[122] R. W. Erickson and D. Maksimovic, *Fundamentals of Power Electronics*, Second. Colorado, US: Springer International Publishing, 2004.

[123] P. Rueda, S. Ghani, and P. Perol, "A new energy transfer principle to achieve a minimum phase & continuous current boost converter," in *2004 IEEE 35th Annual Power Electronics Specialists Conference (IEEE Cat. No.04CH37551)*, Aachen, Germany, 2004, pp. 2232–2236. doi: 10.1109/PESC.2004.1355467.

[124] J. Calvente, L. Martinez-Salamero, H. Valderrama, and E. Vidal-Idiarte, "Using Magnetic Coupling to Eliminate Right Half-Plane Zeros in Boost Converters," *IEEE Power Electron. Lett.*, vol. 2, no. 2, pp. 58–62, Jun. 2004, doi: 10.1109/LPEL.2004.834615.

[125] M. Kwon, S. Oh, and S. Choi, "High Gain Soft-Switching Bidirectional DC–DC Converter for Eco-Friendly Vehicles," *IEEE Trans. Power Electron.*, vol. 29, no. 4, pp. 1659–1666, Apr. 2014, doi: 10.1109/TPEL.2013.2271328.

[126] JiTai Han, Chang-Soon Lim, Ja-Hwi Cho, R.-Y. Kim, and D.-S. Hyun, "A high efficiency non-isolated bidirectional DC-DC converter with zero-voltage-transition," in *IECON 2013 - 39th Annual Conference of the IEEE Industrial Electronics Society*, Vienna, Austria, Nov. 2013, pp. 198–203. doi: 10.1109/IECON.2013.6699135.

[127] L. Jiang, C. C. Mi, S. Li, M. Zhang, X. Zhang, and C. Yin, "A Novel Soft-Switching Bidirectional DC–DC Converter With Coupled Inductors," *IEEE Trans. Ind. Appl.*, vol. 49, no. 6, pp. 2730–2740, Nov. 2013, doi: 10.1109/TIA.2013.2265874.

[128] M. Esteki, B. Poorali, E. Adib, and H. Farzanehfard, "Interleaved Buck Converter With Continuous Input Current, Extremely Low Output Current Ripple, Low Switching Losses, and Improved Step-Down Conversion Ratio," *IEEE Trans. Ind. Electron.*, vol. 62, no. 8, pp. 4769–4776, Aug. 2015, doi: 10.1109/TIE.2015.2397881.

[129] I.-O. Lee, S.-Y. Cho, and G.-W. Moon, "Interleaved Buck Converter Having Low Switching Losses and Improved Step-Down Conversion Ratio," *IEEE Trans. Power Electron.*, vol. 27, no. 8, pp. 3664–3675, Aug. 2012, doi: 10.1109/TPEL.2012.2185515.

[130] S. Inoue and H. Akagi, "A Bidirectional DC–DC Converter for an Energy Storage System With Galvanic Isolation," *IEEE Trans. Power Electron.*, vol. 22, no. 6, pp. 2299–2306, Nov. 2007, doi: 10.1109/TPEL.2007.909248.

[131] W. Sun, Y. Xing, H. Wu, and J. Ding, "Modified High-Efficiency LLC Converters With Two Split Resonant Branches for Wide Input-Voltage Range Applications," *IEEE Trans. Power Electron.*, vol. 33, no. 9, pp. 7867–7879, Sep. 2018, doi: 10.1109/TPEL.2017.2773484.

[132] D. Gautam, F. Musavi, M. Edington, W. Eberle, and W. G. Dunford, "A zero voltage switching full-bridge DC-DC converter with capacitive output filter for a plug-in-hybrid electric vehicle battery charger," in *2012 Twenty-Seventh Annual IEEE Applied Power Electronics Conference and Exposition (APEC)*, Orlando, FL, USA, Feb. 2012, pp. 1381–1386. doi: 10.1109/APEC.2012.6166000.

[133] H.-N. Vu, D.-D. Tran, and Woojin Choi, "A novel hybrid soft switching full-bridge PWM and full-bridge LLC converter for on-board battery charger applications," in *2016 IEEE 8th International Power Electronics and Motion Control Conference*

(IPEMC-ECCE Asia), Hefei, China, May 2016, pp. 2470–2473. doi: 10.1109/IPEMC.2016.7512686.

[134] D. Tran, N. Vu, and W. Choi, "A Quasi-Resonant ZVZCS Phase-Shifted Full-Bridge Converter with an Active Clamp in the Secondary Side," *Energies*, vol. 11, no. 2868, p. 21, Oct. 2018.

[135] H.-N. Vu and W. Choi, "A Novel Dual Full-Bridge LLC Resonant Converter for CC and CV Charges of Batteries for Electric Vehicles," *IEEE Trans. Ind. Electron.*, vol. 65, no. 3, pp. 2212–2225, Mar. 2018, doi: 10.1109/TIE.2017.2739705.

[136] F. Musavi, M. Craciun, D. S. Gautam, W. Eberle, and W. G. Dunford, "An LLC Resonant DC–DC Converter for Wide Output Voltage Range Battery Charging Applications," *IEEE Trans. Power Electron.*, vol. 28, no. 12, pp. 5437–5445, Dec. 2013, doi: 10.1109/TPEL.2013.2241792.

[137] J. Zhang, J. Liu, J. Yang, N. Zhao, Y. Wang, and T. Q. Zheng, "A Modified DC Power Electronic Transformer Based on Series Connection of Full-Bridge Converters," *IEEE Trans. Power Electron.*, vol. 34, no. 3, pp. 2119–2133, Mar. 2019, doi: 10.1109/TPEL.2018.2842728.

[138] A. Gheitasi, A. Almaliky, and N. Albaqawi, "Development of an automatic cleaning system for photovoltaic plants," in *2015 IEEE PES Asia-Pacific Power and Energy Engineering Conference (APPEEC)*, Brisbane, Australia, Nov. 2015, pp. 1–4. doi: 10.1109/APPEEC.2015.7380938.

[139] P.-O. A. Borrebæk, B. P. Jelle, and Z. Zhang, "Avoiding snow and ice accretion on building integrated photovoltaics – challenges, strategies, and opportunities," *Sol. Energy Mater. Sol. Cells*, vol. 206, p. 110306, Mar. 2020, doi: 10.1016/j.solmat.2019.110306.

[140] A. Kelkar, "A Bidirectional Battery-to-Battery Energy Cycler for Battery Pack Testing and Validation," Ontario Tech University, Oshawa, Canada, 2020.

[141] City of Toronto, *Zoning By-law 569-2013, as amended (Office Consolidation) - Chapter 200 Parking Space Regulations*. 2021. Accessed: Jun. 01, 2021. [Online]. Available: https://www.toronto.ca/zoning/bylaw_amendments/ZBL_NewProvision_Chapter200.htm

[142] SUNPOWER, "MAXEON 3 400 W." SUNPOWER, 2019. Accessed: Aug. 07, 2021. [Online]. Available: https://sunpower.maxeon.com/au/sites/default/files/2019-07/max3-400-390-370-au_0.pdf

[143] Trina Solar, "Trina Solar TSM-PC05," 2013. https://static.trinasolar.com/sites/default/files/TSM_PC05_datasheet_EN.pdf (accessed Feb. 18, 2022).

[144] O. López-Santos, Y. A. Aldana-Rodríguez, G. Garcia, and L. Martínez-Salamero, "A Unified Multimode Control of a DC–DC Interlinking Converter Integrated into a Hybrid Microgrid," *Electronics*, vol. 8, no. 11, p. 1314, Nov. 2019, doi: 10.3390/electronics8111314.

[145] J. M. Lozano Nieto, "Diseño y Simulación de un Regulador de Histéresis con Frecuencia de Conmutación Fija," Universitat Politecnica de Catalunya, Spain, 2007.

[146] Arnoldo Pacheco Alamos, "Análisis de Pérdidas del Convertidor Buck Síncrono para Aplicaciones Móviles," Centro Nacional de Investigación y Desarrollo Tecnológico, Cuernavaca, Mexico, 2007.

[147] K.-H. Chao, M.-C. Tseng, C.-H. Huang, Y.-G. Liu, and L.-C. Huang, "Design and Implementation of a Bidirectional DC-DC Converter for Stand-Alone Photovoltaic Systems," vol. 2, p. 12, 2013.

[148] Texas Instruments, "Basic Calculation of a Boost Converter's Power Stage," Application Report SLVA372C, Nov. 2009.

[149] Texas Instruments, "Basic Calculation of a Buck Converter's Power Stage," Application Report SLVA477B, Dec. 2011.

[150] D. Gonzalez, C. A. Ramos-Paja, and G. Petrone, "Automated Procedure for Calculating the Controller Parameters in Photovoltaic DC/DC Converters," vol. 6, no. 7, p. 14, 2011.

[151] E. Ugur and B. Vural, "Comparison of different small signal modeling methods for bidirectional DC-DC converter," in *2014 International Conference on Renewable Energy Research and Application (ICRERA)*, Milwaukee, WI, USA, Oct. 2014, pp. 913–915. doi: 10.1109/ICRERA.2014.7016518.

[152] M. C. Merchan Riveros, "Control multimodal para la integración de sistemas fotovoltaicos en microredes híbridas," Master of Science, University of Ibague, Ibague, 2018.

[153] Junhong Zhang, Jih-Sheng Lai, and Wensong Yu, "Bidirectional DC-DC converter modeling and unified controller with digital implementation," in *2008 Twenty-Third Annual IEEE Applied Power Electronics Conference and Exposition*, Austin, TX, USA, Feb. 2008, pp. 1747–1753. doi: 10.1109/APEC.2008.4522963.

[154] Ideal Power, "Stabiliti Product Page," *Ideal Power*. http://dev.idealpower.com/stabiliti-product-page/ (accessed Feb. 18, 2022).

Appendices

Appendix A

A.1 P&O MPPT control code for PSIM

The code was extracted from [78] and the parameters T, dV and V, were modified according to the proposed system.

```
#include <Stdlib.h>
#include <String.h>
#include <math.h>
#include <Psim.h>

// PLACE GLOBAL VARIABLES OR USER FUNCTIONS HERE...
float T;
static float t_mppt;
static float P_old;
float P;
static float V;
static float S;
float dV;


////////////////////////////////////////////////////////////////////
// FUNCTION: SimulationStep
//   This function runs at every time step.
//double t: (read only) time
//double delt: (read only) time step as in Simulation control
//double *in: (read only) zero based array of input values. in[0] is the first node, in[1]
second input...
//double *out: (write only) zero based array of output values. out[0] is the first node,
out[1] second output...
//int *pnError: (write only)  assign  *pnError = 1;  if there is an error and set the error
message in szErrorMsg
//    strcpy(szErrorMsg, "Error message here...");
// DO NOT CHANGE THE NAME OR PARAMETERS OF THIS FUNCTION
void SimulationStep(
                double t, double delt, double *in, double *out,
                 int *pnError, char * szErrorMsg,
```

```
                void ** reserved_UserData, int reserved_ThreadIndex, void *
reserved_AppPtr)
{
// ENTER YOUR CODE HERE...

T=0.35e-3;
dV=250e-3;

P=in[0]*in[1];

if (t<=delt)
{
        t_mppt=0;
        P_old=0;
        S=1;
        V=271.8;
}

t_mppt=t_mppt+delt;

if (t_mppt>=T)
{
        if(P<P_old)
        {
        S = S*(-1);
        }

        V = V+S*dV;
        P_old = P;
        t_mppt=0;
}

out[0]=V;
}
```